Assessment of microstructures and mechanical behaviour of metallic materials through non-destructive characterisation

4 authors, including:

Baldev Raj
Indira Gandhi Centre for Atomic Research
914 PUBLICATIONS   **14,613** CITATIONS

Moorthy Vaidhianathasamy
Newcastle University
66 PUBLICATIONS   **1,182** CITATIONS

Kota bhanu sankara rao
University of Hyderabad
268 PUBLICATIONS   **4,702** CITATIONS

Some of the authors of this publication are also working on these related projects:

Distortion analysis of magnetic excitation voltage - A novel NDT method for ferromagnetic materials evaluation View project

Thermomechanical Fatigue Behavior of a Near Alpha Titanium Alloy: High Pressure Compressor Bling Applications View project

Assessment of microstructures and mechanical behaviour of metallic materials through non-destructive characterisation

Baldev Raj, V. Moorthy, T. Jayakumar and K. Bhanu Sankara Rao

Non-destructive evaluation (NDE) of materials for characterising various key microstructural features, mechanical properties (tension, creep, fatigue crack growth, hardness and fracture toughness), deformation and damage mechanisms has attracted considerable attention in the past 20 years as a primary step towards ensuring structural integrity of components. However, until recently, the correlations between the various NDE parameters and material properties have been only empirical and based on physical principles. The interaction between the NDE probing medium and the mechanical behaviour is not yet fully understood. The purpose of this review is to discuss the progress made in the application of non-destructive testing (NDT) techniques in evaluating various microstructural features and mechanical properties with emphasis on recent studies. Reinterpretation of older data, in the light of present understanding of the interaction of the NDE probing medium with material parameters, is carried out selectively. The NDT techniques evaluated include acoustic emission, ultrasonic attenuation and velocity, magnetic hysteresis parameters, magnetic Barkhausen emission, acoustic Barkhausen emission, laser interferometry, positron annihilation, X-ray diffraction and small angle neutron scattering. Critical assessments of the applicability of the various NDE techniques for the material parameters are provided.   IMR/388

The authors are in the Metallurgy and Materials Group, Department of Atomic Energy, Indira Gandhi Centre for Atomic Research, Kalpakkam 603 102, India (dmg@igcar.ernet.in).

Introduction

The characterisation of microstructures, mechanical properties, deformation, damage initiation and growth by non-destructive evaluation (NDE) techniques is assuming a vital role in various industries because of growing awareness of the benefits that can be derived by using NDE techniques for assessing the performance of various components. Non-destructive evaluation is particularly assuming greater significance in the assessment of material degradation, where investment in new plant is not cost effective and the safe operational life of existing plant needs to be extended. In recent years, various advanced NDE techniques have been successfully employed for characterisation of defects and microstructural features such as grain size, texture, nucleation and growth of second phases, assessment of tensile, creep and fatigue properties, deformation and damage. Non-destructive evaluation techniques are also becoming indispensable in the monitoring and control of fabrication processes for assuring quality of materials and components.

Most components and structures subjected to complex service environments, for example, exposure to elevated temperature and/or loading, undergo degradation of mechanical properties, such as strength, fracture toughness, etc., due to microstructural changes, corrosion, creep and fatigue damage. Microstructural features are decisive, as they determine the physical, mechanical and corrosion performance of materials. Microstructural features and mechanical properties can be assessed using optical and electron-optical and mechanical testing systems, but these are essentially destructive in nature. For characterisation of the microstructures of components, it is essential to develop techniques that give the required information without destroying the material, thus enabling structural integrity assessment, particularly under the severe operating conditions of fatigue, creep, radiation and corrosive environments. With the advent of fracture mechanics concepts, microstructure and defects as well as stresses must be quantitatively characterised to have reliable and fail-safe materials and components. Any alteration in the microstructure which reduces the toughness and, in turn, the life or performance, should be able to be predicted sufficiently in advance to ensure safe, reliable and economic operation of components. This is possible when one realises that the interaction of the non-destructive probing medium with the material depends on the substructural/microstructural features, such as point defects, dislocations, voids, micro- and macrocracks, secondary phases, texture, residual stress, etc. While this is considered advantageous for complete characterisation, often such comprehensive interaction of the probing medium with various microstructural features may lead to extensive modification of signals, thus making interpretations very difficult and necessitating further processing of the signal to obtain feature-specific information. Under such conditions, use of multiple NDE techniques and a multiple NDE parametric approach in a complementary manner helps in isolating the influence of different microstructural features.[1] The benefits of non-destructive characterisation and the challenges in interpretation of results have led to intensive efforts worldwide. Modelling, development of new sensors, advanced signal analysis and materials science based approaches are the new directions.

In the recent past, many NDE techniques have been developed for the characterisation of microstructures, deformation mechanisms, fracture behav-

iour and the assessment of creep and fatigue damage. Ultrasonic parameters, such as attenuation and velocity, and micromagnetic parameters, such as coercive force and magnetic Barkhausen emission, are being used to determine the variation of microstructural features, such as grain size, precipitation, growth of second phases, etc., due to thermal aging. Non-destructive evaluation techniques, such as *in-situ* metallography, acoustic emission (AE), ultrasonic attenuation and velocity measurements, acoustic harmonic measurement, magnetic Barkhausen emission (MBE), acoustic Barkhausen emission (ABE), laser interferometry, positron annihilation (PA), X-ray diffraction (XRD), small angle neutron scattering (SANS), etc., are used for studying creep and fatigue damage. The AE technique has been extensively used to study deformation mechanisms, and to determine the low cycle and high cycle fatigue damage and fatigue crack propagation rate, which in turn estimates the severity of flaws. The different stages of fatigue crack growth can also be identified using this technique. Changes in ultrasonic absorption and velocity have been correlated with changes in dislocation substructure, dislocation density, microcrack formation, etc. Electromagnetic non-destructive testing (NDT) techniques can estimate fatigue crack depth, void density, microstructural variations, creep strain, etc. A recently developed pulsed laser induced ultrasound technique has the potential as a non-contact NDE method to determine creep and fatigue damage. Techniques such as scanning acoustic microscopy, positron annihilation, neutron scattering, etc. are capable of quantifying the damage produced by thermal aging, creep and fatigue processes. In addition, miniature specimens taken from the aged components using scooping devices are also becoming indispensable in assessing the degradation of tensile and fracture properties, and creep and fatigue damage in service exposed components. Very recently, a stress–strain microprobe (SSM) system, based on the automated ball indentation (ABI) technique, has proven to have potential in determining the tensile and fracture properties of materials in a nearly non-destructive manner. However, unlike the use of NDE techniques, which can cover the entire component under inspection, measurements using miniature specimens can be carried out on a limited statistical basis only. In the process, it is possible to miss the region of maximum damage which therefore goes unexamined. Furthermore, these techniques are time consuming and require extensive prior calibration.

In spite of extensive and intensive research conducted using various NDE techniques for different materials and applications, a comprehensive review and critical assessment to compare a wide range of NDE techniques for assessing the microstructure and mechanical behaviour of materials has not been undertaken until now. Since many excellent review articles and books are available on the various NDT techniques for defect detection and sizing,[2–5] in this review attention is focused on the current status and applications of various advanced NDE techniques for assessment of microstructures, creep and fatigue damage in various engineering metallic materials. The applications of the different NDE techniques for damage assessment and life prediction of components are also reviewed. The uncertainties in the use of NDE techniques, and the approach for selection of ideal parameters for effective correlation are discussed. The statistical nature of the results, and the associated scatterband to be taken into account for reliable utilisation of the correlations between materials and NDE parameters for practical utility, are also discussed.

Fundamental aspects of NDE techniques

Understanding the interaction of the NDE probing medium and the material greatly helps in evolving new concepts and specialised approaches in the analysis of the NDE signal towards application in the characterisation of materials. In this section, the fundamental aspects of various advanced NDE methodologies are discussed to provide an overview with the intention that the information will assist in making a choice of technique and approaches to specific issues related to NDE characterisation.

Acoustic emission (AE) technique

Acoustic emission signals are transient elastic stress waves generated by the sudden release of stored elastic strain energy by dynamic processes such as plastic deformation, crack initiation and propagation and martensitic phase transformation, from the material under stress. Detection of an AE signal is usually accomplished with a piezoelectric crystal sensor mounted on the surface of the structure to be monitored. The sensor output is amplified through a high gain low noise preamplifier, filtered in order to remove any extraneous low frequency (LF) hardware noise and high frequency (HF) electromagnetic noise. The AE signals are analysed in a time domain and/or frequency domain depending on the type and characteristics of the AE signals.[6] Brittle crack growth and inclusion/precipitate cracking would normally generate burst type AE signals. The AE signal from plastic deformation and leaks would be of continuous type. In some cases, the time domain parameters would be able to distinguish different AE sources. For example, the AE from plastic deformation would generate signals with low peak amplitude and long duration, whereas the AE signals from brittle crack growth or inclusion/precipitate cracking would have high amplitude and short duration. Frequency domain analysis can be adopted for both burst type and continuous type AE signals. This approach is mainly used for differentiating the different sources of AE, which are inseparable in the time domain, but are generated in different frequency ranges. In this approach, techniques such as autocorrelation and cross-correlation are used to extract the AE signal buried in the noise.

The dynamic nature of AE makes it a useful technique for monitoring the structural integrity of components/structures in various industries with respect to identifying micro- and macroyielding and propagating cracks. A unique advantage of the AE technique is its ability for remote defect location and on-line monitoring of growing defects even in complex geometries. Using this technique, on-line monitoring

of critical components and structures can give advance warning before the occurrence of catastrophic failures. Improved instrumentation and analysis enable the detection and evaluation of the weak signals associated with deformation and propagating fatigue cracks even in high toughness materials such as austenitic stainless steels.

Micromagnetic NDE techniques

Among the various NDE methods, micromagnetic methods are unique and widely used for characterisation of ferromagnetic materials. Ferromagnetic materials consist of magnetic domains, in each of which all the atomic magnetic moment vectors are aligned in parallel. The adjacent magnetic domains are separated by 180 or 90° domain walls.[7,8] When a demagnetised material (where all the domains are oriented randomly) is subjected to an external varying magnetic field, the magnetisation in the material increases in the direction of the applied magnetic field. It is well known that the cyclic magnetisation process consists of domain nucleation, domain wall movement and domain rotation. However, the irreversible movement of magnetic domain walls is the major contribution to the magnetisation process. The magnetisation process is strongly influenced by microstructural features, such as dislocations, grain boundaries, second phase precipitates, and stresses.

The magnetic hysteresis loop (*B–H* loop) is a plot of the magnetic induction *B* as a function of magnetic field *H*.[8] When a ferromagnetic material is subjected to a varying magnetic field, the magnetic flux density during magnetisation varies in discrete steps as the magnetic domain walls have to overcome various types of obstacle during their movement. The discrete changes in magnetisation induce electric voltage pulses in a pick-up coil placed near the surface of a ferromagnetic material.[8–10] These noise-like voltage pulses were first observed by Barkhausen in 1919 and the phenomenon is known as magnetic Barkhausen noise (MBN) or magnetic Barkhausen emission (MBE). This phenomenon is considered to be the first evidence for the existence of magnetic domains in ferromagnetic materials. Plotting the rms (root mean square) voltage of the MBE signal as a function of the magnetic field or the current applied to the electromagnetic yoke would indicate the changes in material parameters. Similarly, during magnetisation, when non-180° domain walls move irreversibly, the magnetostriction causes strain redistribution and in the process generates elastic stress waves known as acoustic Barkhausen emission (ABE). A piezoelectric transducer coupled to the specimen can detect the ABE. Details of the experimental set-up for measurement of all these micromagnetic parameters can be obtained from Refs. 9, 11 and 12.

The magnetic properties can be classified into two categories: (i) structure insensitive properties (saturation magnetisation and Curie temperature) and (ii) structure sensitive properties (maximum magnetic induction for an applied field, permeabilities, hysteresis loss, coercive force H_c, residual induction B_r, MBE and ABE). Any change in the material parameters, even at the microscopic level, would be reflected on these micromagnetic parameters. The changes in the magnetic properties associated with the changes in the material parameters (e.g. alloying elements; grain size and size distribution; density and arrangement of dislocations; size, shape, orientation, distribution and volume fraction of secondary phases; applied and residual stresses; texture; creep damage, fatigue damage; etc.) and, in turn, in the mechanical properties, are measured and the correlations obtained are analysed for evaluation of materials.[13]

Ultrasonic techniques

It is known that an acoustic wave travelling through a material will lose its energy.[14,15] The energy loss is known as attenuation. The total attenuation is caused by basic processes, namely, divergence, absorption and scattering. Beam spreading is primarily a geometric function where the intensity decreases with the square of the distance travelled. Absorption is caused by inelastic interaction as the wave propagates inside the material. The absorption coefficient α_a can be expressed as

$$\alpha_a = a_1 f^{0.5} + a_2 f + a_3 f^2 \qquad . \quad . \quad . \quad . \quad . \quad . \quad (1)$$

where a_1, a_2, and a_3 are constants and f is the frequency. The first, second and third terms in the right-side of equation (1) correspond to the thermoelastic losses, magnetic losses and losses due to dislocation damping respectively.

Ultrasonic scattering is caused by elastic interaction, such as reflection at grain boundaries, small cracks and other regions of impedance mismatch. Scattering is governed by the grain size, frequency of the wave and the anisotropy of the material. Depending on the ratio of the wavelength of the ultrasonic wave λ to the grain size d, the ultrasonic scattering phenomenon can be classified into three regimes, namely

$$\alpha_s \propto d^3 f^4 \quad \text{(Rayleigh scattering, when } \lambda \gg d) \qquad (2)$$

$$\alpha_s \propto d f^2 \quad \text{(stochastic scattering, when } \lambda \approx d) \qquad (3)$$

$$\alpha_s \propto 1/d \quad \text{(diffusion scattering, when } \lambda \ll d) \qquad (4)$$

Measurements from the difference in the amplitudes of the front and back wall echoes give the total attenuation caused by both the absorption and the scattering. Given plane waves of small amplitude, the energy intensity I at a distance x from a source of ultrasound is given by

$$I = I_o \exp(-\alpha x) \qquad . \quad . \quad . \quad . \quad . \quad . \quad . \quad . \quad . \quad (5)$$

where α is the total attenuation coefficient and I_o is the intensity of the incident ultrasonic beam.

It is evident from the above that the ultrasonic attenuation should vary with microstructural changes, such as grain size variation caused by thermal aging and dislocation substructure variation caused by tensile, creep and fatigue deformations, etc.

Ultrasonic velocity is directly connected to the elastic properties and the density of a solid material. Ultrasonic velocity changes have been determined by time-of-flight measurements using a pulse–echo method. An advanced methodology has been developed for precise ultrasonic velocity measurements using a cross-correlation technique. Adaptation of

cubic spline fitting of the cross-correlation function enhances the accuracy in the velocity measurement. The resolution in time delay measurements used for computing the velocity is of the order of 0·5 ns. The relationships between ultrasonic velocity and the elastic properties of materials are as follows. Young's modulus is expressed as

$$E = \rho V_S^2 (3V_L^2 - 4V_S^2)/(V_L^2 - V_S^2) \quad . \quad . \quad . \quad . \quad (6)$$

shear modulus is expressed as

$$G = \rho V_S^2 \quad . \quad . \quad . \quad . \quad . \quad . \quad . \quad . \quad . \quad . \quad (7)$$

and Poisson's ratio is expressed as

$$v = \tfrac{1}{2}(V_L^2 - 2V_S^2)/(V_L^2 - V_S^2) \quad . \quad . \quad . \quad . \quad . \quad (8)$$

where V_L and V_S are the ultrasonic longitudinal and shear wave velocities respectively and ρ is the density of the material.

Based on acousto-elastic theory, it is established that the ultrasonic velocity changes linearly with elastic strain and is expressed as

$$V = V_o + A\sigma \quad . \quad . \quad . \quad . \quad . \quad . \quad . \quad . \quad (9)$$

where V and V_o are the ultrasonic velocities in the stressed and unstressed conditions, σ is the stress and A is the acousto-elastic constant. It has been established that the Young's modulus E and hence the ultrasonic velocity V can be related to the volume fraction of porosity[16] as

$$E = E_o \exp(-bp) \quad . \quad . \quad . \quad . \quad . \quad . \quad . \quad (10)$$

and

$$V = V_o(1 - ap) \quad . \quad . \quad . \quad . \quad . \quad . \quad . \quad (11)$$

where E_o and V_o are the Young's modulus and ultrasonic velocity in material without porosity, p is the volume fraction of porosity, and a and b are constants. This relationship can be employed for the evaluation of creep damage.

It is evident from the above that the ultrasonic velocity measurements are useful for determining several important material parameters, such as moduli, Poisson's ratio, stresses, texture, porosity and characterisation of secondary phases in microstructures which undergo changes due to thermal aging and deformation (e.g. tensile, creep and fatigue) processes.

It has been observed that acoustic waves at harmonic frequencies are generated when fundamental acoustic waves traverse a solid. Apart from lattice anharmonicity, dislocations, microcracks, etc., can also contribute to harmonic generation. The presence of fatigue cracks influences the production of harmonic waves. Harmonicity arises as the crack opens and closes along a portion of the crack front as the acoustic wave passes normal to the fracture plane. An important potential application of this technique is to estimate the remaining fatigue lifetime of a structure by establishing the correlation between the harmonics generated and the progress of fatigue crack growth.[17,18] A substantial amount of harmonic signals must be generated from the numerous small microcracks in the surface that are common precursors to low cycle fatigue (LCF) failure.

X-ray diffraction (XRD) technique

The XRD technique is widely used for measuring changes at the crystal lattice level caused by metallurgical phase transformations and deformation processes. It can be easily understood that tensile stress would increase while compressive stress would decrease the lattice parameter. Any change in the internal stress/strain would result in a shift in the location of the peak in the diffraction profile depending on the nature of the stress; the peak position is proportional to the stress value. The principle stresses of a two-dimensional stress state can be determined by the conventional $\sin^2 \psi$ method.[19,20] In addition, the generation of dislocations in the material would broaden the diffraction profile. The measurement of the full width at half maximum (FWHM) of the diffraction profile would indicate the changes in the dislocation substructure caused by the plastic deformation process, such as cold rolling and fatigue. The detailed analysis of the changes in peak position and the FWHM would greatly help in materials characterisation. The change in the diffraction profile can be used to predict the precipitation kinetics in precipitation hardening alloys, as the transformation of coherent precipitates into incoherent precipitates would be reflected in the diffraction profile. Macroscopic residual stress is generally caused by inhomogeneous plastic strains in a structure due to damage such as fatigue. Most of the engineering applications and fracture mechanics calculations require knowledge of this residual stress. The XRD technique can rapidly measure applied and residual stresses in a small area on the surface of polycrystalline materials. Personal computer based portable automatic systems are now available for reliable and rapid measurement of stresses. The disadvantage of this technique is that it gives information only from shallow depths of the order of 10–30 μm.

Small angle neutron scattering (SANS)

It has been well established that when a beam of neutrons enters a material, it undergoes scattering by microstructural features such as grain boundaries, dislocations, second phase precipitates, voids, and microcracks. The magnitude of the neutron scattering vector is defined as

$$q = 4\pi \sin \theta/\lambda$$

where θ is the Bragg angle and λ is the neutron wavelength. The measurement of scattering intensity over a range of scattering vectors is used for the estimation of the volume fraction and size distribution of a particular type of microstructural feature, such as voids, cavities, and second phase precipitates. Several numerical techniques are used for converting the scattering intensity profile into the size distribution of defects.[21,22] The plot of scattering cross-section $d\Sigma/d\Omega$ versus scattering vector q can be used to obtain information about the type of microstructural feature. For example, the volume fraction of the scattering centres can be calculated from the integration of $d\Sigma/d\Omega$ over the entire reciprocal space and their size distribution can be determined from an inversion of scattering data.[21,22]

Small angle neutron scattering (SANS) provides information on the shape and size distribution of microstructural defects in a variety of materials in a non-destructive manner. It can detect much smaller defects as compared to other NDE techniques owing to:

(i) the longer wavelengths of neutrons (5–10 Å) compared to X-rays (this eliminates multiple Bragg scattering phenomena and consequently simplifies the analysis of the observed spectra)

(ii) increased depth of penetration (several millimetres)

(iii) the widely varying neutron scattering cross-section with atomic number (permitting clear distinction of the scattering contribution from neighbouring elements in the periodic table).

These advantages enable the SANS technique to be used to study voids, precipitates and many other types of defect in solids. The SANS method can be used to examine bulk defects of sizes ranging between 0·01 and 0·1 µm.

Positron annihilation (PA) technique

Positrons are positively charged particles of electronic mass emitted from radioactive sources. For example, β decay of sodium-22 is an efficient source of positron emission. When the positrons enter the solid, they tend to annihilate with negatively charged electrons in the medium. It has been found that the rate of annihilation of the positrons is determined by the density of the electrons at the position of positrons.[23] Since the electron density distribution in the region of crystalline defects is different from that in a defect free lattice, the annihilation characteristics of positrons trapped in vacancies, dislocations and microvoids are significantly different from those of untrapped positrons.

One way of using this technique for materials characterisation is by measuring the lifetime of a positron before its annihilation. The lifetime of the positron is determined by measuring the time difference between the 1·28 MeV γ-ray emitted during the creation of positrons and the 0·511 MeV γ-ray emitted during the annihilation of positrons. The positron annihilation radiation carries information concerning the momentum of the electron–positron pair. A consequence of this momentum is the Doppler broadening of the profile of the positron annihilation radiation. The annihilation profile can be measured using a high energy-resolution germanium detector. The line-shape parameter S is calculated from this annihilation profile, i.e. the counts versus γ-ray energy plot. The S parameter is defined as the ratio of the counts in the central region to the total counts in the annihilation profile.[24] The complementary W parameter, deduced from the normalised counts in the wing region of the spectrum, is also used in applications related to chemical composition changes. While the S parameter signifies the annihilation events with valence electrons, the W parameter signifies the annihilation events with core electrons.
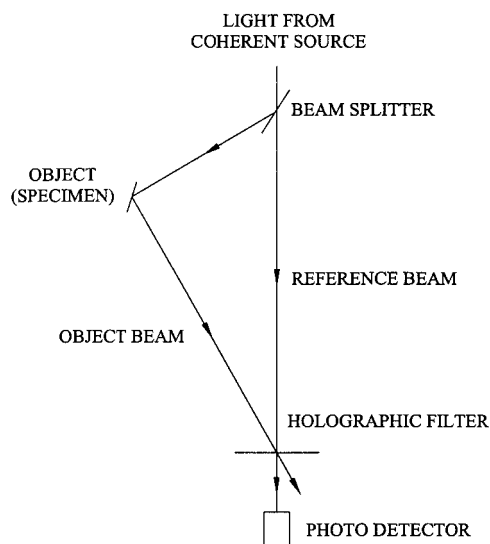
1 Schematic of optical correlation system for non-destructive measurement[25]

Many recent investigations on the annihilation characteristics of positrons show the high sensitivity of positrons to lattice defects, such as vacancies and dislocations, and provide information about the nature and concentration of these defects. By exploiting the annihilation characteristics of positrons, this technique can be used as a NDE tool for evaluating the changes in second phase precipitation and growth during thermal aging, and changes in dislocation density, vacancy concentration, void formation and growth, microcrack formation and growth, etc. caused by fatigue and creep damage. At present, the technique is laboratory based, wherein a specimen or a component is brought to the laboratory for measurements. The typical time scale for each measurement is of the order of a few tens of minutes, thus it is slower than other non-destructive techniques such as ultrasound.

Laser scattering technique

The laser scattering technique is being considered as a viable NDE tool for quantitative surface topography and strain measurements.[25–27] In this optical scattering method, two types of approach are followed, namely, holography and speckle pattern. In the holographic technique, optical correlation measurements are used for surface damage evaluation. In the optical correlation method (*see* Fig. 1 for schematic diagram), first, an optical hologram of the unaffected surface is generated by superimposing the light scattered from the specimen surface (object beam) and a coherent plane wave reference beam on a light sensitive film or some alternative recording device. For observing any change in the surface of the object as a result of service exposure, the reference beam is blocked out. The light beam from the coherent source, which is scattered by the damaged object surface, is allowed to pass through the processed hologram. The scattered light from the damaged object surface modifies the reference beam, which can be viewed from the hologram. The intensity of the central peak of the

modified reference beam is measured by a photodetector, as shown in Fig. 1, and is termed the optical correlation intensity. The optical correlation intensity is reduced with increase in surface roughness. In cases where the surface has undergone severe plastic deformation, the increased surface roughness causes the pattern of the scattered light to become more diffuse. In such cases, the speckle technique is employed, where the speckle pattern on the surface of a material to be evaluated is digitised and the digitised intensity distribution is smoothed using numerical processing and is plotted as average grey level as a function of spatial frequency (line/mm). The width at half the maximum of grey level is defined as spectrum width. Optical correlation measurement is highly sensitive to surface topography, but its practical applications are limited by interference from rigid body movement. The spectrum width technique is advantageous because it is insensitive to rigid body movement, but extremely sensitive to surface changes prior to crack initiation and can detect the progressive damage on the surface. Another technique considered for characterisation of surfaces experiencing deformation is based on the evaluation of fractal dimension by using surface relief images obtained from a scanning electron microscope.[28] A good correlation is obtained between the stepwise increase in fractal dimension with stepwise increase in load in austenitic stainless steel specimens. Thus, stepwise increase in fractal dimension is further correlated with the specific energies dissipated in deformed specimens.

Miniature specimen testing

Assessment of structural integrity and prediction of remaining life in service exposed components/structures, requires evaluation of mechanical properties such as yield strength, ultimate tensile strength and ductility. Fabrication of standard size test specimens from these components is not possible. There exists a need for techniques capable of estimating the mechanical properties of components from small size specimens, which can be made from material scooped out of the service exposed components. There are many types of testing method suitable for mechanical property determination using miniaturised specimens, including: microindentation, shear punch, bulge, miniature disc bend, miniature tensile, and miniature Charpy tests. Small specimen testing methodologies have been developed for evaluation of mechanical properties such as: biaxial stress/strain, yield strength, tensile strength, ductility, Charpy fracture appearance transition temperature (FATT) and fracture toughness of metals and alloys, while using a greatly reduced volume of material. For example, the disc punch tests employ circular disc specimens of ~ 3 mm dia. and 0·3 mm thickness. The testing involves axisymmetric loading of a small disc specimen with different types of punch (hemispherical, cylindrical with flat tip, etc.) and the resultant load–deflection/displacement curve is analysed to obtain mechanical properties. Proper care is taken during the preparation of the specimens right from the stage of scooping out the 'moon' sample and grinding and polishing to avoid deformation/cold work/alteration
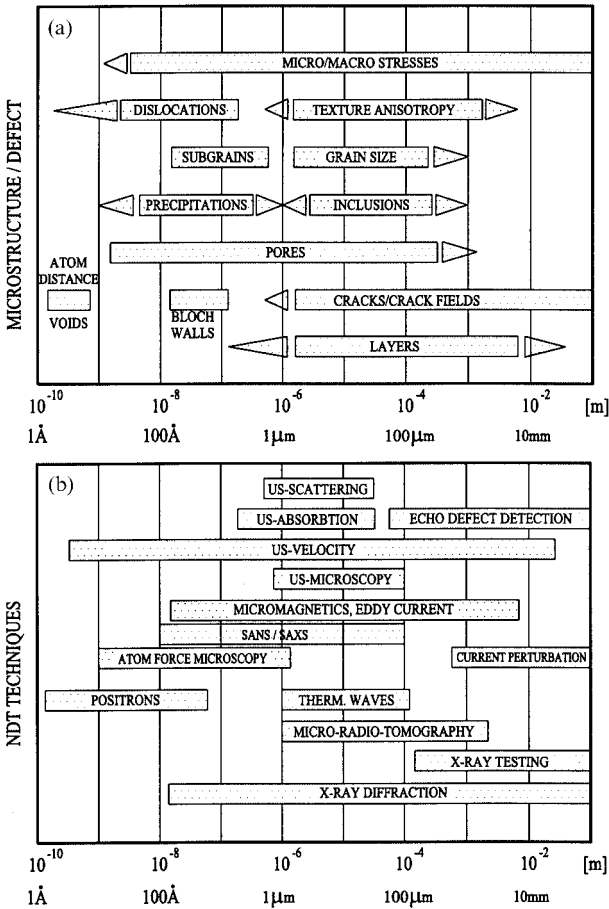
2 *a* Dimensions of various microstructural features required to be characterised as part of NDT evaluation and *b* capabilities of various NDT techniques for characterising microstructural features depicted in *a*[33]

in substructure. There is a good correlation between the properties measured through conventional mechanical testing and miniature specimen testing methodologies. Excellent reviews on the principles, design considerations and procedures for mechanical property evaluation for various miniature specimen testing techniques are presented in Refs. 29–31. The automated ball indentation (ABI) technique has been developed to determine the tensile and fracture properties of materials in a nearly non-destructive manner.[32]

Microscopy techniques

One of the important clues to the damage of a component is obtained from details of microstructure. Microscopy can provide useful information for reliable prediction of the remaining life. This can be achieved non-destructively by using *in situ* metallography or replication techniques. The localised region of interest on a component/structure after on-site metallographic preparation is observed directly using a portable optical microscope if there is accessibility or after taking a replica of the region and then viewing under a microscope. Replicas are especially suitable for those components whose complex load cannot sufficiently be described by stress

analysis, e.g. welds with complex microstructure. *In situ* metallography has found extensive applications in assessing creep damage, precipitation of harmful second phases, etc. in long service exposed components. It is possible to assess the different stages of creep damage, such as microstructural changes, formation of isolated cavities, aligned cavities, microcracks and macrocracks. Currently available small portable microscopes with a CCD camera facility can greatly help in enhancing the resolution in observing the microstructural details by *in situ* metallography.

Micro NDT methods are being increasingly applied, especially for new materials, for characterising the condition of the material by providing local high resolution images. The basic principle for nondestructive characterisation is the interaction of any type of energy with the test material. Based on these, many non-destructive microscopic techniques have been recently developed. Figure 2a presents the dimensions of various microstructural features that need to be characterised as part of NDT evaluation.[33] The capabilities of various NDT techniques for determining the microstructural features depicted in Fig. 2a are indicated in Fig. 2b.[33] A comparative evaluation of various microscopic NDT techniques with respect to the probing medium, its interaction with microstructural features and the possible applications is given in Table 1.

Acoustic microscopy has been widely used for materials characterisation and damage assessment studies. Acoustic microscopy can find small cracks and locate their tips, detect damage ahead of crack tip, distinguish cracks from slip bands and grain boundaries with a reliability and accuracy comparable to optical microscopy. Techniques such as positron microscopy, photothermal microscopy and magnetic Barkhausen microscopy[34] have the potential to assess surface and subsurface defects, local residual stress, etc. A miniaturised MBE probe whose spatial resolution is of the order of 10 µm has been developed for measuring the local residual stress. These microscopic NDT techniques are capable of imaging the surface and subsurface damage, thereby assessing the extent of damage induced by fatigue and creep.

Characterisation of microstructures by NDE techniques

Grain size measurement

Grain size in the case of ferrite/austenite microstructure or lath size in the case of martensite/bainite microstructure is an important engineering parameter which influences mechanical properties such as yield strength, fatigue strength and creep strength. Metallography, *in situ* or using the replica technique, is widely used for grain size measurement on service exposed industrial components. The main limitation of the technique is that it is very time consuming for global assessment of large components. Many studies using other NDT techniques have shown excellent correlation between various NDE parameters and grain size. Micromagnetic parameters such as coercive force and peak height of the MBE have been correlated with grain size in ferromagnetic materials. Ultrasonic attenuation, velocity and spectral parameters have been related to the average grain size in various metallic materials.

Grain size measurement by magnetic Barkhausen emission (MBE) techniques

Coercive force H_c derived from a B–H loop is considered as the structure sensitive parameter when the

Table 1 Microscopic non-destructive testing (NDT) techniques

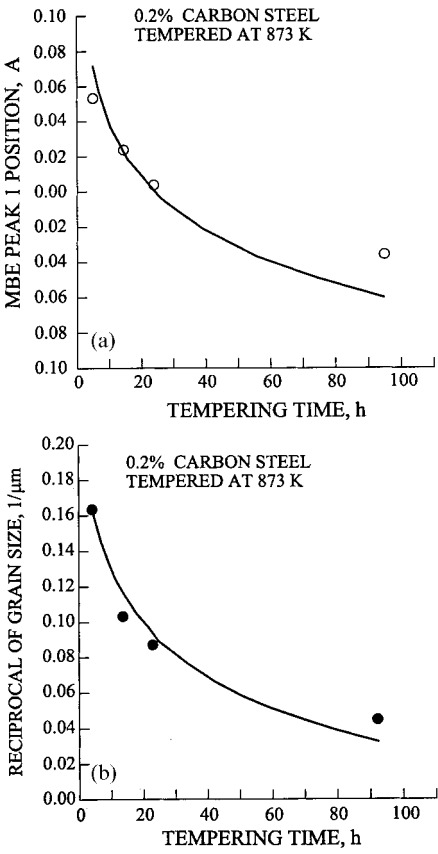| Method	Energy input	Interaction signal	Detected	Applications
Raster electron microscopy	Electron beam	Deceleration of electrons	X-rays	Surface topography
Electron beam microanalysis	Electron beam	Energy loss of electrons	Characteristic X-rays	Microanalysis
Electro-acoustics	Modulated electron beam	Local periodic heating	Elastic waves	Surface structure
Photo-acoustics	Modulated laser beam	Local periodic heating	Elastic waves	Surface layers
Photothermal microscopy	Modulated laser beam	Local periodic heating	Surface temperature	Surface layers, subsurface defects
Photothermally modulated stray fields	Modulated laser beam	Fluctuations in magnetisation	Magnetic fields	Local magnetic properties
Laser scan microscopy	Laser beam	Reflection of laser light	Reflected light	Surface imaging
HF ultrasound acoustic microscopy	Focused ultrasound	Propagation of elastic waves	Elastic waves	Surface layers, subsurface defects
Scanning tunnelling microscopy	Electric field	Exchange of tunnelling electrons	Tunnelling current	Local electron density
Scanning force microscopy	Mechanical force	Tip–sample interaction	Deflection of microcantilever	Surface topography, surface friction
Eddy current microscopy	Modulated magnetic field	Eddy current propagation	Impedance of miniaturised probe	Visualisation of electric and magnetic properties
Barkhausen microscopy	Magnetic field varying with low frequency	Movement of Bloch walls	Barkhausen noise	Local residual stress
Positron microscopy	Slow and focused positrons	Trapping and annihilation	γ radiation 0·511 MeV	Local near lattice defects
Nuclear magnetic resonance imaging	Static magnetic and HF electromagnetic field moments	Excitation of magnetic states	Decay of magnetic excitation of protons	Distribution and mobility
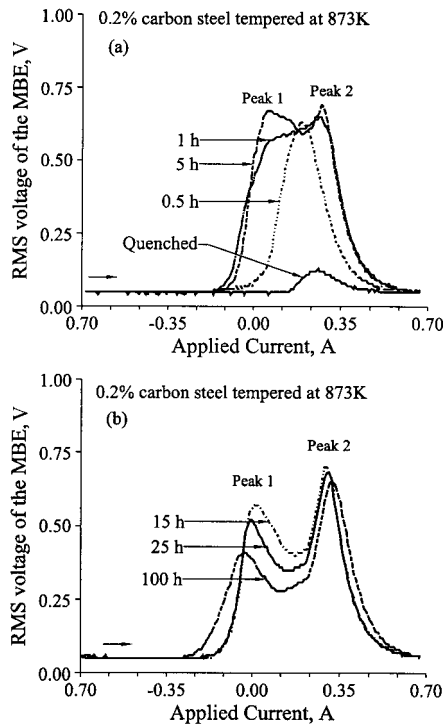
3   Variation in rms voltage profile of magnetic Barkhausen emission (MBE) for 0·2%C steel samples tempered at 873 K for different times[11]

4   Variation in *a* MBE peak 1 position and *b* reciprocal of average grain size with tempering time at 873 K for 0·2%C steel[53]

ferromagnetic materials are free from stresses. An excellent review has been written by Mikheev and Gorkunov[35] on the effect of various microstructural features on the magnetisation process and hence on the coercive force. Since the grain boundaries in polycrystalline materials separate regions of different crystallographic orientation or easy direction of magnetisation, they posses magnetic free poles.[36] It has been shown theoretically that the magneto-static energy associated with grain boundary free poles depends on the volume of the grain and the angular separation of the easy magnetisation direction in adjacent grains.[36] The changes in the grain boundary magneto-static energy decide the magnetic field required for the formation of reverse domains at grain boundaries and to overcome the resistance offered by the grain boundaries to domain wall movement during cyclic magnetisation.[35,36] The increasing magneto-static energy with increase in grain size facilitates reverse domain wall movement during the reverse magnetisation process. Also, the grain size decides the mean displacement of domain walls. Hence, the coercive force H_c is strongly influenced by average grain size. Based on this, an empirical relation has been obtained between grain size and H_c (in oersted) as

$$H_c = (A/d_g) + B \qquad \ldots \ldots \ldots \ldots (12)$$

where d_g is the grain size (in centimetres) and the coefficients A and B depend upon the degree of alloying and the character of the alloying elements. Much experimental verification carried out in iron and carbon steels showed the inverse linear relationship between H_c and d_g.[35–40]

The MBE technique has also been used to estimate the grain size in ferromagnetic materials. In most MBE studies, the peak height from the plot of rms voltage of the MBE signal versus magnetic field/applied current or the M parameter, the pulse amplitude that divides the total area under the pulse height distribution plot into two equal parts, is generally used for the analysis. Several studies have been made correlating the MBE to grain size ranging from 5 to 300 µm in materials such as pure iron, nickel and carbon steels with different microstructures.[9,41–48]

Generally, it has been observed that MBE peak height decreases and the peak position shifts to lower field with increase in grain size. Sundstroem and Torronen[48] reviewed the successful use of MBE for grain size determination in low carbon ferritic and ferritic and pearlitic steels. Tiitto[9] showed a linear correlation between the M parameter derived from the MBE pulse height distribution and the grain size in low carbon ferritic and pearlitic steels. However, in many cases, particularly in alloy ferritic steels, the linear correlation between MBE and grain size has not been observed.[46,49,50] The MBE level is affected by the chemical composition and microstructure. Segregation of impurities and presence of precipitates at the grain boundaries further complicate the magnetisation process by affecting the nucleation of domains and the movement of domain walls.[43,51] In the case of ferritic steels, the micromagnetic parameters are affected by the synergistic influence of microstructural features (such as grain boundaries,
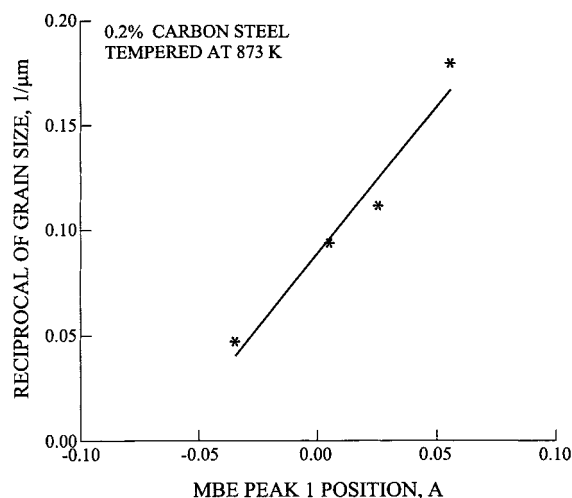
5 Relationship between MBE peak 1 position and average grain size for tempered (873 K) 0.2%C steel samples (correlation coefficient = 0.96)[53]

second phase precipitates, dislocations) and stresses on the magnetisation process. To separate unambiguously the influences of microstructural features and residual stresses on micromagnetic parameters, numerical modelling is being applied using advanced tools of mathematical approximation theory, i.e. multiregression algorithms and neural networks.[1] Based on the existing theories on the interaction of grain boundaries and inclusions/precipitates in tempered microstructures, Moorthy and co-workers[11,52] have proposed a two-stage magnetisation process considering the grain boundaries and precipitates to act as obstacles to domain wall movement in different field ranges. They have established that, by proper optimisation of instrumentation parameters such as magnetising frequency and time constant of the rms voltmeter for MBE signal integration,[53,54] it is possible to resolve the individual effect of grain boundaries and precipitates on the magnetisation process from the MBE profile. They have shown that the plot of rms voltage of the MBE versus current applied to the electromagnetic yoke systematically changes from a single peak to two peaks with increase in tempering time in carbon steel and Cr–Mo steels as typically shown in Fig. 3a,b.[11] Based on the two-stage magnetisation process,[11] the MBE peak 1 at lower field has been attributed to the influence of martensitic lath/ferrite grain boundaries and the MBE peak 2 at higher field has been attributed to the influence of carbide precipitates. As mentioned above, since the formation and growth of reverse domains would become increasingly easy with increase in grain size due to large demagnetising field at the grain boundaries, the MBE peak 1 position would shift to lower magnetic field as shown in Fig. 3. The correlation between MBE peak 1 position and grain size is further substantiated by comparing the variations in the MBE peak positions with the kinetics of grain size variation during tempering (Fig. 4a,b). The excellent correlation between the MBE peak position and grain size (Fig. 5) supports the view that the MBE technique can be used to resolve the effect of grain boundaries and precipitates and thereby to estimate the average
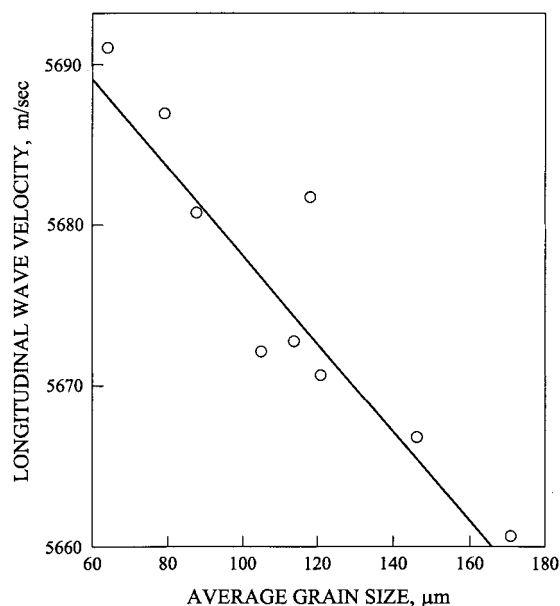
6 Variation in ultrasonic longitudinal velocity with grain size in AISI type 316 stainless steel[58]

grain size more accurately in tempered ferritic steels.[53] However, it has been observed that the individual effect of grain boundaries and precipitates can be resolved from the MBE profile only when the dislocation density is low and the precipitate size is sufficiently large (>150 nm).

Grain size measurements by ultrasonic methods
Over the years, several studies have been carried out to correlate ultrasonic parameters with grain size in various metallic materials. As mentioned above in the section 'Ultrasonic techniques', attenuation of ultrasonic waves is essentially due to scattering at grain boundaries.[15] Ultrasonic attenuation has been successfully correlated with grain size in ferritic steels (with various microstructures such as ferrite, pearlite, tempered bainite and tempered martensite), austenitic stainless steels, Ti alloys, etc.[55] In low carbon steels, the attenuation has been found to increase rapidly with grain size up to about 0.2 mm and then more slowly and linearly at larger grain sizes.[15] This has been attributed to the variation in scattering mechanisms associated with different grain size ranges (*see* 'Ultrasonic techniques').

In most cases, ultrasonic attenuation has been found to increase linearly with effective grain size irrespective of the microstructure, as the grain size in most materials is much lower than the wavelength of the ultrasound normally used in practice.[56] The main problems associated with the attenuation method are the estimation of corrections for couplant and diffraction. Hence, as an alternative, ultrasonic velocity measurements are being used for grain size estimation.[15,57–59] Accurate velocity measurements can be made using ultrasonic longitudinal and shear waves using the pulse–echo overlap technique. It has been observed that ultrasonic velocity decreases with increase in grain size (in the range 60–110 μm) in AISI type 316 austenitic stainless steel (Fig. 6),[58,59] while Ti alloy and maraging steel display an increase in ultrasonic velocity with increasing grain size.[60]

However, in both cases, a linear relationship was found to exist between the velocity and the metallographically estimated grain size. In the case of AISI type 316 stainless steel, it has been found that, for a given grain size range, the change in shear wave velocity is greater than that in longitudinal velocity for waves of the same frequency. For example, for a grain size range of 60–170 μm, the change in shear wave velocity is 1·23%, whereas the change in longitudinal wave velocity is only 0·5%. The observed increase or decrease in ultrasonic velocity with grain size in different materials can be rationalised based on a theory proposed by Hirsekorn.[61,62] According to her theory, the product of the wave number k and the average grain diameter d, i.e. kd, is the deciding factor for the change in velocity with grain size. The velocity would go through a minimum when the conditions (grain size–wavelength combination) are favourable for resonance interaction between the ultrasonic waves and the grains.

A comparative study[58] indicated that a best confidence level of 90% in the grain size estimation was achieved using velocity measurements, whereas attenuation measurements using first back wall echoes gave only 80% confidence level. Unlike the attenuation methods, velocity measurements were also found to be more or less unaffected by changes in the grain size distribution.

It has been observed that both attenuation and velocity measurements are affected by couplant condition, error in thickness measurement, attenuating properties of the material, thickness, etc. In an attempt to overcome these difficulties, recently Anish Kumar et al.[63] have used an ultrasonic spectral approach for grain size estimation. The shift in the spectral peak frequency and the change in the full width at half maximum (FWHM) of the auto power spectrum of the first back wall echo are correlated with the grain size in AISI type 316 austenitic stainless steel.[63,64] This shift in peak frequency has been explained with the help of the ultrasonic attenuation theory and spectral analysis of the ultrasonic waves. The spectrum power distribution depends on the ultrasonic attenuation and frequency. As the attenuation increases, the spectral power at the higher frequencies decreases. This leads to the decrease in peak frequency and FWHM of the auto power spectrum with increase in attenuation. As mentioned above, ultrasonic attenuation α increases with the third power of grain size d and the fourth power of frequency f in the Rayleigh regime (i.e. $\alpha \propto d^3 f^4$). Hence, as the grain size increases, attenuation increases and the peak frequency and FWHM of the auto power spectrum shift towards lower values. A Hall–Petch type relationship is found for peak frequency and FWHM with grain size as shown in Fig. 7. Therefore, these ultrasonic parameters can be linearly correlated with yield strength, if there is no other microstructural variation such as precipitation of second phases and other phase transformations which would affect the yield stress.

A similar spectral approach has also been used to estimate prior austenite grain size in 9Cr–1Mo steel samples solutionised at different temperatures.[64,65] The ratio of the two peaks in the auto power spectrum
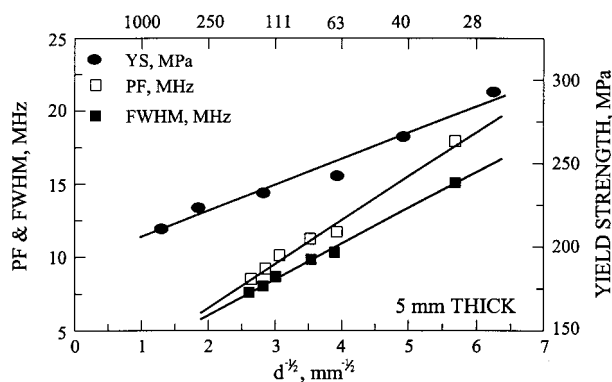
7 Variation in peak frequency (PF), full width at half maximum (FWHM) and yield strength with $d^{-1/2}$ for AISI type 316 stainless steel[63]

of the first back wall echo has been linearly related to grain size in the range from 20 to 120 μm. The peak frequency and FWHM in the auto power spectrum were found to be independent of couplant condition for a given specimen. This has an important practical significance, i.e. if the variation of these spectral parameters with grain size is used for grain size measurement, then the error involved in the measurements due to variation in the couplant condition can be minimised for on-line and/or a large number of measurements to be made by moving the plate/transducer.

Critical assessment of MBE and ultrasonic methods for grain size measurement

In situ metallography is a realistic method for obtaining the grain size in service exposed components, but the technique is limited by the prolonged time for obtaining good average information. For grain size estimation in ferromagnetic materials, the MBE technique is found to be more appropriate as compared to the hysteresis loop parameters. This is because the coercive force H_c is influenced by changes in dislocation density, residual stresses and second phase precipitation. It is not possible to distinguish the individual variation of grain size and precipitation from the coercive force measurement. However, the MBE could resolve the individual effect of grain size variation in sufficiently tempered or aged ferritic steels and the MBE peak position can be used for quantitative estimation of grain size. However, optimisation of experimental parameters, such as excitation frequency of magnetisation and time constant of the rms voltmeter for MBE measurement, is crucial for resolving the grain size effect. In this area, further work is needed in a wide range of ferritic steels.

Ultrasonic attenuation shows a linear relationship with effective grain size irrespective of the microstructure. However, the attenuation measurement is strongly affected by couplant condition and diffraction for which applying correction is quite inaccurate. The use of non-contact electromagnetic acoustic transducers (EMAT) would eliminate this problem. The relationship between ultrasonic velocity and grain size is decided by the product of the wave number k and the average grain size d. The velocity would go through a minimum when the conditions (grain size–

wavelength combination) are favourable for resonance interaction between the ultrasonic waves and the grains.[66,67] It is essential to know the grain size of interest in order to choose the correct probe frequency for using the established calibration graph. Analysis of the ultrasonic frequency spectrum gives better correlation with grain size and also overcomes the difficulties encountered in attenuation and velocity measurements. The peak frequency and the FWHM of the ultrasonic frequency spectrum have linear relationship with grain size and also these two parameters are found to be independent of couplant condition.

Evaluation of prior cold work, recovery and recrystallisation using NDE techniques

Ultrasonic and magnetic NDE techniques have been used to assess cold work in AISI type 304 stainless steel and the associated microstructural changes such as dislocation substructure evolution, α'-martensite phase formation, and texture formation. Since the X-ray and neutron diffraction techniques are well established for texture determination and substantial information is available in literature, those techniques are not discussed in this review.

Ultrasonic methods

Since ultrasonic parameters are influenced by bulk material phenomena, microstructural changes such as dislocation density, texture and grain size variation can be characterised using the ultrasonic parameters.

Ultrasonic velocity
Extensive studies[56,68–70] have been carried out to establish the variation in the three ultrasonic longitudinal wave velocities (V_{11}, V_{22} and V_{33}, i.e. velocities in the rolling (1), transverse (2) and normal (3) directions) and six shear wave velocities (V_{12}, V_{21}, V_{23}, V_{32}, V_{13}, V_{31}) with polarisation and propagation in rolling/transverse/normal directions (first subscript number indicates propagation direction and second subscript number indicates polarisation direction) with different degrees of cold work and the effect of subsequent annealing. It was found that the longitudinal velocities vary non-linearly with cold work in AISI type 304 stainless steel (Fig. 8a): this behaviour has been attributed to the formation of α'-martensite due to cold rolling.[56,68] However, all the six shear wave velocities decreased nearly linearly with increase in cold work (Fig. 8b). This difference in the behaviour of longitudinal and shear velocities is attributed to the predominant influence on shear velocities of texture in comparison to α'-martensite. Based on the velocity differences, V_{31} and V_{32} were established as the best parameters for estimating the extent of cold work. It should be mentioned that, while only one transducer is needed for measurement of V_{31} and V_{32}, it is necessary to know the specimen thickness. However, the use of velocity ratios would eliminate this difficulty and only the transit times would be adequate. Considering the ease with which the velocities of longitudinal and shear waves propagating in the normal (thickness) direction can be measured, the ratios V_{33}/V_{31}, V_{33}/V_{32} and V_{31}/V_{32} were estimated. The variations in these ratios with cold work showed large increase in the ratio V_{33}/V_{32}, increasing almost
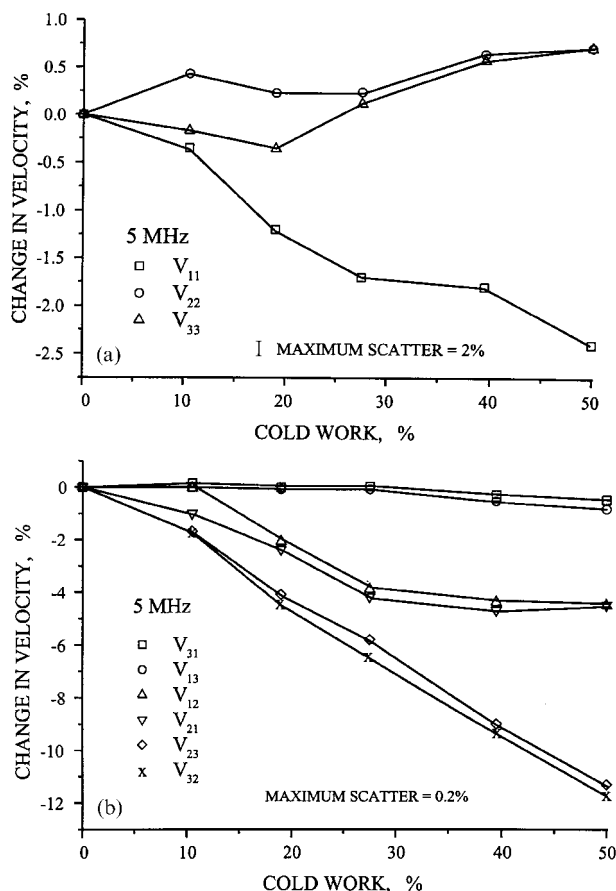
a variation in ultrasonic velocity of longitudinal waves having different propagation directions (V_{11}, V_{22}, and V_{33} are velocities in rolling (1), transverse (2), and normal (3) directions); *b* variation in ultrasonic velocity of shear waves having different polarisation and propagation directions (first and second subscript numbers indicate propagation and polarisation directions respectively)

8 Effect of degree of cold work on ultrasonic wave velocity in AISI type 304 stainless steel[56]

linearly with increase in cold work. A straight line fit between the ratio V_{33}/V_{32} and the per cent cold work (%CW) has been obtained as given below with the correlation coefficient of 0·99

$$(V_{33}/V_{32}) = 0.00527(\%CW) - 1.83 \quad . \quad . \quad . \quad (13)$$

Using equation (13) and measuring the velocities of the longitudinal and shear waves (shear waves polarised in the transverse direction) propagating in the rolling direction, the degree of cold work can be estimated with good precision.

Palanichamy *et al.*[70] have shown that the variation in shear wave velocity with annealing time exhibits three-stage behaviour in cold worked D9 alloy (Ti modified austenitic stainless steel). The shear wave velocity increases slowly corresponding to the recovery region and then sharply during the progress of recrystallisation and reaches saturation on completion of recrystallisation. During the progress of recrystallisation, the longitudinal velocity decreased sharply in contrast to the behaviour of shear wave velocity. They have also shown that the degree of recrystallisation can be quantified from a ratio comprising shear wave velocities in different polarisation directions (Fig. 9).[70]

$$Y = 0.05165 - 0.1009X + 0.05795X^2$$
$$R^2 = 0.9993$$
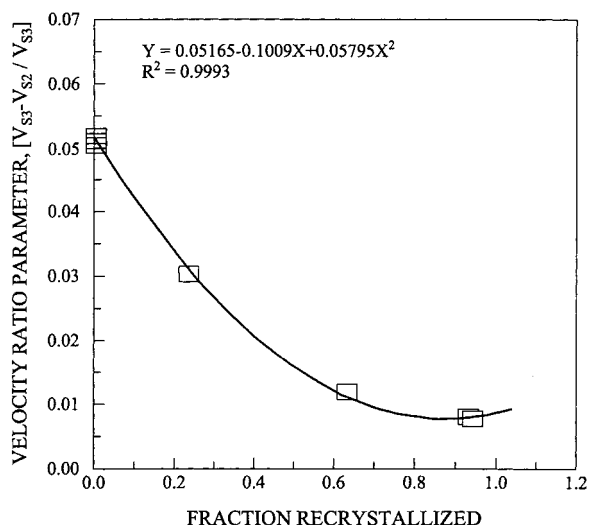
9   Variation in shear wave velocity ratio parameter with extent of recrystallisation in alloy D9 (Ti modified austenitic stainless steel)[70]

10   Variation in ultrasonic absorption with cold work in AISI type 304 stainless steel[56]
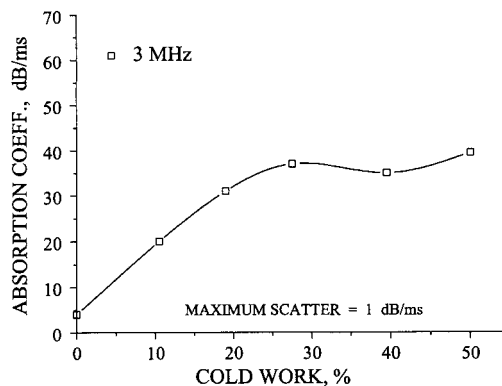
Ultrasonic attenuation

The influence of cold work on the ultrasonic attenuation in different directions was evaluated in austenitic stainless steel.[56,68] The attenuation in rolling and transverse directions increased slightly after a small amount of cold work and then decreased with further increase in cold work. The decrease in attenuation with cold work in all directions was attributed to the reduced scattering associated with the formation of texture or reduced anisotropy. Cold working enables formation of texture, which results in reduced misorientation among adjacent grains by rotation of grains to accommodate the strain. The scattering is reduced due to the reduction in the misorientation between adjacent grains, which enables the beam to be channelled through the specimen.

Ultrasonic absorption

Jayakumar[56] studied the influence of cold work on ultrasonic absorption in AISI type 304 stainless steel. The absorption measurements were carried out using a reverberation technique.[71] The absorption was found to increase with increase in cold work up to about 30% and then reach saturation (Fig. 10). It is suggested that the increase in absorption with increase in cold work up to 30% was due to an increase in dislocation density and the associated dislocation damping with cold work. Subsequent saturation in the absorption beyond 30% cold work was attributed to the competing influences on ultrasonic absorption from the formation of dislocation cell structure, which reduces absorption, and the formation of magnetic bcc α'-martensite, which increases absorption due to magnetic losses. This study qualitatively shows that the absorption measurement would indicate the percentage increase in strain induced α'-martensite and the stage where the dislocation cell structure begins to form.

Magnetic methods

Micromagnetic methods such as magnetic hysteresis loop, MBE and ABE can be used to characterise the microstructural changes due to cold working, recovery and recrystallisation in ferromagnetic materials as they are strongly influenced by the variation in dislocation density and its substructure, grain size, texture, etc.

Hysteresis loop measurements

The magnetic hysteresis loop parameters coercive force H_c, residual induction B_r and maximum permeability μ_{max} have been used to assess cold rolled or hot rolled ferritic steels. It has been generally observed that the H_c increases with percentage cold work. Also these parameters have been used to inspect the annealing of rolled steels. During annealing, the different stages such as recovery and recrystallisation can be identified from changes in these magnetic parameters.[72,73] During the recovery stage, the H_c decreases more rapidly compared to the rate of reduction during the recrystallisation stage. However, the behaviour of magnetic parameters cannot be generalised for a wide variety of ferritic steels.

When magnetic hysteresis loop measurements are made on a material having ferromagnetic second phase dispersed in a paramagnetic matrix or vice versa, the hysteresis loop shape would reflect the changes in the ratio of the ferromagnetic to non-ferromagnetic phases. Jayakumar and co-workers[56,74] have taken magnetic hysteresis loop measurements for AISI type 304 stainless steel specimens with 0–50% cold work. They have shown that the hysteresis loop shears with increase in cold work, which was attributed to the demagnetisation effect due to the presence of magnetic dipoles on the surface of the ferromagnetic second phase (α'-martensite). The observed increase in coercivity with increase in degree of cold work was attributed to the generation of stronger barriers through the deformation of already formed α'-martensite and the increased amount of dislocation density. The slope of the hysteresis loop given by $\Delta V/\Delta H$ was measured for different cold worked specimens. The variation of this slope showed that the slope increases with increase in the degree of cold work. Since the ΔH is same for all the specimens, the increase in $\Delta V/\Delta H$ indicates that the intensity of magnetisation I increases with increase in degree of cold work. This is attributed to the increase in the amount of α'-martensite with increase in degree of cold work. The digitised induced voltage V from the coil was rectified and then integrated over the full

cycle of the magnetisation using a microcomputer and the variation in this parameter ($\int V \mathrm{d}t$) with per cent cold work showed that the integrated area of the induced voltage signal increases with increase in degree of cold work. The variations in both $\Delta V/\Delta H$ and the area of the hysteresis loop with degree of cold work are very similar indicating that both these parameters can be used to determine the amount of α'-martensite formed with the increase in degree of cold work. These two parameters can detect α'-martensite even in specimens cold worked as little as 10%.

Magnetic Barkhausen emission (MBE) measurements
Similar to the coercive force, the MBE level is also influenced by cold work. The change in dislocation density and its substructure, the formation of texture, etc. would influence the MBE level. Normally, cold working in ferromagnetic materials is expected to reduce the MBE level due to increase in dislocation density, as it would reduce the domain wall displacement. The dislocation substructure would also influence the MBE level. The preferred $\langle 100 \rangle$ texture induced domain alignment will enhance the domain wall movement in a narrow field range and increase the MBE level in that direction. The measurement of variation in MBE level from the rolling direction to a transverse direction by rotation of magnetisation direction would indicate the presence of any texture. Tiitto[75] has studied the effect of texture in AISI 430 ferritic stainless steel sheet with a wide variety of textures. The MBE level relative to rolling and transverse directions varies over a wide range from one texture type to another. However, high MBE level is observed in $\langle 100 \rangle$ texture. In cases where superimposition of several texture types takes place, the interpretation of MBE response becomes complex. However, it is possible to identify sheet quality from the distribution of MBE level.

In the case of austenitic steels, the stress induced ferromagnetic phase formation during cold working would contribute to the magnetisation and hence to the MBE. Jayakumar and co-workers[56,74] measured the rms voltage of the MBE signals for different cold worked specimens of AISI 304 stainless steel at 50 mHz and 1 Hz applied field frequencies. There is a gradual increase in peak height and broadening of the MBE signal with increase in cold work (Fig. 11). Two parameters, half the difference in the magnetic field corresponding to the two peaks of the MBE signal H_{cm} and the maximum amplitude M_{max} of the rms voltage of the MBE signal, were estimated. The M_{max} value was found to increase with increase in degree of cold work and frequency of applied magnetic field. The increase in M_{max} was more pronounced in specimens with higher degree of cold work ($> 20\%$) and at higher frequencies of applied field (1 and 10 Hz). The increase in M_{max} with increase in frequency of magnetic field was attributed to the higher rate of movement of domain walls with increase in applied field frequency causing higher induction in the pick-up sensor. The increase in M_{max} with increase in degree of cold work is attributed to the increase in amount of α'-martensite. The MBE measurements can also be used, particularly at higher
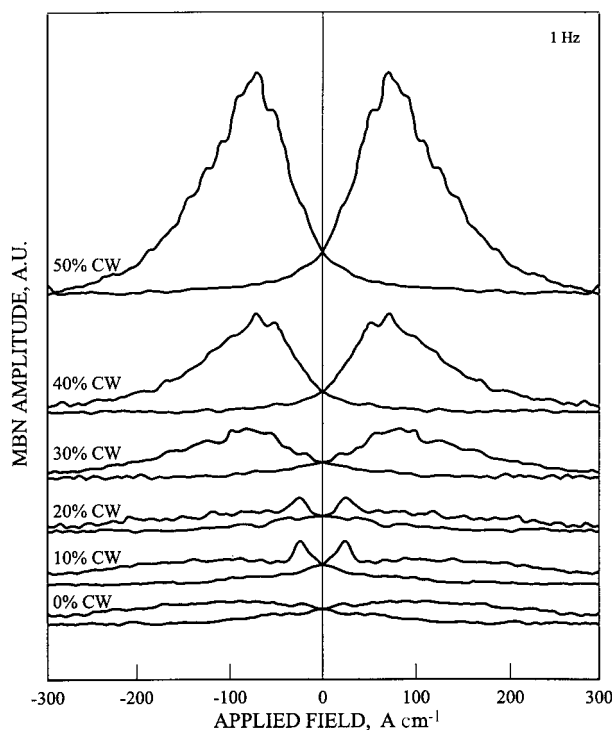
11 Variation in MBE amplitude with applied magnetic field in cold worked AISI type 304 stainless steel[74]

applied field frequency, to detect the presence of α'-martensite even in 10% cold worked specimens. It was established that MBE analysis could be utilised advantageously over hysteresis loop measurements for assessment of stress induced α'-martensite in nonstandard/irregularly shaped objects/components and at localised regions.

Acoustic Barkhausen emission (ABE) measurements
As mentioned above under the heading 'Micromagnetic NDE techniques', ABE is generated by the movement of 90° domain walls or the domain rotational process, which involves strain redistribution. Cold working would change the domain structure in order to lower the magnetic free energy. Hence, an increase in the extent of cold work tends to increase the number of 90° domains formed. The movement of these 90° domain walls would contribute to ABE. An increase in dislocation density restricts the movement of 90° domain walls. Hence, the ABE level is decided by the opposing effects of number of moving 90° domain walls and their displacement.[76,77] In the case where there is formation of strain induced α'-martensite, being small in size, the α'-martensite would have single domain structure. In such cases, the domain rotation process would contribute to ABE. Jayakumar and co-workers[56,74] have studied the ABE signal for different degrees of cold work in AISI type 304 austenitic stainless steel and shown that the ABN signal could be observed only in the 50% cold worked specimen. This was attributed to the presence of high dislocation density in martensite and very low volume of the magnetic phase. The magnetic field at which the ABE signal was observed in the 50% cold worked specimen was very high

(approximately 450 A cm^{-1}) indicating that single domain rotational processes could mainly be contributing to the observed ABE signal. In spite of the weak ABE signal generated in the cold worked AISI type 304 stainless steel, ABE measurement in the case of the 50% cold worked specimen could provide valuable information, namely, the martensite platelets are very small even after 50% cold work, i.e. of the order of the size of single magnetic domains, which otherwise needs extensive TEM investigations.

Critical assessment of NDE methods for measurement of cold work

The percentage cold work can be estimated from the ratio of the ultrasonic velocities in different directions. The ultrasonic attenuation varies non-linearly with cold work due to opposing influences of increase in dislocation density, which increases absorption, and the formation of texture induced anisotropy, which reduces the scattering. It is not possible to resolve the individual contribution of these two effects. However, it is possible to identify the phase transformation due to cold working from the changes in ultrasonic absorption.

The magnetic hysteresis loop and MBE techniques can be used to qualitatively assess the percentage cold work, recovery and recrystallisation in ferritic steels. Magnetic measurements have the potential to assess the different stages of dislocation substructure evolution during cold working, recovery and recrystallisation processes in rolled or forged ferritic steels. Further research work needs to be pursued in this area for characterising the microstructural evolution during various forming operations in ferritic steels. It is possible to detect the occurrence of texture in rolled sheets by measuring the MBE level in different directions, but identifying the type of texture is difficult. Only the $\langle 100 \rangle$ texture gives prominent changes in the magnetic parameters. It has also been found that the magnetic parameters can be used to detect the formation of a ferromagnetic phase in a non-magnetic matrix due to cold working. The formation of α'-martensite in AISI type 304 stainless steel cold worked as little as 10% could be detected, which is superior to the detection capability of TEM. Further work is required to explore these techniques for applications in assessing the quality of forming operations based on the microstructural predictions.

Characterisation of precipitation and growth of second phases

It is well known that the tempering or aging process in most metallic systems results in the precipitation of alloying elements from supersaturated solid solution. In some steels, the strain accumulation due to forming processes such as cold rolling and forging would also induce the phase transformation resulting in duplex microstructure. Since the presence of second phases strongly affects the properties of the materials, it is very essential to identify the formation of second phases and determine their volume fraction. Many NDE techniques have been developed which are found to be sensitive to the precipitation and growth of second phases. This section discusses the various
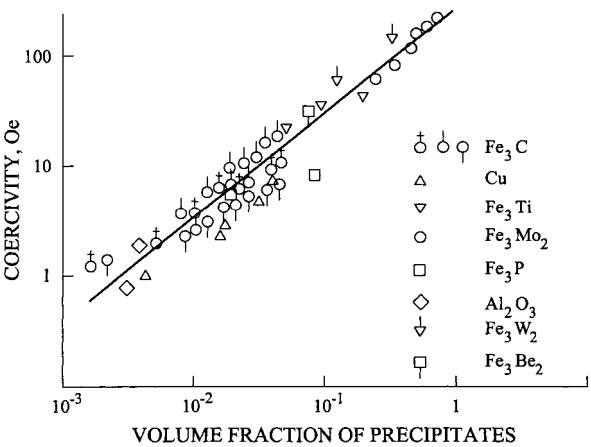
12   Coercivity of various steels as function of total volume fraction of inclusions[86]

NDE techniques that can be used for identification and quantification of second phases.

Micromagnetic methods

The size, shape, orientation, distribution, volume fraction and nature of the secondary phase (paramagnetic or ferromagnetic) have been found to influence the magnetisation process in ferromagnetic materials. The total magnetic energy of the domain walls changes from one location to the other in a matrix containing second phases due to (i) reduction in the domain wall energy caused by intersection of domain walls with second phases,[78] (ii) changes in the magneto-static self energy associated with the second phases/inclusions due to the movement of the domain walls, (iii) interaction of domain walls with closure/spike domains associated with the second phases, and (iv) magneto-elastic interaction due to the stress field around the second phases. These variations in the domain wall energy in ferromagnetic material influence the magnetisation process[79,80] and, in turn, the coercivity, the MBE and the ABE parameters.

Saturation magnetisation
When different phases having different magnetic properties are present, the saturation magnetisation would vary depending on the volume fraction of these phases as
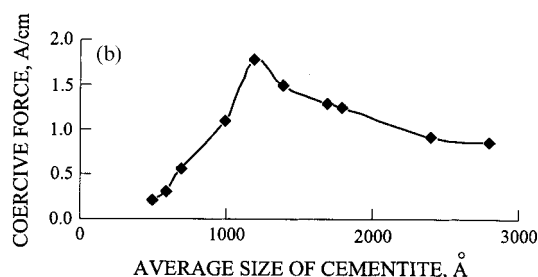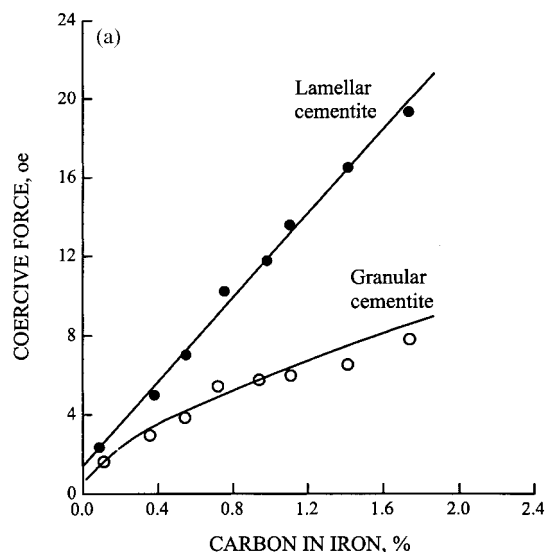
$$M_s = \sum_i V_i/100(M_s)_i \quad \ldots \ldots \ldots \ldots (14)$$

where V_i is the volume fraction of ith phase and $(M_s)_i$ is the saturation magnetisation of ith phase. When a martensitic steel contains residual austenite, the volume per cent of austenite V_a is given as

$$V_a = 100[1 - (M_s/M_m)] \quad \ldots \ldots \ldots (15)$$

where M_s is the saturation magnetisation of a test specimen containing both martensite and austenite and M_m is the saturation magnetisation of a standard specimen containing only martensite.

Based on the above, the ratio of volume fraction of non-ferromagnetic to ferromagnetic phases can be determined. Many studies have been carried out on the quantitative estimation of a paramagnetic phase in a ferromagnetic matrix by measuring M_s. Mikheev and Gorkunov[81,82] have written an excellent review

14 **Coercive force and extent of precipitation as function of tempering time at 523 K for Fe–0·02%C steel[78]**

a dependence of H_c on amount of C in steel in form of spheroidal and lamellar cementite;[36] b relationship of H_c to average size of cementite particles in steel[35]

13 **Effects of second phase on coercive force H_c for C steels (note that units of coercive force differ for parts *a* and *b*)**

on the analysis of phases using magnetic methods. The saturation magnetisation M_s has also been used to estimate the ferrite and martensite contents in duplex steels and transformation induced plasticity (TRIP) steels,[81] and residual austenite in carbon and low alloy steels.[82] However, the practical application of this method is difficult, as it requires the large magnetic field strength for attaining saturation. The complex geometry of the component and the associated large demagnetising field also increase the difficulty.

Coercive force
Several studies carried out by both theory and experiment have shown that the coercive force is proportional to the volume fraction of second phases as[83]

$$H_c \propto V^n \qquad \qquad \qquad \qquad (16)$$

where V is the volume fraction of second phases/inclusions and n is an exponent depending upon the form of inclusion and may have values of 1, 2/3, 4/3, etc.[78,84,85] A comparison between the second phase/inclusion theory and the experimental values obtained for coercivity in steels containing different types of second phases/inclusions shows a good correlation between the coercivity and the volume fraction (Fig. 12).[86]

Some of these studies indicated that the relation is also influenced by the alloying content (for example

carbon content), volume fraction of second phases, and size and shape of second phases.[35,36,78,87–90] For example, in steels, it was found that H_c was proportional to $V^{2/3}$ only up to 2 wt-%C.[35] Similarly Goodenough[36] showed that, for lamellar forms, $H_c \propto V$ and for spheroids $H_c \propto V^{2/3}$. Figure 13*a* shows the variation in coercive force as a function of carbon content in iron for precipitation of cementite in lamellar and spheroidal shapes. For a given carbon content, the lamellar shape gives higher coercivity than spheroids. It is also observed that the coercive force depends not only on the shape and volume fraction of precipitates, but also on the size of the precipitates.[35] Figure 13*b* shows the relationship of H_c to the average size of cementite particles in steel. Dijkstra and Wert[78] observed that the H_c has maximum value when the size of the ferromagnetic cementite is comparable to domain wall thickness δ in steel. However, Dietze[87] showed that, for a steel with 2·14%Cu tempered at 710°C, the coercive force is maximum with non-ferromagnetic Cu precipitate size of about 5 to 6 times the domain wall thickness. This observation reveals that it is not only the size, but also the other magnetic properties of the inclusions that influence the coercive force.[91]

The coercivity generally increases with increase in the size of precipitates p when $p \ll \delta$. However, when $p \gg \delta$, the coercivity is found to decrease because of the easy nucleation of reverse domains at precipitate/matrix interfaces. The peak in coercivity was found by Dijkstra and Wert[78] when the size of Fe_3C reached 1400 Å (after ~ 10 min at 523 K) in the case of an iron alloy with 0·02%C (Fig. 14). The extent of progress in precipitation with time is also shown in Fig. 14. As already discussed above, the coercive force is also influenced by the variation in grain size and dislocation density in a synergistic manner. It is not possible to isolate the individual effects of these microstructural features from coercive force.

*Magnetic Barkhausen emission (MBE) technique*
As mentioned above, the pinning of magnetic domain walls by the lattice distortion due to the strain field and the magneto-static interaction of secondary phases is reflected in the variation of the MBE parameters. Many studies have been carried out to

understand the interaction of secondary phases during the magnetisation process[9,10,41,43,51,92–95] and it has been observed that MBE is more sensitive to the presence of second phase precipitates than the coercive force. Gatelier-rothea *et al.*[41] have compared the behaviour of MBE in pure iron, solid solution containing 130 ppm carbon and ferrite with intergranular cementite precipitation. They have observed the reduction in rms voltage of the MBE and broadening of the MBE profile in solid solution and in the presence of intergranular cementite precipitation. This indicates the pinning of domain walls resulted from the lattice distortion associated with the interstitial solutes and carbide precipitates.

Similar to the coercive force, MBE is also influenced by the type, size, shape and volume fraction of second phases. For example, the type of carbide, e.g. Fe_xC, was found to have a strong influence on the MBE as the magnetic response of the two phases is different.[9,42] The shape anisotropy and the stress field around coherent Fe_xC precipitates influence the domain wall movement more strongly than when around incoherent Fe_3C spherical precipitates. The influence of these factors on MBE has been studied by Tiitto[9] during aging of rimmed carbon steel at room temperature (298 K) and also at 523 K. During the early stage of precipitation of coherent Fe_xC, even though the particles are small in size, the overlapping stress fields restrict domain wall movement and hence lower the MBE level. The precipitation of Fe_3C spheroidal carbides gives higher MBE response and the MBE level goes through a maximum with aging time. However, the changes in dislocation density and coarsening of laths/grains have not been taken into consideration while explaining the MBE response.

Buttle *et al.*[76] have studied the effect of tempered microstructure of mild steel on the MBE activity profile for samples isochronally tempered at from 250 to 650°C for 1 h. They observed single peak MBE behaviour at lower tempering temperatures and two-peak behaviour at higher temperatures. Buttle *et al.*[93] have also studied the MBE and ABE from the domain wall interaction with precipitates in single crystal and polycrystalline Incoloy 904. In polycrystal, they observed three-peak behaviour in MBE and the peak heights go through a maximum as a function of aging time. After long term aging, only a single peak occurred. They have shown that MBE is more sensitive to smaller size precipitates than ABE, but for sizes greater than the domain wall width, both MBE and ABE are sensitive. They have suggested that ABE can be used to determine the larger precipitate size. Since, for smaller precipitates, ABE is insensitive, stress measurements can be made in Incoloy 904 using ABE.

Bhattacharya *et al.*[96] have studied the effect of precipitation in 17-4PH steel on MBE. In the quenched condition, 17-4PH steel has lath martensitic (soft bcc) structure. When aged in the temperature range 750–900 K, finely dispersed copper rich coherent phase precipitates. With increased aging time, loss of coherency and austenite reversion take place. Each of these different stages of aging can be identified from the MBE level. Figure 15 shows the variation in rms voltage peak of the MBE with aging time at
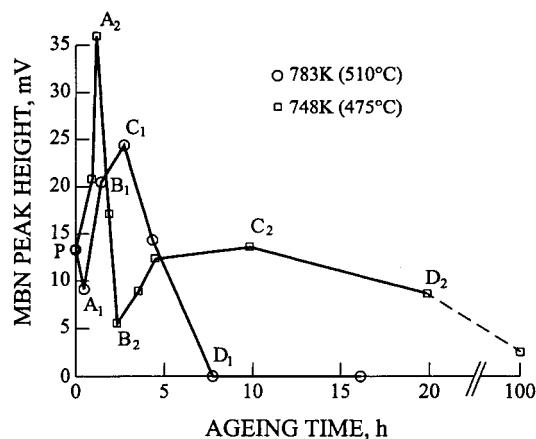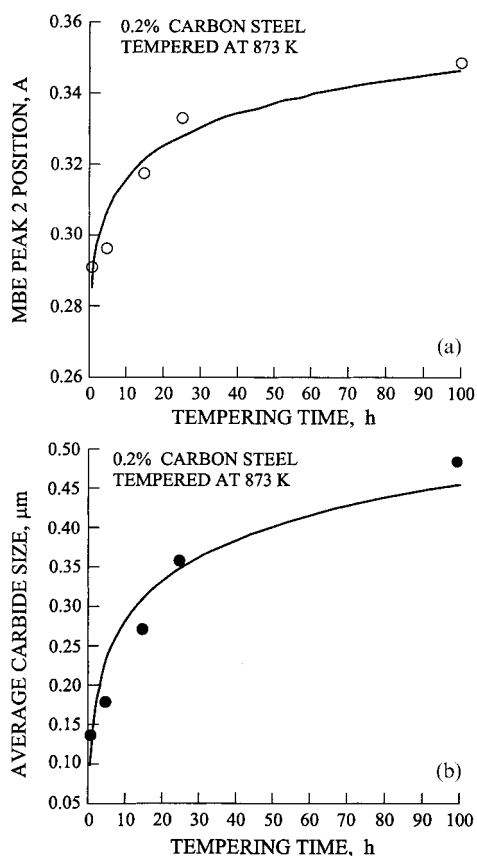

P–A_2: reduction in dislocation density; P–A_1/A_2–B_2: build-up of coherency strains through fine Cu precipitation; A_1–C_1/B_2–C_2: loss of coherency and growth of Cu precipitates; C_1–D_1/C_2–D_2: reversion to austenite (paramagnetic phase)

15 Variation in rms voltage peak of magnetic Barkhausen noise (MBN) signal with aging time at 748 and 783 K for 17-4PH steel[96]

748 and 783 K.[96] The MBE voltage peak decreases initially due to build up of compressive stresses in the matrix due to coherency strains associated with copper precipitation, which restricts domain wall movement. Subsequent loss of coherency due to growth of copper precipitates leads to increase in MBE signal due to lower resistance to domain wall movement. At longer aging times, due to precipitation of interlath austenite phase (a paramagnetic phase), the MBE signal again decreases. These observations clearly establish that the MBE level can be used to clearly identify the peak aging, overaging and austenite reversion stages in this steel. But, in contrast to the observations in this study, Altpeter *et al.*[97] have shown that copper precipitation increases the MBE level due to development of tensile residual stress in WB36 pressure vessel steel due to aging during service exposure. Therefore, it is essential to carry out systematic investigations to clearly understand the effect of coherent precipitation of second phases and the associated residual stress on MBE in precipitation hardened ferritic steels.
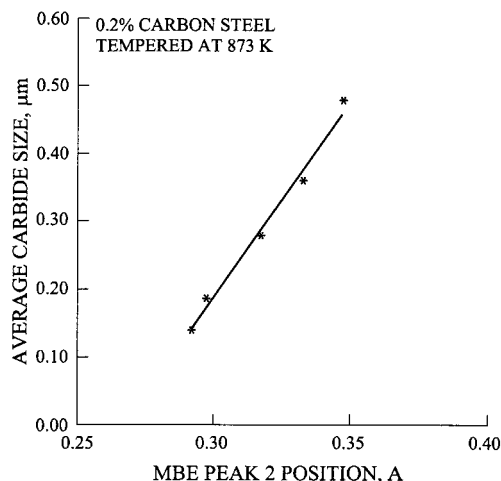
Similar to the effect of grain size, different results have been obtained by various investigators for different systems. In a carbon steel with cementite precipitation, Gatelier-rothea *et al.*[41] and Kameda and Ranjan[42] have observed single peak behaviour, whereas Buttle *et al.*[93] observed three-peak behaviour in MBE activity for Incoloy 904 with coherent spherical precipitates. Bhattacharya *et al.*[96] have observed only single peak MBE behaviour in the case of 17-4PH stainless steel with coherent copper precipitates. These studies show different MBE behaviour for similar systems where only the grain boundaries and second phase precipitates are major obstacles to domain wall movement. The single peak or multiple peak MBE behaviour may depend on the MBE instrumentation parameters, such as MBE coil frequency response, filter conditions and time constant of the integration of rms signal. For the instrumen-

16 Variation in *a* MBE peak 2 position and *b* average cementite size as function of tempering time at 873 K for 0·2%C steel[53]
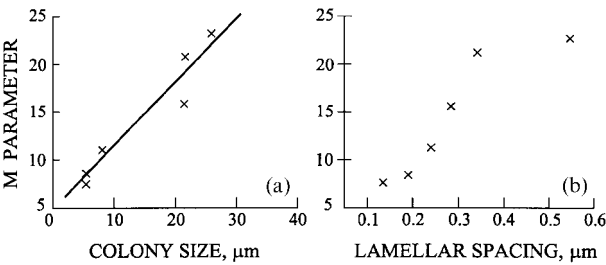

17 Relationship between MBE peak 2 position and average size of cementite precipitates for tempered (873 K) 0·2%C steel samples (correlation coefficient = 0·99)[98]

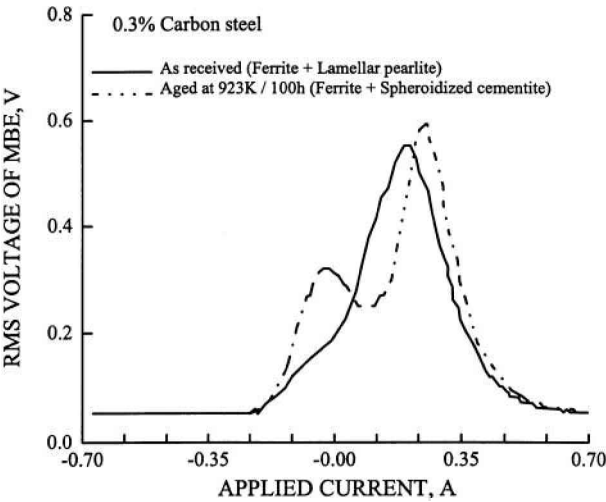variations in the lath/grain size and type and size of carbides.[11,98]

Based on the two-stage magnetisation process, it has been shown that the individual effect of variation in average grain size and average precipitate size can be resolved from the two-peak MBE profile (Fig. 3a,b). The correlation between the MBE and the average grain size has already been discussed (*see* above). Figure 16a and b shows the variation in MBE peak 2 position and the average carbide size as a function of tempering time. The perfect matching between the MBE peak position and microstructural features shows the strength of the proposed two-stage magnetisation process model. Excellent correlation between MBE peak position and microstructural parameter (Figs. 5 and 17) shows that the MBE technique can be used to evaluate the changes in grain size and precipitate size in long term aged ferritic steels. However, this is difficult in short term aged conditions, where the dislocation density is high, and the lath and precipitate sizes are very small.

Apart from the type of second phase, the shape is also found to influence the MBE. Altpeter[99] reported the different influences of lamellar and globular cementites on the MBE activity. She obtained a single peak MBE profile for lamellar structure and a two-peak MBE profile for globular structure. This has been attributed to the effect of long-range stress fields associated with the lamellar cementites and short-range stress fields associated with the globular cementites.[99] Also, a linear correlation has been established between the MBE parameter and cementite content in globular cementite structure and annealed structure.[8] Wafik and co-workers[94,95] reported that pearlite with lamellar cementite generates MBE with a higher number of jumps with higher amplitudes as compared to the structure with spheroidised cementite. Tiitto[9] showed that the MBE activity increases with increase in colony size and lamellar spacing in pearlite. Figure 18a and b shows the dependence of *M* parameter on pearlite colony size and lamellar spacing respectively.[9]
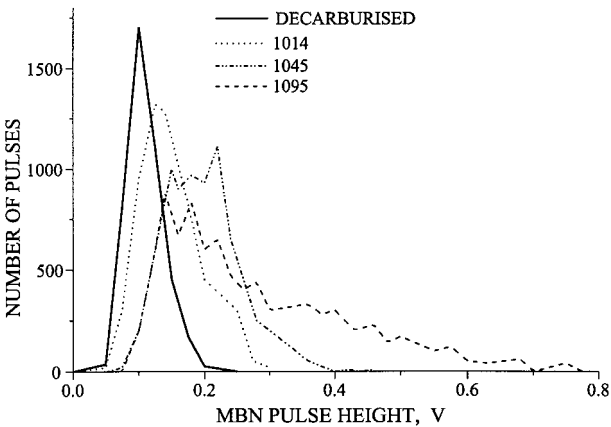
tation condition used by Bhattacharya *et al.*[96] a single peak MBE in 17-4PH steel has been observed. For the mechanisms of MBE generation, some investigators[42,93] have suggested that the domain nucleation process would be the major contribution to MBE and other researchers[41,45,92] have suggested irreversible domain wall movement as the major contribution to MBE generation without distinguishing the effect of different microstructural features.

Normally, during thermal aging, the dislocation density, size and distribution of laths/grains and second phase precipitates would vary in a synergistic manner. In none of these studies, has the effect of second phase precipitates and grain boundaries on the magnetisation process been distinguished. Recently, Moorthy *et al.*[52] have proposed a two-stage magnetisation process in sufficiently tempered microstructure considering grain boundaries and carbide precipitates as the two major types of obstacle to domain wall movement. They have also validated this by studying the influence on the MBE behaviour of tempered microstructure in carbon steel, 2·25Cr–1Mo steel and 9Cr–1Mo steel.[11] The MBE profiles for tempered specimens of these steel types can be found in Refs. 11 and 53. Based on the two-stage magnetisation process, the MBE peak 1 has been attributed to the influence of grain boundaries and peak 2 to that of carbides.[11,98] The systematic changes in height and position of the MBE peaks at different stages of tempering have been explained based on

18 Dependence of *M* parameter (derived from MBE pulse height distribution) on *a* pearlite colony size and *b* lamellar spacing in low C steel[9]

20 Pulse height distribution of MBE signal for decarburised (100% ferrite), 1014, 1045, and 1095 (100% pearlite) steels in annealed condition[92]

The MBE profiles in annealed and thermally aged 0·3%C steel samples have been analysed in the authors' laboratory to study the effect of lamellar and spheroidised cementite structures on the magnetisation process. The annealed sample having ferrite and pearlite microstructure showed a sharp slope change near the field transition ($H \approx 0$) and a dominant peak in the MBE profile, whereas the thermally aged sample having spheroidised cementite particles showed two peaks in the MBE profile (Fig. 19). The microstructural observation clearly shows that every ferrite grain has lamellar cementite boundaries on at least two sides. Hence, even in the ferrite grains, the domain walls cannot move a large distance, being restricted by pinning at grain boundaries with lamellar cementite. Therefore, the small peak (slope change) near the field transition in the MBE profile can be attributed to the domain wall movement in overcoming the ferrite grain boundary (without precipitates) resistance before they are pinned by the grain boundaries with lamellar precipitates. The dominant peak at higher field is attributed to the domain wall movement overcoming the resistance offered by the grain boundaries with lamellar precipitates. The spheroidisation of cementite during thermal aging increases the precipitate-free ferrite grain boundaries and hence the first MBE peak height near the field transition. The second peak becomes narrow and shifts to higher

**19 Difference in rms voltage profile of MBE for lamellar and spheroidised cementite structures in 0·3%C steel**

field indicating the spheroidisation of cementite and the stronger resistance of spherodised particles to domain wall movement. Once the lamellar structure changes into spheroidal, the grain boundaries and the granular cementite would act in different field ranges as explained elsewhere[11] resulting in a two-stage magnetisation process and hence the two-peak MBE profile. This study shows that it is possible to identify the spheroidisation of lamellar cementite during thermal aging from the MBE profile.

The MBE technique has been used to determine the volume fraction of the two phases in duplex steels. The influence of ferritic and pearlitic structure on MBE behaviour has also been studied.[92,95,100,101] Figure 20 shows the pulse height distribution of the MBE signal for decarburised (100% ferrite), 1014, 1045, and 1095 (100% pearlite) steels in the annealed condition.[92] It can be observed that the pulse height increases with increase in volume fraction of pearlite. In decarburised steel with ferrite structure, the pulse height is small but the number of pulses is very large. This has been attributed to the fact that the maximum domain wall jump was limited to ferrite grain size. But in the case of pearlite, adjacent colonies would have close orientation relationship because a pearlite nucleus, located at a grain boundary, would have grown into a very large number of contiguous colonies, all preferentially oriented with respect to one another. This would have led to larger mean free path for domain walls in pearlite than in the ferrite and, hence, results in MBE events with large pulse height with asymmetrical distribution in the fully pearlitic structure.

Recently, Vaidyanathan *et al.*[102] have established, from a study on the induction hardened case, the coexistence of one hard and one soft ferromagnetic phase (for example, martensite and ferrite) from the two-peak MBE profile. The variation in the volume fraction of ferrite and martensite phases has been directly observed from the height variation of the two peaks in the MBE profile. However, when there is formation of non-ferromagnetic austenite, the development of two peaks is not possible, because the austenite regions act as a strong barrier to the magnet-
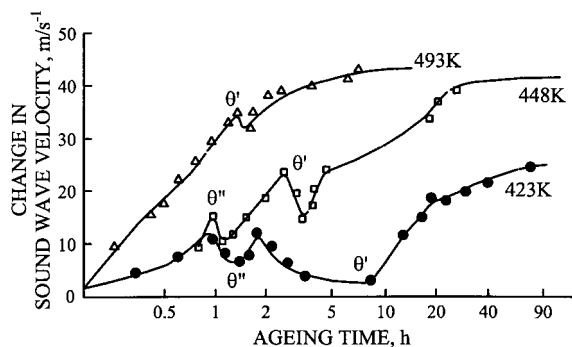
21 Change in sound wave velocity during isothermal aging of 2219 Al alloy: series of dips corresponds to maximal rate of formation of θ' and θ'' particles[103]

22 Variation in ultrasonic attenuation with aging time in 2219 Al alloy[103]

isation process and would drastically reduce the MBE below detection level.[96] In such cases, the measurement of saturation magnetisation M_s would give clear indication of the volume fraction of non-magnetic phases.[81,82]

Ultrasonic techniques

As already mentioned, the precipitation of second phases strongly affects the ultrasonic attenuation by scattering and absorption phenomena and also affects the ultrasonic velocities by changing the elastic properties. Several studies have been made on establishing the effect of second phase precipitation on ultrasonic parameters.

Aluminium alloys Precipitation hardening is an important metallurgical process applied to aluminium alloys whereby the strength and hardness can be augmented considerably. The ultrasonic velocity and attenuation parameters monitored continuously during the precipitation hardening process would provide insight into the kinetics and mechanism of precipitate formation and growth. Such a possibility has been studied extensively in aluminium alloys.[103,104] Figure 21 shows the aging time dependence of the changes of sound wave velocity in 2219 aluminium alloy during isothermal aging at three temperatures. The non-destructive characterisation of the aging process, as manifested in Fig. 21 and corroborated with optical and electron microscopy, hardness, strength and eddy current based conductivity data, indicated a series of dips that corresponded to the maximal rate of formation of θ' and θ'' particles.[103,105]

The variation in ultrasonic attenuation with aging time for the same Al alloy is shown in Fig. 22. The prominent peaks in the ultrasonic attenuation shown in Fig. 22 represented the loss of coherency of θ' particles with the matrix and the beginning of the softening process. The peaks in ultrasonic attenuation arise from the interaction between the acoustic vibrations of the ultrasonic waves propagating through the material and the interface dislocations surrounding θ' particles.

Nimonic alloy PE16 In Nimonic alloy PE16, the volume fraction of γ' precipitation strengthening phase has been correlated to the ultrasonic velocity.[106] The results clearly showed a linear relationship between volume fraction of γ' and velocity irrespective
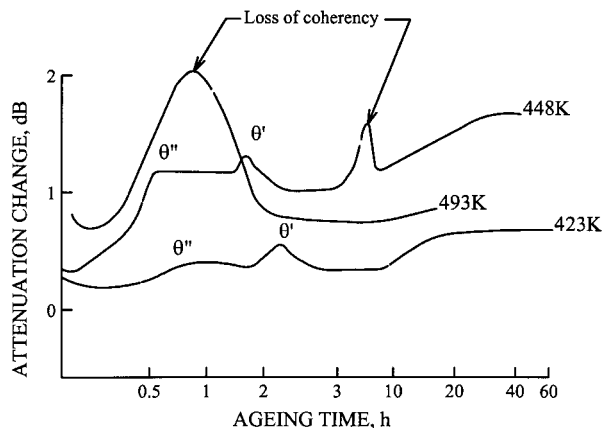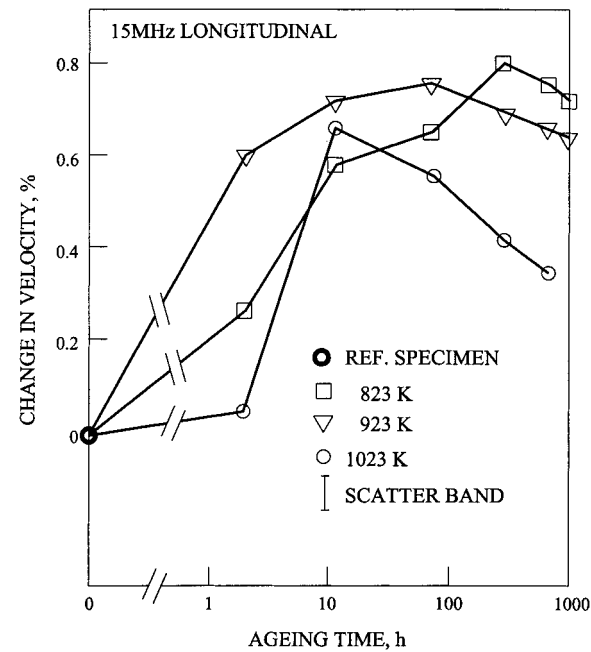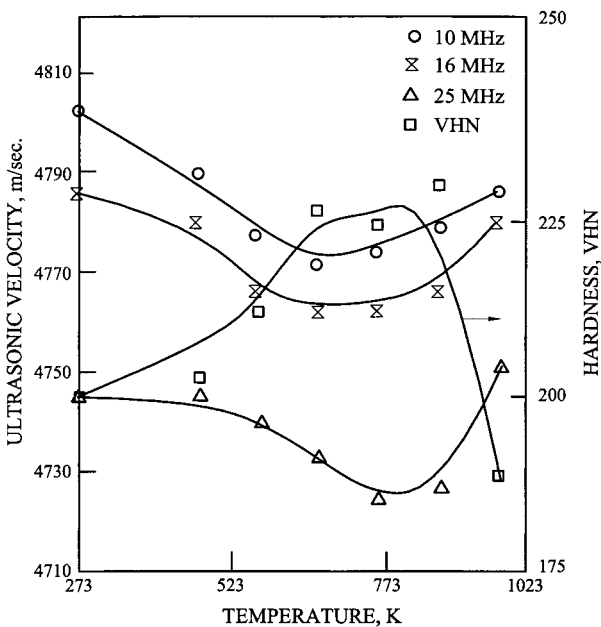
of the aging temperature. The ultrasonic velocity measurement can be used for detection of optimised microstructure and strength in heat treated alloy. The changes in the volume fraction of γ' in a component, which may occur during accidental rise in temperature in service, can also be detected. Similarly, ultrasonic velocity measurements in quenched and aged 17-4PH stainless steel have shown[106] that the precipitation of intralath copper rich precipitates increases the ultrasonic velocity by a factor of 1·5.

9Cr–1Mo ferritic steel This steel is used in the normalised (at 1323 K for 30 min) and tempered (at 1023 K for 1 h) condition. The tempered martensite with fine distribution of M_2X precipitates imparts optimum creep resistance. It has been observed that the coherency strain associated with precipitation of needle-like M_2X particles together with small amounts of ferrite formation (by dissolution of martensite) up to 1000 h during aging at 823 and 923 K and during initial periods of aging at 1023 K increases the ultrasonic velocity as shown in Fig. 23.[107] However, the dissolution of M_2X causes rapid coarsening of ferrite grains at longer aging periods at 1023 K and decreases the ultrasonic velocity. Therefore, any increase in velocity with time at a particular location on a component should indicate precipitation of essentially M_2X with very small or no ferrite formation. On the other hand, any decrease in velocity with time would indicate definite ferrite formation, an indication for degradation of the microstructure, as a result of dissolution of M_2X, which would reduce the strength of the material.

β quenched and thermally aged Zircaloy 2 During the fabrication of Zircaloy 2 components, β quenching is an important step. Precipitation of hard intermetallic phases, such as Zr_4Sn, $ZrFe_2$, $NiZr_2$, and $ZrCr_2$, and the presence of α phase in the β quenched billet are to be avoided. Ultrasonic velocity measurements carried out in the frequency range up to 25 MHz showed a decreasing trend with aging temperature up to 773 K, with an increase in the ultrasonic velocity indicated for a further increase in aging temperature (Fig. 24).[108] The dip in velocity has been found to coincide with peak in hardness, which is due to the presence of hard intermetallic phases. By specifying a minimum ultrasonic velocity as an acceptance

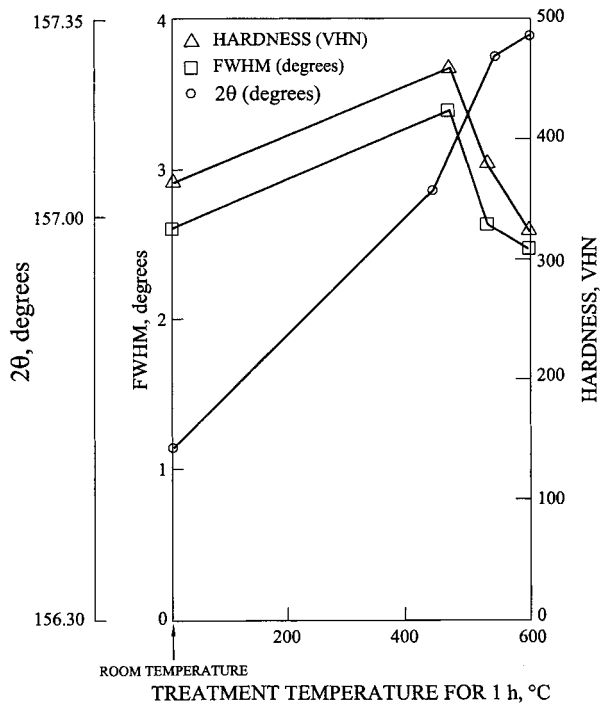23 **Variation of change in ultrasonic velocity with aging time for 9Cr–1Mo steel[107]**

24 **Variation in ultrasonic velocity and Vickers hardness with aging temperature of quenched and isochronally aged (for 1 h) Zircaloy 2 (10, 16 and 25 MHz)[108]**

25 **Variation in Vickers hardness and XRD parameters with temperature in isochronally aged 17-4PH steel**

interval 603–466 K was attributed to the formation of α'-martensite in the cold worked specimens during cooling after aging. A good correlation has been observed between the AE activity and the amount of α'-martensite formed in differently cold worked specimens. The temperatures corresponding to the beginning M_s and end M_f of α'-martensite formation during cooling after aging of cold worked specimens have been established. For the first time, ambiguity pertaining to the nature of this transformation as nucleation and growth type or shear type, has been resolved and the formation of α'-martensite has been shown to occur by a shear process.

X-ray diffraction (XRD) technique for assessment of aged condition during precipitation hardening

Hardness is normally used as a parameter to assess the aging status of microstructures. Hardness measurement cannot distinguish the underaged/overaged condition as both would result in lower hardness compared to the peak (optimum) aged condition. In a recent study on 17-4PH steel in the authors' laboratory, the FWHM and 2θ values of the diffraction peak of the XRD profiles of {211} reflections have been correlated to the hardness variations for isochronally aged samples (Fig. 25). The FWHM and hardness vary in a similar manner. The FWHM increases during the initial period of aging due to the microstrain associated with precipitation of coherent copper rich phases. At longer aging times, there is growth of copper precipitates and loss of coherency. This results in the reduction in microstrain and hence the reduction in FWHM at longer aging periods. The 2θ value of the peak increases continuously with aging temperature from the solution annealed state. As there is continuous change in the composition of

criterion, the absence of intermetallics in β quenched billets can be ensured.

Acoustic emission (AE) technique to study α'-martensite formation

The AE technique has been used to study α'-martensite formation in solution annealed and cold worked AISI type 304 stainless steel during cooling after aging for 1 h at 673 K.[109,110] The higher amount of AE generated in the cold worked specimens compared to in the annealed specimens in the temperature

26 **Variation in *S* parameter with aging time in Al–Cu alloy**[112]

27 **Variation in positron lifetime with annealing temperature for D9 alloy cold worked (CW) to 20 and 17·5% thickness reduction**[116]

the matrix due to precipitation of copper, there would be continuous change in the lattice parameter, which manifests as the continuous increase in 2θ value. This study shows that monitoring of both FWHM and 2θ value together could indicate not only the hardness but also the aging stage, i.e. whether underaged, peak aged or overaged.

Positron annihilation (PA) technique
Positron annihilation has been used to study the formation of precipitates in Al–Cu, Al–Zn, Fe–C, etc. alloys.[111–115] Decomposition of Al–Cu alloy during aging has been observed by measuring the variations of the fraction of positrons trapped in each family such as (i) vacancies in pure Al around GP1 zones, (ii) vacancies inside GP2 zones, and (iii) dislocation misfit regions around semicoherent and incoherent precipitates. Guinier–Preston (GP) zones are small precipitation domains in a supersaturated metallic solid solution. The zones do not have a well defined crystalline structure of their own and contain an abnormally high concentration of solute atoms. The formation of GP zones constitutes the first stage of precipitation and is usually accompanied by a change in properties of the solid solution in which they occur. The formation of GP zones usually coincides with changes in properties, for example increase in strength. Gauster and Wampler[113] studied the variation in *S* parameter during isochronal annealing for Al–Cu alloy containing various amounts (wt-%) of Cu. They observed that the *S* parameter is lower in Al–Cu alloy as compared to in pure Al.[113] This is attributed to the preferential trapping of positrons in Cu rich precipitate zones. The *S* parameter (Fig. 26) has been shown to identify the progressive dissolution of GP1 zones, growth of GP2 zones up to a critical size, and transformation of GP2 zones into θ' precipitates in Al–Cu alloys.[112] The transition from GP1 to GP2 does not cause any significant change in the *S* parameter. This is attributed to the retention of coherency with the Al lattice. The progressive transformation of GP2 zones into θ' is clearly indicated by a gradual drop in *S* parameter due to loss of coherency. Abis *et al.*[112] have related the constant positron lifetime observed beyond a certain aging time to the critical time at which transformation of GP2 zones into θ' begins.
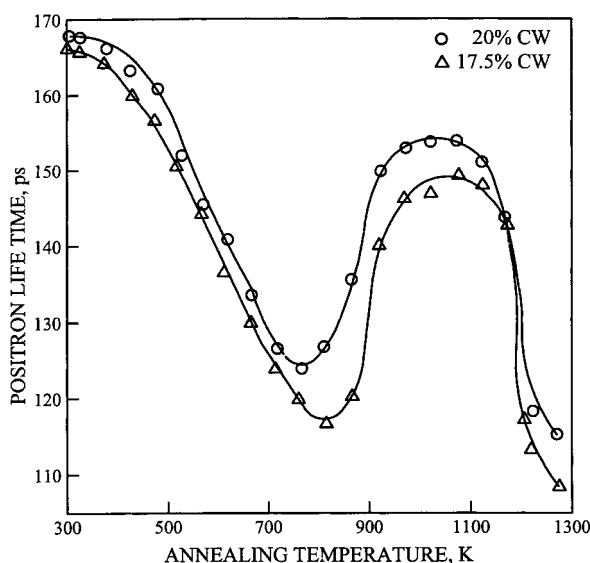
Positron annihilation spectroscopy has been used to study the kinetics of formation and growth of TiC precipitates in Ti modified austenitic stainless steel (D9 alloy),[116] a primary case component material in fast breeder reactors. Figure 27 shows the variation in positron lifetime with annealing temperature for D9 alloy cold worked to 20 and 17·5% thickness reduction. This plot shows four distinct sequential stages: (1) an initial monotonic decrease in positron lifetime from the cold worked state till 823 K, which corresponds to point defect recovery; (2) a sharp increase in the interval 823–973 K, which corresponds to the formation of TiC precipitates, giving rise to positron trapping at misfit dislocations; (3) a plateau region in the interval 973–1073 K, suggesting the completion of TiC precipitation and stability of these precipitates; and (4) beyond 1073 K, a final decrease to near solution annealed state corresponding to the growth of TiC precipitates during recrystallisation. Similar PA behaviour has also been seen during isothermal annealing. In this study, the nucleation and growth of TiC precipitates have been estimated from the positron lifetime measurement.[116]

In order to study the kinetics of TiC precipitate formation, a nucleation parameter (NP) is defined as

$$NP = \{(\tau - \tau_p)/(\tau_{ppt} - \tau)\} \times 100$$

where τ_p is the positron lifetime of a defect free sample, τ is the average positron lifetime and τ_{ppt} is the saturation positron lifetime at misfit dislocations associated with TiC precipitates.[116] Figure 28 shows the variation in nucleation parameter with annealing time for three different annealing temperatures. From the nucleation parameter, it is possible to measure the percentage increase in the concentration of TiC precipitates.

Similarly, a growth parameter (GP) is defined as

$$GP = \{(\tau_{ppt} - \tau)/(\tau_{ppt} - \tau_p)\} \times 100$$

which is a measure of the percentage change in TiC precipitate concentration due to coarsening. Figure 29
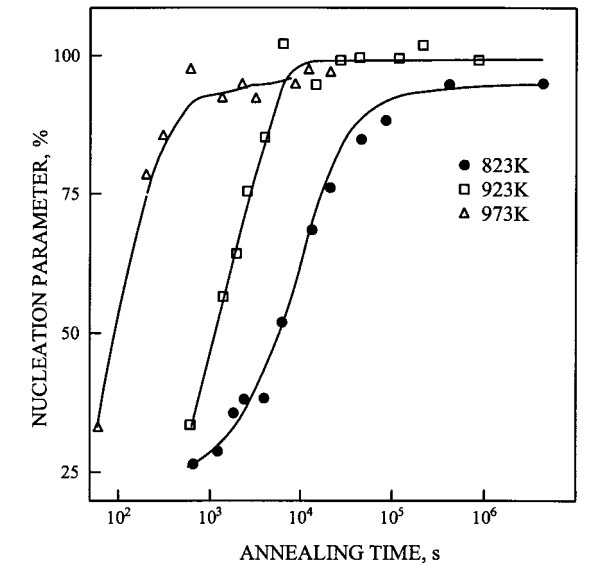
28   Variation in nucleation parameter with annealing time at three different temperatures (D9 alloy)[116]

shows the variation in growth parameter as a function of annealing time at three different temperatures. The temperature effect on both nucleation and growth of TiC precipitates can be clearly seen from Figs. 28 and 29. Since TiC precipitates are efficient traps for helium and vacancies, these studies may be significant in the context of evaluation of helium embrittlement and void swelling in these steels.

Small angle neutron scattering (SANS) for precipitation hardening studies

It has been established that the SANS intensity versus scattering vector profile is very sensitive to variations in the size and distribution of second phases. The growth of the second phase precipitates increases the intensity at lower scattering vector and reduces the intensity at higher scattering vector. This has been attributed to the diffraction scattering effect of the
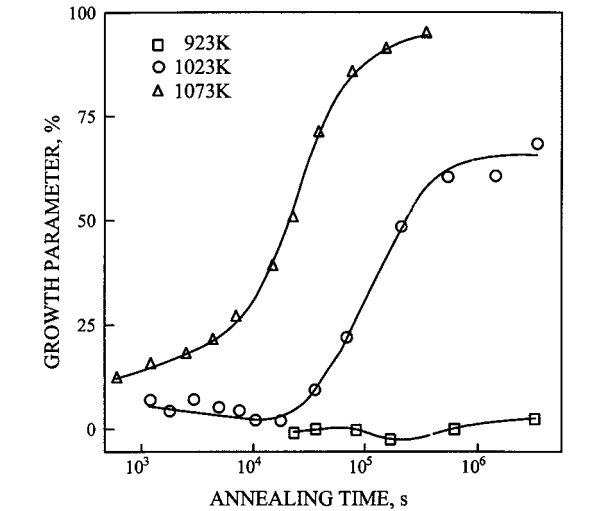
29   Variation in growth parameter with annealing time at three different temperatures (D9 alloy)[116]
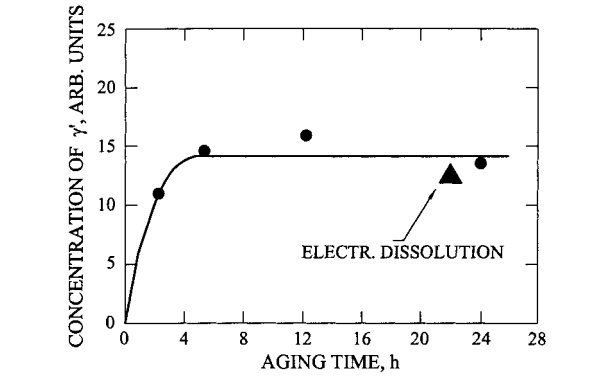
30   Variation in concentration of γ' with aging time at 1116 K for Inconel X750[119]

smaller precipitates and the multiple refraction caused by larger precipitates. Based on these phenomena, SANS has been used to study precipitation and phase transformation in Al–Mg, Al–Zn and Al–Li alloys,[117] carbon steels, austenitic stainless steels and Cu alloy.[118]

The SANS technique has been used to study the Ω phase precipitation kinetics in βIII-titanium alloy.[22] The interparticle distance D_{int} has been correlated to the peak position q_{max} of the intensity versus scattering vector q profile (*see* 'Small angle neutron scattering' section above) as

$$D_{int} = 2\pi/q_{max} \qquad \dots \dots \dots \dots \quad (17)$$

That is, the scattering intensity peak position shifts to lower q value with increase in particle size. The interparticle distance estimated from the SANS peak position has been linearly correlated to the average particle size observed from TEM.[22]

The concentration and average size of γ' precipitates in Inconel X750 during aging have also been estimated using SANS.[119] Figure 30 shows the variation in volume fraction of γ' with aging time. The volume fraction of γ' increases initially and then stabilises. The stabilisation of volume fraction of γ' is attributed to the fact that the scattering from larger particles of the fully aged sample is pushed to smaller values of scattering factor. However, the individual γ' particles continue to grow, as can be observed from Fig. 31. The evolution of particle radius with cube root of
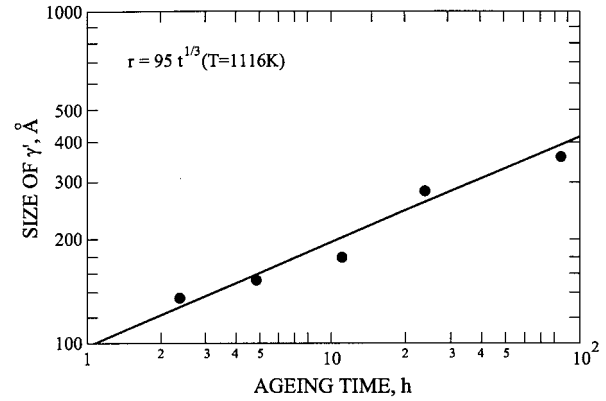
**31   Variation in average size of γ' with aging time at 1116 K for Inconel X750[119]**
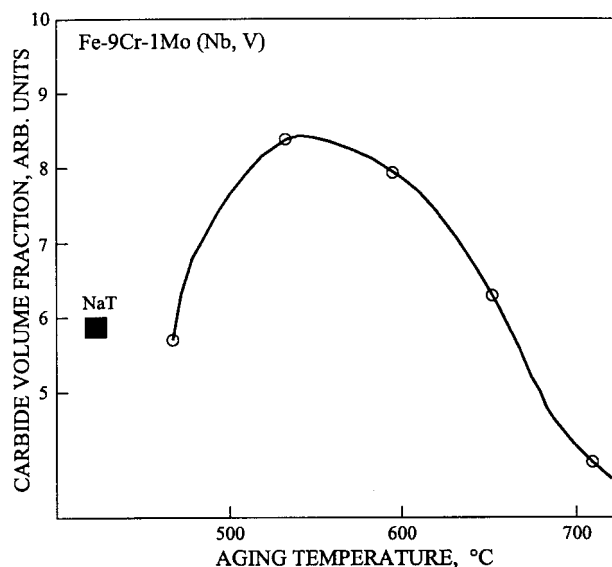
32   Carbide volume fraction as function of aging temperature for 9Cr–1Mo steel samples aged for 5000 h[121]

33   Size distribution of carbides obtained from inversion of scattering data for 9Cr–1Mo steel samples normalised and tempered (N&T) or aged for 5000 h at 538 and 704°C[121]

aging time agrees with the predictions of the Lifshitz–Wagner theory and the TEM measurements. This study shows that it is possible to estimate the growth of second phase precipitates from SANS measurement.

The SANS method has also been used to measure the thermal aging induced variation in average size of γ' precipitates from the root of the blade to the tip in aircraft turbine blades made of nickel base superalloy Inconel 700. Close agreement has been found between the SANS measurements and the TEM observations.[120] The dissolution of smaller size γ' precipitates during service has also been found from the diminution of neutron scattering at high values of scattering vector in IN100 turbine blades.[119]

Kim et al.[121] have studied the microstructural changes in modified 9Cr–1Mo ferritic steel due to aging using SANS. The scattering effect of magnetic domains (refraction) has been eliminated by magnetically saturating the specimens with externally applied magnetic field in a direction perpendicular to the neutron beam. This study clearly established the difference in the variation of scattering cross-section as a function of scattering vector between samples aged at 538 and 704°C. The lowering of scattering intensity at higher scattering vector indicates the faster growth of carbides resulting in the reduction in the number density of carbides at higher temperature. They have estimated the variation in carbide volume fraction and size distribution during isochronal annealing. Figure 32 shows the carbide volume fraction as a function of aging temperature for a 9Cr–1Mo steel. The maximum scattering cross-section is observed at 538°C at which the hardness is also found to be greatest. Figure 33 shows the size distribution of the carbides obtained from the inversion of the scattering data for a normalised and tempered sample and for samples aged for 5000 h at 538 and 704°C. The peak shift clearly shows the increase in the average precipitate size at higher aging temperature.
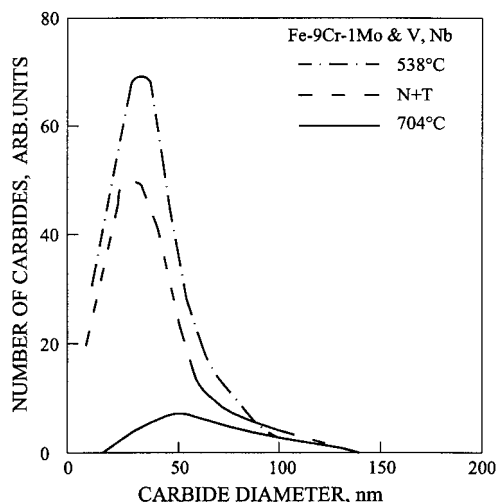
The austenite content formed during aging in 17-4PH steel has also been measured using SANS.[122] Since the austenite regions are large enough to cause multiple refraction of the neutron beam, it causes line broadening in the SANS profile. The line broadening has been found to vary in proportion to the per cent austenite content as measured using the X-ray diffraction method.

Critical assessment

Saturation magnetisation measurement can be used for absolute estimation of the volume fraction of non-ferromagnetic phase in a ferromagnetic matrix. However, this requires the application of large magnetic field strength for achieving the saturation condition, which limits the practical application of this method. The relative changes in the coercive force or MBE level even at lower applied magnetic field can also be correlated to the volume fraction of non-magnetic phases in a ferromagnetic matrix. However, this is affected by the changes in the microstructure of the ferromagnetic matrix and hence introduces error in the estimation. In steels with duplex structure containing ferrite and martensite, the volume fraction of individual phases can be obtained from the MBE profile as these two phases (one hard and one soft) act in different field ranges during magnetisation resulting in two peaks in the MBE profile.

For characterisation of thermal aging induced second phase precipitation and growth in ferritic steels, the MBE technique has potential as an NDE tool comparable to the magnetic hysteresis loop. The different stages of progressive degradation in thermally aged microstructure can be qualitatively identified from the MBE profile. Except in the short term microstructure dominated by dislocations and in the microstructure with fine (< 0·05 μm) coherent precipitates, the individual variation in precipitation and growth of second phase particles can be resolved and the average size of precipitates can be quantified from the MBE peak position in sufficiently aged microstructures.

Ultrasonic attenuation and velocity measurements show great promise for characterisation of second phase precipitation in metallic alloys. It is possible to identify the development of coherency and loss of coherency during precipitation from changes in the attenuation and velocity, as they strongly influence the ultrasonic scattering and elastic modulus. However, quantification of second phase particles from ultrasonic parameters has not been well established. Since the mechanisms of interaction of ultrasonic waves with microstructural features are strongly influenced by the frequency range of the ultrasonic waves and the size of the precipitates, the relationship between the ultrasonic parameters and the size or volume fraction of second phase particles is different for different materials. Further research work is required for understanding the mechanism of interaction of ultrasonic waves with different microstructural features.

The analysis of XRD profiles is another NDE tool for identifying the formation of coherent precipitates and loss of coherency during coarsening. Since the precipitation of fine second phase particles is always associated with coherency strain, the precipitation kinetics can be observed from the changes in the peak position and FWHM of the XRD profile. However, the quantification of second phase particles is yet to be carried out. However, this technique is restricted because it requires an electropolished surface and hence it is time consuming.

Positron annihilation measurement is another potential NDE method for studying precipitation behaviour. The sensitivity of the positron lifetime to the dislocations can be exploited for detecting the nucleation and growth of fine precipitates as they are accompanied by changes in the misfit dislocation density. Also, since the PA lifetime is a characteristic of the composition of second phases, the transformation of phases can be detected from changes in the PA lifetime. This technique can be effectively utilised for evaluating the precipitation condition in precipitation hardened alloys. Also, the PA technique can be used for estimating the concentration of fine precipitates, which would otherwise be possible only by TEM.

The neutron scattering properties are strongly influenced by the size and volume fraction of second phase particles. Exploiting this, SANS measurement can be used to obtain information on the precipitation and growth of second phases and quantitative estimation of average size and volume fraction of second phases. The cost and size of a neutron source facility are the main limitations for wide application of this technique.

Characterisation of tensile properties and fracture toughness using NDE techniques

Many NDE techniques have been developed to evaluate properties such as hardness, elastic modulus, tensile strength and fracture toughness. Some of the NDE techniques are also capable of identifying the deformation and fracture mechanisms.
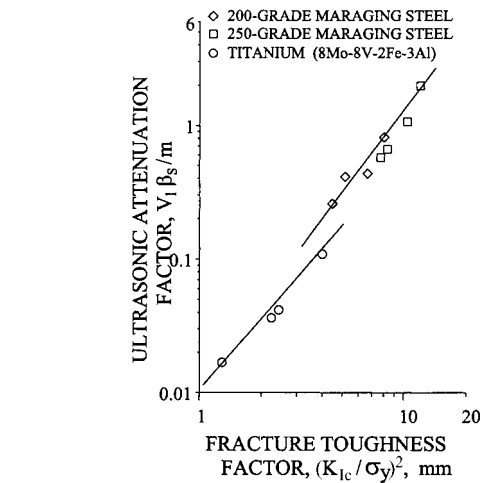
34   Relationship between ultrasonic attenuation factor and fracture toughness factor for three different alloys[14]

Determination of elastic modulus, yield strength, ultimate tensile strength, fracture toughness and hardness

Ultrasonic methods

An excellent review has been carried out by Vary[14] on the evaluation of mechanical properties from ultrasonic attenuation and velocity measurements. Good correlations between the principal ultrasonic wave velocities and the elastic constants were established.[14] As shown above, for engineering materials, the relation between total attenuation α and frequency f will involve a combination of exponents on f and mean grain size d. A particular derivative β_d relative to the variation in α versus f is given by

$$\beta_d = d\alpha/df|_d \text{ where } \alpha = cf^m + \dots \quad \dots \quad (18)$$

For many materials, c and m are constants over a frequency range in which a specific attenuation mechanism predominates depending on the mean grain size d. Within this frequency range, the quantity β_d will correlate with microstructure dependent material properties.[123] Based on this, the feasibility of ultrasonic measurement of plane strain fracture toughness K_{Ic} has been demonstrated in maraging steels and titanium alloy.[123] The fracture toughness factor $(K_{Ic}/\sigma_y)^2$ has been correlated to the ultrasonic parameter as

$$(K_{Ic}/\sigma_y)^2 = M(V_l\beta_d/m)^{1/2} \quad \dots \quad (19)$$

where V_l is the longitudinal velocity and β_d is the attenuation slope $(d\alpha/df)$ evaluated at a particular frequency that is based on the mean grain size d and M is an experimental constant for a specific material. Figure 34 shows linear relationship between the ultrasonic attenuation factor and the fracture toughness factor for three different alloys.[14]

Similarly, the yield strength σ_y has been related to the ultrasonic parameter as

$$\sigma_y = (A/B)(K_{Ic}) + \beta_1 \quad \dots \quad (20)$$

where β_1 is the attenuation slope $(d\alpha/df)$ evaluated at a particular frequency for unit attenuation coefficient, and A and B are experimental constants
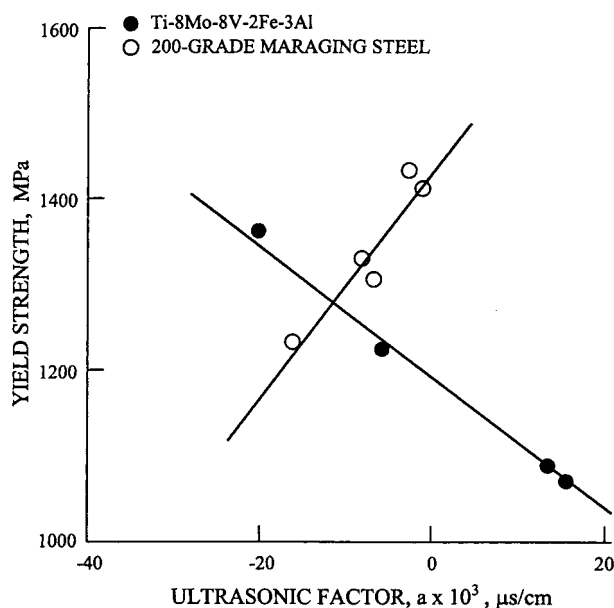
35 Relationship between yield strength and ultrasonic parameter for maraging steel and Ti–Al alloy[123]

for a specific material. Figure 35 shows the typical linear relationship between yield strength and ultrasonic parameter for Ti–Al alloy and maraging steel.[123] These studies show that, once the calibration curves have been established for a given polycrystalline material, the ultrasonic methods can be used to determine the fracture toughness and yield strength.

Ultrasonic spectral parameters, such as peak frequency and FWHM, can be used to estimate the yield strength indirectly from the grain size, as mentioned above. However, this is possible only if there are no other substructural changes accompanying the grain size variation.[63] Ultrasonic velocity and attenuation have been correlated to hardness in various steels. In general, the velocity and attenuation coefficients have been found to vary inversely with hardness in case hardened, quenched and tempered steels.[124,125]

Magnetic methods
Magnetic hysteresis loop
As mentioned in the section 'Micromagnetic NDE techniques' above, the magnetic hysteresis loop parameters are sensitive to microstructure dependent properties: many studies have established the correlation between magnetic parameters (such as coercive force and residual induction) and mechanical properties (such as hardness and tensile strength) in various ferritic steels.[82,126–133] The quality of various heat treatments is assessed primarily based on the hardness value. This is because of the general observation that hardness is strongly influenced by basic microstructure, alloy content (particularly carbon level in steels), presence of secondary phases, internal stresses, etc. Hardness has been related to strength and ductility in most materials. Generally, hard martensitic structure was found to have high coercivity due to the presence of high residual microstrain and due to the high shape anisotropy of crystallites.[131] The mag-

netic properties of bainite were found to be intermediate between the high permeability ferrite/pearlite (soft) structure and low permeability martensite.[131] Gorkunov *et al.*[132] have used H_c for evaluation of the hardness of various steels. Generally, it has been observed that H_c increases linearly with hardness in Fe–C alloy up to 0.5 wt-%C. At higher percentages of carbon, the increase in H_c is very slow.[132]

These studies show that the relationship between the magnetic hysteresis loop parameters and mechanical properties is unique to a specific class of steels depending on the amount of carbon and other alloying elements. Based on the characteristic variations in the magnetic hysteresis loop parameters with tempering temperature, the structural steels were classified into four groups: steels with (i) < 0.3 wt-%C, (ii) 0.3–0.4 wt-%C, (iii) > 0.4 wt-%C, and (iv) large content of alloying elements. From these relationships, mechanical properties such as hardness, yield strength, ultimate tensile strength, ductility and impact strength can be estimated.[126]

Magnetic Barkhausen emission (MBE)
In general, similar to H_c, the MBE parameters have been related to the hardness of steels with different microstructures. Tiitto[9] related the *M* parameter (derived from the pulse height distribution) with hardness value for ferritic, pearlitic and martensitic steels. The *M* parameter was found to decrease linearly with increase in hardness, independent of the type of structure present. It has also been found that the *M* parameter obtained from different regions (negative high field, near zero field, positive high field) of the hysteresis loop shows different behaviour which is specific to the treatment, e.g. cold rolling, recrystallisation, tempering, etc.[9] It is quite difficult to judge the appropriate region of pulse height analysis for correct estimation. A similar type of linear relationship has also been found between hardness and rms voltage peak of the MBE in simulated heat affected zone (HAZ) microstructures of weldments of Cr–Mo steels.[134] But in the case of tempered microstructures, the linear correlation between hardness and the rms voltage peak height of the MBE exists only in short term tempered conditions. In long term aged conditions, the correlation becomes non-linear due to the synergistic effect of variations in grain size and precipitate size.[98]

The *M* parameter has also been correlated with tensile strength and elongation in carbon steels.[10,135] It has been found that the *M* parameter decreases linearly with increase in tensile strength and increases linearly with elongation. In the authors' laboratory, the rms voltage peak of the MBE profile has also been correlated to tensile strength in simulated HAZ microstructures of weldments of Cr–Mo steels (Fig. 36) and short term thermally aged microstructures in 17-4PH steel (Fig. 37) and to impact toughness in aged 17-4PH steel (Fig. 38). In Cr–Mo steels, the MBE decreases with increase in tensile strength, but the reverse is observed for 17-4PH steel. This is because, in Cr–Mo steel, dissolution of bainite or martensite is accompanied by coarsening of ferrite laths/grains. This would lead to reduction in tensile strength, but would enhance domain wall displace-
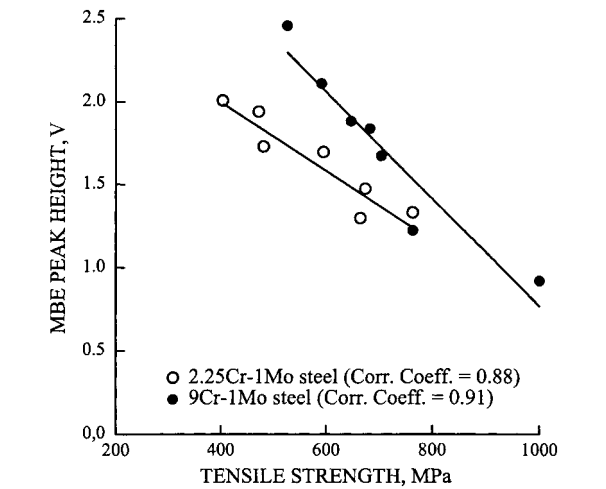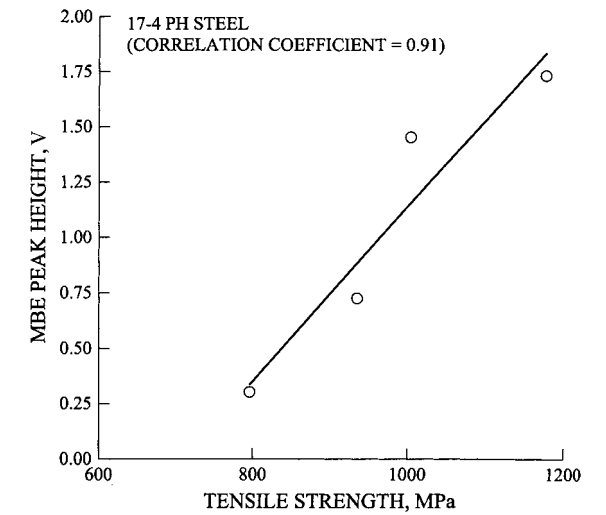
36   Relationship between MBE peak height and tensile strength in thermally aged and simulated HAZ microstructures of 2·25Cr–1Mo and 9Cr–1Mo steels

38   Relationship between MBE peak height and Charpy impact energy in thermally aged 17-4PH steel
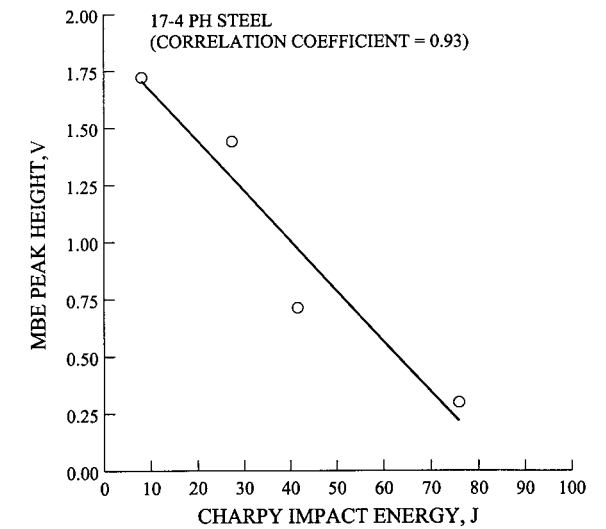
ment and hence the MBE. In the case of 17-4PH steel, the thermal aging results in austenite reversion in the copper rich precipitate regions. The austenite formation would reduce the tensile strength, but strongly inhibits the domain alignment process and hence reduces the MBE. At the same time, the formation of austenite increases the impact toughness. This effect can be observed from Fig. 38. These studies clearly show that the MBE behaviour is strongly influenced by the type of microstructural evolution and its effect on the magnetisation process.

Acoustic emission (AE)

Since the AE signal is strongly influenced by the deformation mechanism, that is, the extent of ductility or brittleness, the fracture process can be characterised from the characteristics of the AE signal. Palmer[136] has carried out AE measurements during fracture toughness tests of reactor pressure vessel steel. He observed that the total AE count increases rapidly up to the maximum load and then saturates

(Fig. 39). It has been observed that most of the emissions arise from plastic zone expansion and the emissions from ductile crack growth are relatively quiet. He also observed that the AE behaviour is structure sensitive, and is markedly affected by the prestrain. Dunegan *et al.*[137] showed that the total AE count N is proportional to the volume of the plastic zone ahead of a crack tip which is a function of stress intensity factor K and, hence, $N \propto K^n$ where the exponent varies from 4 to 8 for different materials.

Takahashi *et al.*[138] have monitored AE during fracture toughness tests for AISI 4340 and SA533B steels. They have related accumulated AE energy and the value of the J integral, which has been used for identifying crack initiation. A clear indication of the onset of stable crack extension J_{Ic} is provided by a significant change in slope of the curve of accumulated AE energy versus J integral (Fig. 40). This study shows that it is possible to determine the J_{Ic} fracture criterion using the AE technique. They have also shown a linear relationship between the area of pop-in crack or incremental crack growth and accumulated AE energy for these steels in different tempered conditions.

37   Relationship between MBE peak height and tensile strength in thermally aged 17-4PH steel
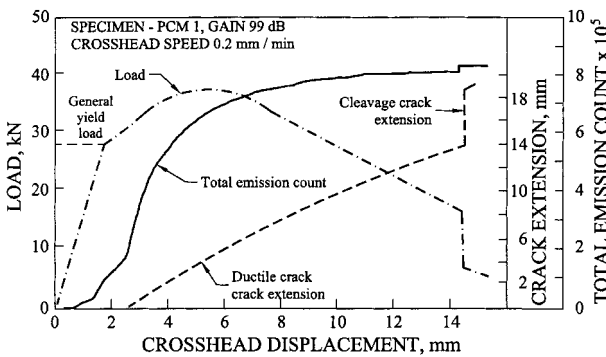
39   Variation in total AE counts, load, crack extension as function of crosshead displacement during fracture toughness test of reactor pressure vessel steel[136]
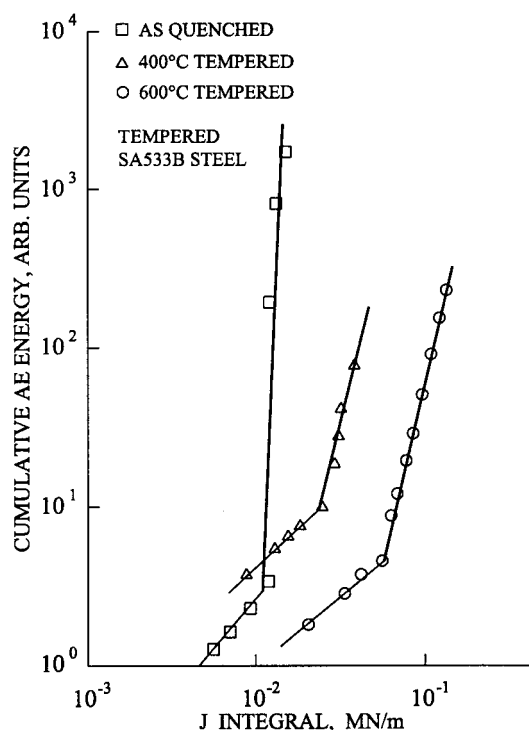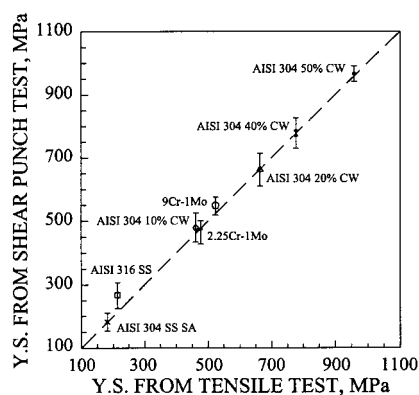
40 **Variation in accumulated AE energy versus *J* integral value for differently tempered SA533B steel**[138]

42 **Comparison between true stress–true strain relationship obtained from automated ball indentation (ABI) and tensile tests on CF8 stainless steel**[144]
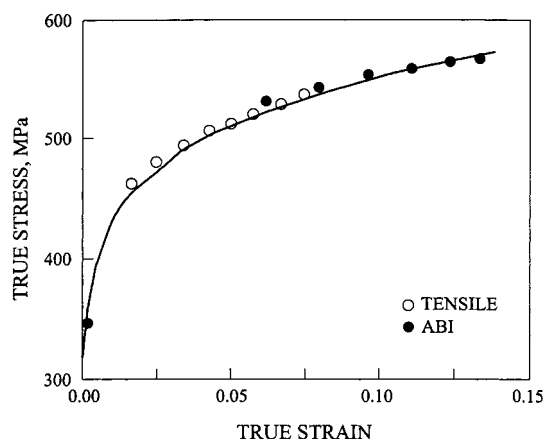
Miniature specimen testing

Many studies have been carried out to determine mechanical properties using miniature specimen testing techniques from samples scooped out directly from service exposed components/structures. For example, uniaxial tensile properties and fracture toughness have been determined from the shear punch test,[139,140] ductility from the disc bend test,[141] and ductile to brittle transition temperature from the small punch test.[142] Miniature specimen testing is gaining importance, because it gives the absolute value of the mechanical properties of the actual components.

A recent study shows excellent correlation between the yield strength and ultimate tensile strength values predicted from the shear punch test and those determined f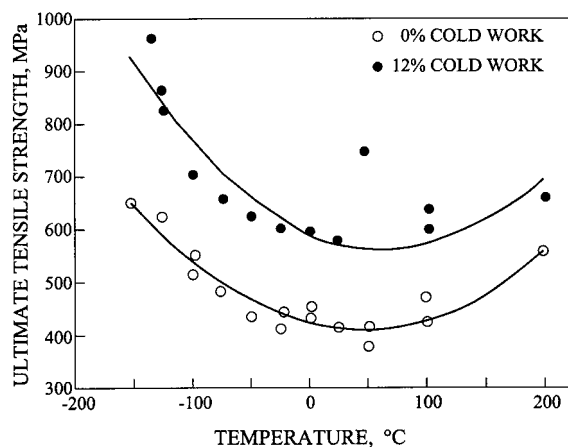rom the standard tensile test for various ferritic and austenitic steels.[140] Figure 41 shows a typical comparison between the yield strength obtained from the shear punch test and from the tensile test for different steels. Monitoring of the AE signal during miniature disc bend and shear punch tests also clearly indicated the macroyielding by a sudden rise in the AE level.[143] The AE technique can also be used in conjunction with miniature tests for reliable prediction of yield strength. Similarly, the automated ball indentation (ABI) technique shows great promise for determination of tensile properties and fracture toughness based on the indentation depth and diameter.[144] A recent study shows excellent matching between the true stress–true strain relationship obtained from ABI and tensile tests (Fig. 42). It has been established that the temperature dependence of ultimate tensile strength and fracture toughness determined using the ABI method matches exactly with that obtained from conventional large size specimen testing. Figure 43 shows the typical effect of cold work on the temperature dependence of ultimate tensile strength estimated using the ABI method in AISI type A36 steel.[144]

SA = solution annealed; CW = cold worked

41 **Typical comparison between yield strength obtained from shear punch test and tensile test for different steels**[140]

43 **Effect of cold work on temperature dependence of ultimate tensile strength estimated using ABI method in AISI type A36 steel**[144]

The small punch test has been used to determine the fracture toughness and ductile to brittle transition temperature (DBTT) of steels.[145] It has been generally observed that the DBTT obtained from small punch tests based on graphically extrapolated data to 0·5 J shows lower values (typically about $-200°C$) compared to those from Charpy tests. However, linear correlation has been found between DBTT values obtained from the small punch test and the Charpy test. Similarly, correlation has been established between the fracture toughness obtained from the small punch test and the full size J test.[145] Bulloch[146] has carried out a complete analysis of various results available in the literature on the temperature dependence of fracture toughness obtained from small punch tests and compared this with that obtained from large size Charpy tests. He has shown that the ductile to brittle transition temperature obtained from small punch tests T_{sp} and from Charpy tests (fracture appearance transition temperature, FATT) can be well related over a wide temperature range by a non-linear relationship as

$$FATT = C/T_{sp}^2$$

where C is a scaling constant. However, it has been found that the grain size[147] and the strain rate influence this relationship.[148,149]

These recent studies establish the potential of miniature specimen testing for the determination of mechanical properties, but suggest the requirement for an appropriate standard or guidelines on test procedures to be adopted. Also, the large scatter in the data limits the confidence level.

Characterisation of different stages of tensile deformation and fracture

Magnetic Barkhausen emission method

Karjalainen and co-workers[150,151] have studied the effect of unidirectional tensile straining on MBE in a mild steel. They have measured the true rms value of the MBE signal during magnetisation both parallel B_p and transverse B_t to the stress direction after unloading the sample from different load levels. They observed considerable reduction in B_p at the macroscopic yield stress while a slight decrease was seen below the yield stress. The decrease in B_p and the increase in B_t have been attributed to the presence of residual compressive stress in the direction of the tensile axis in the surface layer of the strained and unloaded specimen.

Recently, Moorthy and co-workers[152,153] have shown that the four different stages of tensile deformation, namely, (1) perfectly elastic, (2) plastic microyielding, (3) macroyielding, and (4) progressive plastic deformation, can be identified from MBE measurements. Figure 44 shows the effect of different stages of prior tensile deformation on the MBE profile in tempered 2·25Cr–1Mo steel.

It can be observed that the MBE profile remains more or less the same up to a certain stress level. Then, with the increase in prior applied stress level, both MBE peak 1 and peak 2 height values decrease. On further increase in prior stress level, the initially present two peaks in the MBE profiles merge into a
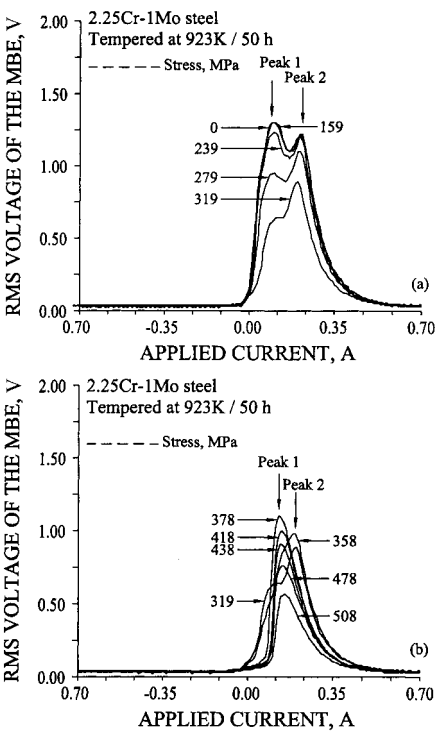

44   Variation in rms voltage of MBE as function of current applied to electromagnetic yoke for different stress (MPa) levels (arrowed to curves) in 2·25Cr–1Mo steel samples tempered at 923 K for 50 h[152]

single peak in between the originally present two peaks. Beyond macroyielding, the single central MBE peak decreases gradually with increasing prior tensile stress level. Similar changes in MBE profiles have also been observed in tempered 0·2%C steel samples.[152] Figures 45 and 46 show the variation in the MBE peak height and the prior stress level as a function of strain in tempered 2·25Cr–1Mo steel and in HSLA steel weldments respectively. The different stages of progressive tensile deformation are clearly illustrated by these figures.

Stage 1: perfectly elastic region   It can be observed from Fig. 44a that, during the initial stages of elastic loading, the MBE profiles remain comparable to that of the virgin condition. This indicates the fact that there is no significant change in the microstructure (dislocation density) after unloading from these stress levels. The constant values of MBE peak 1 height in the unloaded condition (stage 1 in Figs. 45 and 46) confirm stage 1 to be the perfectly elastic condition.

Stage 2: microyielding   It can be seen from Fig. 44 that the MBE peak 1 and peak 2 heights decrease significantly well before the macroyielding. This indicates the activation of grain boundary and Frank–Read type dislocation sources even during the macroelastic region (about 3/4 of the yield stress) causing the plastic microyielding. The dislocation pile-ups created within the grain would reduce the mean free path of domain wall displacement and hence the MBE peak heights.

Stage 3: macroyielding   Near the macroyielding, the originally present two MBE peaks merge into a single central peak with relatively high peak height and
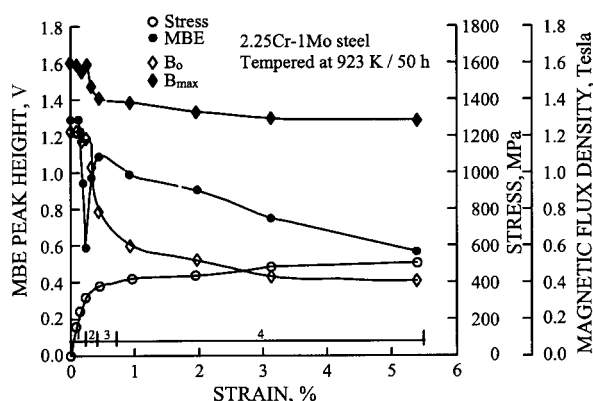
45 Variation in MBE peak height (peak 1 height in regions 1 and 2 and central peak height in regions 3 and 4), induction at zero B_o and at maximum B_{max} applied magnetic field, and applied stress as function of percentage strain for 2·25Cr–1Mo steel samples tempered at 923 K for 50 h[152]

46 Typical variation in MBE level in loaded and unloaded conditions and applied stress as function of percentage nominal strain at weld, heat affected zone (HAZ) and base metal regions of HSLA steel weldment specimen[153]

narrow profile width. It is known that the macroyielding is associated with grain rotation in order to maintain the boundary integrity between adjacent grains for compatible deformation. When such grain rotation occurs under the action of external tensile stress, the grain reorientation would be such that the $\langle 100 \rangle$ direction in some grains would tend to align closer to the stress direction in order to reduce its magneto-static energy by way of decreasing the normal component of magnetisation across the grain boundary. This results in domain alignment closer to the tensile stress direction and would enhance domain wall movement during magnetisation along the stress direction and hence the increase in the micromagnetic parameters.

Stage 4: progressive plastic deformation Entry into the plastic deformation regime is clearly reflected by a gradual decrease in MBE peak height. The dislocations generated due to plastic deformation act as strong obstacles to domain wall movement. Plastic deformation is associated with the formation of extensive dislocation tangles, which would reduce the mean free path of the domain wall displacement. The linear reduction in the MBE peak with strain is attributed to the increase in the dislocation density and the compressive residual stress produced on the surface due to the prior tensile deformation.

Assessment of tensile deformation and fracture mechanisms

Acoustic emission (AE) technique
Plastic deformation and fracture processes are strongly influenced by the microstructural condition of the material. Hence, it can be expected that the elastic stress waves generated during different deformation and fracture mechanisms would have characteristic features. Therefore, analysis of the AE signal would give an insight into the different types and stages of deformation and fracture processes. An excellent review of AE generated by various plastic deformation mechanisms in different materials has been compiled by Heiple and Carpenter[154,155] The
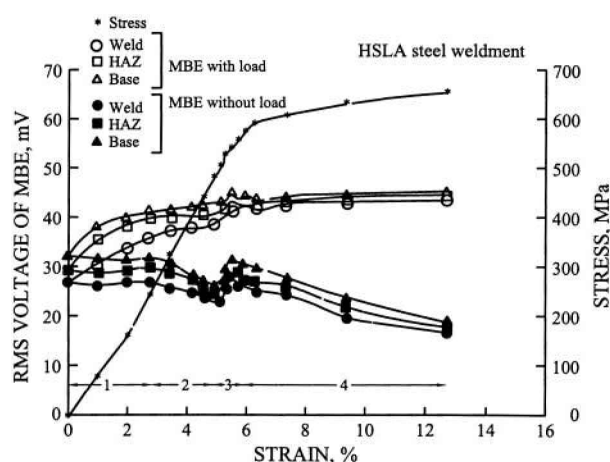
influence of various microstructural features (such as grain size, inclusions, carburisation, inter- and intra-granular precipitates) and test parameters (such as strain rate and temperature) on AE generated during tensile deformation has been studied.[156–159] Various processes such as: (i) reduction in dislocation activity due to intragranular precipitation of carbides in short term thermally aged specimens, (ii) grain boundary carbide cracking in the presence of intergranular carbides in long term thermally aged specimens, (iii) cracking of the brittle case in carburised steel, and (iv) decohesion and fracture of inclusions, have been identified from AE parameters such as events, ring-down count (RDC) rate, energy and peak amplitude distribution.

The deformation associated with decohesion and fracture of inclusions can be revealed by the AE signals.[159–162] Figure 47 shows the difference in the peak amplitude distribution plot between commercial grade and nuclear grade austenitic stainless steels. The large number of low peak amplitude AE generated in the low inclusion content nuclear grade steel is attributed to the dominance of deformation by dislocation generation and motion. The relatively large value of high peak amplitude AE in the commercial grade steel is attributed to decohesion and fracture of inclusions. Similarly, carburisation results in a larger number of AE events with higher peak amplitude as compared to solution annealed steel.[162]

Acoustic emission during discontinuous deformation
The AE technique has been applied to study the discontinuous deformation in the yield region in many materials. In most of the studies, the AE generated during load drop in the yield region is attributed to breakaway of dislocations from solute pinning atmospheres.
*Steels* A study by Airoldi[163] using A533B steel at room temperature showed very little AE associated with yield point load drop. This is attributed to reduction in the dislocation glide distance and dislocation velocity, which play important roles, in addition to the number of dislocations participating
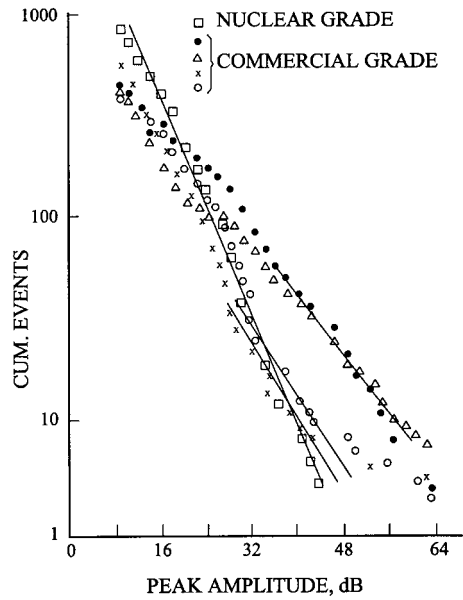
47 **AE peak amplitude distribution plots for commercial grade and nuclear grade AISI type 316 austenitic stainless steels**[162]

in *a*, type A and type B serrations are indicated; in *c*, E and F denote one-to-one correlation with 'burst' AE signals

48 **AE rms voltage peak in correlation with change in load during serrated flow in AISI type 316 stainless steel at different temperatures**[156]

in the load drop phenomenon. Tandon and Tangin[164] observed in Fe–3Si steel, a sharp peak in AE count rate at yield point load drop (formation of Lüders band) and constant AE activity during Lüders band propagation. They suggested that the cluster of yielded grains at the end of the microyield region may expand at a faster rate resulting in the nucleation of a band which rapidly crosses the width of the specimen. The expansion of the nucleated band from grain to grain occurs by extensive grain boundary dislocation source activation, which results in high AE activity. The Lüders band front is the region of intense slip activity. Since the basic process of AE here is same as that at yield, the AE pulses have been found to have the same amplitude. Long and Yin Huazi[165] studied the AE during deformation of dual phase steels consisting of ferrite and martensite. The total AE energy $\sum E_{Lp}$ emitted during Lüders band propagation is related to the Lüders strain ε_L: $\sum E_{Lp}/\varepsilon_L$ decreases as ε increases because of the increase in ε resulting from the decrease in dislocation velocity.

Aluminium alloys   Caceres[166] studied the AE generation associated with Lüders bands and Portevin–Le Chatelier (PLC) bands in Al–2.5Mg alloy. He observed that the cumulative AE activity during Lüders deformation increases with increasing strain rate while Lüders bands become shorter and are increasingly serrated in Al–2.5Mg alloy. Once PLC bands develop, AE appears in stepwise fashion. The AE is found to concentrate mainly at the beginning of every new band, but preceding the first load drop. Once nucleated, the PLC band propagates with relatively low AE. Increase in AE is related to serration amplitude of PLC bands. The results of TEM and *in situ* HVTEM showed that AE is associated with dislocation movement and dislocation breeding in localised slip bands.
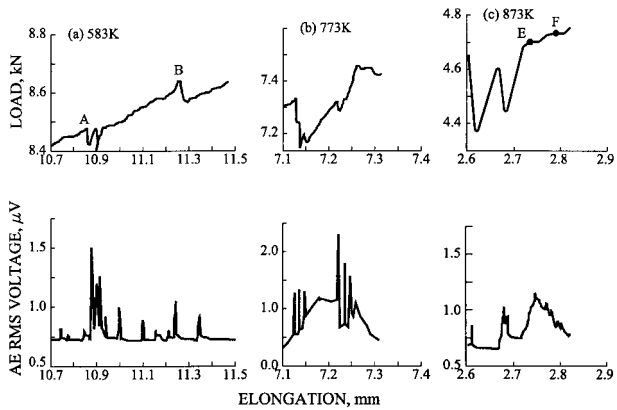
Acoustic emission during dynamic strain aging/PLC serrated flow
Characteristic AE has been observed with the occurrence of different types of serration in various materials. In most of the studies, the AE generation is attributed to repeated locking and unlocking of dislocations by solute atoms during deformation. In addition to the number of dislocations participating in an event, the glide distance and velocity of dislocations are found to influence the amount of AE activity corresponding to a load drop.

Steels   Fleischmann[167] studied AE behaviour in mild steel using a 2.1 MHz resonant sensor. He observed one AE peak at the start of yield and another peak at the end of serration or at the beginning of the consolidation stage. The frequency spectra of the AE signals from both peaks were corrected for transfer function of transducer and specimen. The signal from the first peak showed a predominant peak at low frequencies (< 500 kHz) and a small peak at 3 MHz. The signals corresponding to the second peak were found to have low amplitude at low frequency and a predominant peak at 3 MHz. It was also concluded that the AE spectrum depends strongly on the frequency characteristics of both the transducer and the specimen.

Raj[156] found generation of AE during both the load drop and load rise corresponding to each serration for different types of serration in AISI type 316 stainless steel (Fig. 48). It was also found that the rate of load drop or rise decides the intensity of the AE generation. Good correlations were obtained between load drop or rise and rms voltage of AE. Comparative studies on AE generated during Lüders deformation in mild steel and the PLC effect in austenitic stainless steels have been carried out by Raj *et al.*[168] by conducting high temperature (548–873 K) tensile tests. A one-to-one correlation has been obtained between the serrations in load–elongation plots and AE signals (burst type) (Fig. 48). It is observed from these studies that the AE technique can be used to identify the critical strain for the occurrence of the PLC effect at a given temperature more precisely than the stress–strain plot.
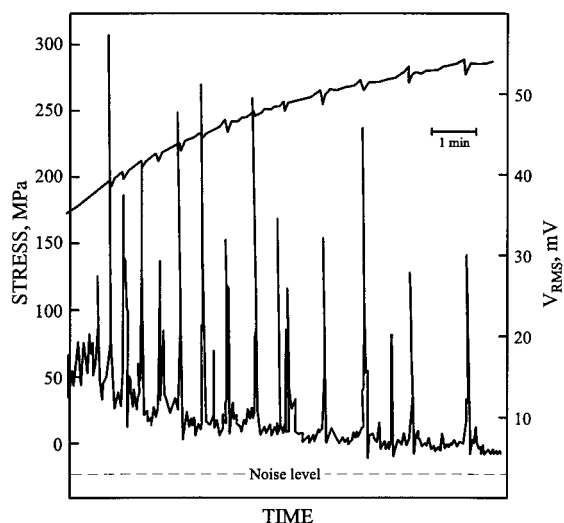
49 AE rms voltage and stress versus time plot for 5083-O Al alloy corresponding to type A serrations during tensile deformation[155]

Aluminium alloys A study by Pascual[169] using 2024 Al alloy showed a rise in AE activity just before the occurrence of type A serrations and during type B serrations. The increase in AE is attributed to mobile dislocation breeding. With increase in strain rate, AE per unit strain was found to decrease and was attributed to a decrease in the dynamic strain aging effect. Heiple and Carpenter[155] observed AE during type A PLC yielding in 5083 Al alloy. The rms voltage of AE versus time plot showed a sharp peak at each load drop (Fig. 49). It was also observed that as the percentage strain increases, the AE peak height decreases even though the load drop is high. Heiple[170] observed, in 5083 Al alloy, a very high level of AE at low strain rates and negative strain rate sensitivity for AE. At high strain rates, he observed that the rms voltage of AE is proportional to the square root of the strain rate.

Scruby[171] observed an AE pulse corresponding to each load drop during type A serrations in Al–1·3Mg alloy, using a sensor having 0·1–1 MHz bandwidth. During PLC deformation, the influence of grain size was observed. For the grain size range 25–80 μm, AE pulse height increased with grain size and was attributed to the increase in the mean free path of the dislocation movement with grain size. For grain size greater than 100 μm, AE pulse height decreased. This was attributed to the rapid reduction in the number of dislocations that can break free of solute due to reduction in flow stress with increase in grain size. This was supported by the observation that the serrated yielding of the PLC effect disappears simultaneously with increase in grain size.

Scruby *et al.*[172] observed copious AE during serrated yielding in Al–5·5Zn–2·5Mg–1·6Cu alloy under solution treated, quenched and room temperature aged conditions. With the addition of 0·16%Zr, the AE associated with serrated yielding reduced substantially under the same heat treatment conditions. Zirconium forms small, insoluble precipitates that pin grain boundaries during solution treatment and reduce grain growth. The smaller grain size or poss-

ibly Zr precipitates reduce the glide distance of dislocation avalanches thus reducing the AE activity.

Young *et al.*[173] observed the effect of addition of Si to Al in Al–Si alloy. With heat treatment, Si precipitates are formed and grow and become more widely spaced. Serrated yielding was observed for all precipitate distributions, but the level of AE associated with serrations was found to increase as the precipitates became larger and widely spaced. The influence of glide distance is found to be important during serrated flow. Caceres[174] observed, in Al and Cu alloys, that band nucleation generates a high level of AE, whereas band propagation is associated with a low level of AE. *Alpha brass* Hartman[175] studied AE behaviour in α-brass. In his study, the AE energy released during dead weight load tests at room temperature is correlated with stored elastic energy between strain increments. Takagaki and Mukherjee[176] attributed AE during serrated flow of α-brass to sudden dislocation motion from unpinning and multiplication. As with yield point load drops, the presence of serrations does not ensure a high level of AE, nor is the level of AE necessarily correlated with the serration size.

The results from the various studies referred to above indicate that the AE signals have so far been used to make essentially qualitative interpretations. For the AE studies to be undertaken to achieve better insight into dynamic strain aging, it is preferable to select the material, microstructure and test conditions such that the phenomenon occurs at room temperature. This would enable direct placement of the broadband sensor on the specimen and recording of signals with minimum modification.

Acoustic emission during deformation of precipitation strengthened materials

It is well known that various types of deformation processes such as dislocation generation and motion by Frank–Read and grain boundary sources in a precipitate free single phase material, particle shearing and Orowan looping processes in two phase material with uniformly distributed fine precipitates, and decohesion and fracture of incoherent, coarse and brittle precipitates in a two phase material take place under loaded conditions. Sometimes, more than one deformation process may operate simultaneously in the presence of more than two types of phase. Conventional techniques such as optical and electron-optical systems may reveal the presence of composite deformation behaviour, but it may not be possible to assess the predominant mechanism responsible and the quantitative contribution from each process at each stage. The only possible technique that could give such information is the AE technique, because of its dynamic nature and its behaviour being a strong function of the deformation process. This possibility has been demonstrated by carrying out AE studies in an elegant way to identify and distinguish dynamic events, such as decohesion and fracture of carbides, and deformation processes, including particle shearing and Orowan looping, in a model alloy, i.e. nickel based superalloy Nimonic PE16.[177,178] Microstructural details and operating deformation processes for selected specimens (designated N1–N5) are given in Table 2.

Table 2   Microstructural details and operating deformation processes for specimens N1–N5 of nickel based superalloy Nimonic PE16[177] (*see* Fig. 50 for heat treatments)

Deformation processes

N1/γ
Dislocation multiplication by Frank–Read and grain boundary sources

N2/γ + MC
(i)   Dislocation activity at γ/carbide interface
(ii)   Decohesion and fracture of MC

N3/γ + γ'
Particle shearing process (size of $\gamma' = 9$ nm)

N4/γ + γ'
Orowan looping processes (size of $\gamma' = 20$ nm)

N5/γ + γ' + MC
All above processes, low volume fraction of γ' (size of $\gamma' = 10$ nm)

Figure 50 shows the AE behaviour during tensile deformation in the specimens N1–N5 having different microstructures resulting from solution annealing (N1) and various solution annealing + aging (N2–N5) treatments. Burst type AE is generated in N2 specimens throughout the tensile test. Only occasional bursts were generated in solution annealed (N1) specimens. Burst emission generated during plastic deformation at higher strains in N2 specimens as compared to solution annealed specimens is attributed to events generated by decohesion and fracture of MC type carbides.[178] In the presence of coherent γ' precipitates, there is a large increase in acoustic activity manifested by very high rms voltage peaks in the yield region in N3 specimens which is attributed to deformation taking place by particle shearing processes. However, when the process of deformation changes from particle shearing to predominantly Orowan looping, as in the case of N4 specimens, there is a considerable reduction in the number of AE events and complete absence of any AE rms voltage peak in the yield region. The broadness of the rms voltage peak during the yielding stage in N3 specimens is attributed to progressive yielding taking place in the complete volume of the specimen. The yielding starts on a microscopic scale initially at favourable regions and progresses throughout the gauge volume as the load increases. The favourable regions for early yielding are the grains that are favourably oriented with respect to the tensile axis and microscopic regions with finer size of γ'. As γ' size approaches the optimum size of 10 nm, AE events with relatively higher peak amplitude are generated. This also results in the increase in the rms value of the signal.

The generation of higher events and ringdown counts in N5 specimens compared to in N3 specimens is due to the contribution from decohesion and fracture of MC present in N5 specimens in addition to the contribution from particle shearing. It was observed that characteristic AE signatures observed in specimens containing γ' (N3) and MC (N2) individually have been maintained even when the two phases are present conjointly in the microstructure (N5). This study clearly reveals the generation of characteristic

A - CHANGE IN X-AXIS SCALE   B - YIELD STRESS
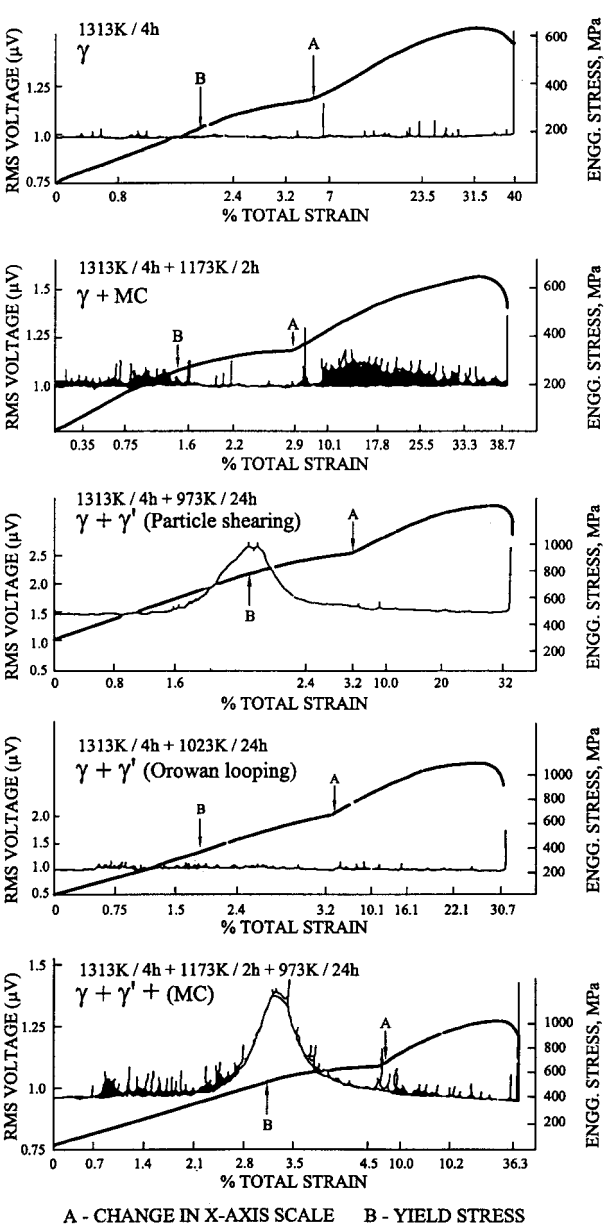
50   Variation in AE rms voltage and engineering stress with percentage total strain for Nimonic PE16 superalloy specimens having different microstructures resulting from solution treatment (N1) and various solution treatment + aging (N2–N5) treatments[178]

AE for different deformation mechanisms. That of the authors' is the only study in the open literature where a detailed analysis on the AE behaviour and a dynamic insight into the deformation process could be observed.

Frequency spectrum of acoustic emission generated during deformation
It is expected that the frequency spectrum of the AE signals generated by the different plastic deformation mechanisms would be different, because the parameters such as dislocation velocity, number of dislocations generated from a source and moving in a coherent manner, waiting time of dislocations in a pile-up, etc. would contribute to the frequency spectrum of the AE signals. A study[179] made using austen-

itic stainless steel shows that the predominant frequency of AE signals increases linearly with increase in plastic strain up to necking. It has been observed from this study that selection of different resonant frequency sensors is essential to detect the AE signal with maximum sensitivity at different strain levels during tensile deformation. An attempt has been made to develop a theoretical model to predict the approximate frequency range of the AE signal generated from dislocation sources operating during pre-yield and near-yield tensile deformation.[180] The frequency of the AE signal has been calculated from the event lifetime of Frank–Read and grain boundary source operations.[180] The model for predicting the frequency of the AE signal from the Frank–Read source operation during pre-yield deformation has been verified by experiments carried out on a nuclear grade AISI type 316 stainless steel. This model has also been extended to predict the frequency of the AE signal from the grain boundary source operation in the near macroyield region and its validity has also been verified by considering the AE results obtained on aluminium, copper and AISI type 316 stainless steel by different investigators. This study has shown good agreement between the theoretically estimated and experimentally observed values.[180] Table 3 gives a comparison of the frequency of the AE signals predicted by the theoretical model and the frequency of the sensor used or the frequency of the AE signals obtained by spectrum analysis for different materials. This study has established a simple, but reasonably accurate model which could help in selecting the resonant sensors with suitable frequency for detecting both the plastic microyielding and macroyielding with high sensitivity during proof testing of pressure vessels and pipes and other components used in various industries. In other words, knowing the grain size of the materials and by using broadband AE sensor, it is possible to identify from the AE peak frequency of the spectrum, whether the AE signal corresponds to microyielding or macroyielding.

Acoustic emission during α′-martensite formation
The influence of prior cold work on α′-martensite formation during subsequent tensile deformation in AISI type 304 stainless steel has been studied using the AE technique.[181,182] The AE generated during tensile deformation of annealed and cold worked

AISI type 304 stainless steel was studied. More AE in the annealed specimens compared to in the cold worked specimens at higher strain levels has been attributed to higher amounts of strain induced α′-martensite formation in the annealed specimens. The increase in AE activity at low strain levels in a 10% cold worked specimen compared to a solution annealed specimen was attributed to the formation of α′-martensite assisted by prior cold work. Decreased acoustic activity for higher cold worked (20% to 50%) specimens at low strain levels was attributed to a reduced amount of α′-martensite formation due to increased stability of the austenite after higher amounts of prior cold work. A good correlation between the AE and α′-martensite formation in the annealed and differently cold worked specimens was established. Activation of α′-martensite formation by small amounts of prior cold work and retardation by higher amount of prior cold work has been conclusively established by this study.[181,182]

Acoustic emission technique for identifying fracture mechanisms
Smith and Carpenter[183] studied the AE generated from various modes of crack propagation such as: (i) microvoid coalescence, (ii) mixture of microvoid coalescence and intergranular separations, (iii) mixture of microvoid coalescence and rapid surface cracking via transgranular cleavage, (iv) transgranular cleavage, and (v) intergranular separations in 304 stainless steel. Analysis of AE energy and frequency content has shown that the different sources produce distinct AE waveform characteristics. For example, the fracture of inclusions and intergranular cleavage give relatively large high frequency AE as compared to the AE frequency spectrum for transgranular cleavage. Takahashi *et al.*[184] have used the AE signal analysis approach for crack monitoring in fracture toughness tests for AISI 4340 and SA533B steels. They have analysed the frequency spectra of AE at different load levels. It is observed that the high frequency component of AE has increased at higher load level (Fig. 51). The AE technique being dynamic in nature, the different fracture processes would generate different characteristic AE spectra.

Critical assessment
Ultrasonic attenuation measurements have been used for determination of yield strength and fracture toughness, because of the fact that mechanical properties are influenced by grain size and second phase precipitation. However, since the attenuation mechanism is different in different grain size ranges, the relationship between attenuation and yield strength could be either direct or inverse. Hence, prior knowledge of the grain size is required for selecting the appropriate ultrasonic probe frequency.

In ferritic steels, since the micromagnetic parameters are extremely sensitive to the microstructure, the mechanical properties can be reliably assessed from changes in the hysteresis loop parameters and MBE. In quenched and tempered conditions, the coercive force is inversely correlated to hardness. It has been observed that the relationship between hysteresis loop parameters and mechanical properties is

Table 3 Comparison of observed and predicted frequencies of AE signals generated during macroyielding

Material	σ_{maxAE}, MPa	f_{exp}, kHz	d, μm	$f_{predict}$, kHz
316 SS	270	475	50	495
99·9%Al	26·4	150–300	40	434
	25		55	231
	17·6		70	140
	13·2		90	86
	11·6		120	49
Pure Cu	145	150–300	70	211

σ_{maxAE} is tensile stress at which maximum AE is observed; f_{exp} is frequency of sensor used or predominant frequency of AE signal observed; d is grain size; $f_{predict}$ is frequency of AE predicted by present model.
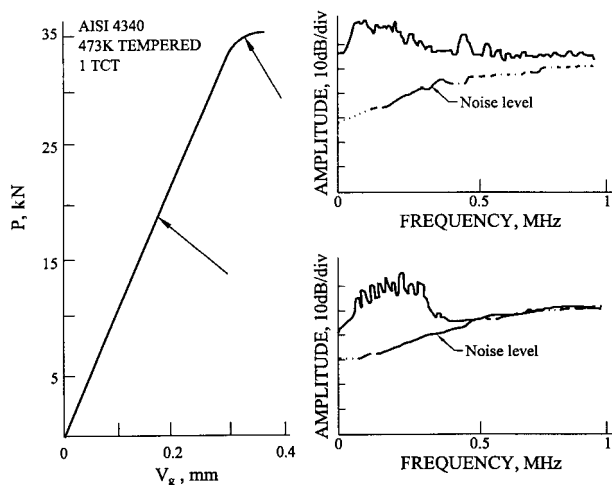
V_g is crack opening displacement

51   Frequency spectra of AE at different load levels (corresponding to regions arrowed on left) during fracture toughness test of AISI 4340 steel[184]

strongly influenced by the amount of carbon content and alloying elements and it is difficult to establish a general correlation. However, a qualitative assessment of variation in tensile strength, impact toughness, etc. can be made from changes in the coercive force. In short term tempered microstructure, the MBE shows good estimation of tensile strength. In long term aged microstructure, the MBE shows a two-peak profile and an appropriate methodology has to be developed for the evaluation of mechanical properties. In the presence of duplex microstructure, the mechanical properties can be more reliably predicted from MBE profiles, since the volume fraction of the two phases strongly influences both the mechanical properties as well as the MBE. Also, the MBE technique is so powerful that it is possible to detect the different stages of progressive tensile deformation from the MBE profile. It can even detect plastic microyielding occurring well before the macroyielding. This extreme sensitivity of MBE can be exploited while monitoring the proof testing of structures. The MBE technique has great potential for on-line assessment of mechanical properties in ferritic steels, but it requires further development of methodologies and standardisation of test procedures.

Recently, the miniature specimen testing methods are gaining a lot of importance, as they would give a realistic evaluation of the mechanical properties of service exposed components/structures. The small punch, shear punch and automated ball indentation methods are found to be more effective in obtaining property values that are in close agreement with results obtained using standard large size specimens. The shear punch test gives a relatively large error band, which needs to be reduced by suitably standardising the specimen and fixture geometry. Also, there is a large shift in the ductile to brittle transition temperature (DBTT) obtained from small punch tests compared to that from conventional Charpy impact tests. This is a growing field for establishing standard

procedures for reliable estimation of mechanical properties.

Since an AE signal is characteristic of the dynamic process causing its generation, the AE technique can be used for characterising plastic deformation processes. The different types of plastic deformation mechanism can be identified from the AE pattern. It is quite interesting to observe that plastic deformation processes such as serrated or discontinuous yielding, precipitate particle shearing, Orowan looping, decohesion and fracture of inclusions and precipitates, and deformation induced martensitic phase transformation, would generate characteristic AE signals. The AE frequency spectrum analysis also indicates the stages of pre-yield and post-yield deformation. This information can be usefully exploited during proof testing of service exposed structures. Similarly, the transgranular or intergranular fracture modes can be identified from the characteristic AE frequency spectra. During a fracture process, the stress intensity factor K can be estimated from the AE counts N, as they are related to expanding plastic zone size. Ductile crack initiation J_{Ic} during the elastic–plastic fracture process can be predicted from the rate of change in the AE counts.

Assessment of creep damage using NDE techniques

Creep is a time dependent deformation process occurring in materials at constant stress and temperature. Creep is the main process responsible for degradation of components and structures operating at elevated temperatures, for example, turbine rotors, castings, turbine blades, boiler tubes, coolant channels, etc. in power plant. Attempts are being made to develop NDT methods for detection of creep damage at the initial stages of its development in order to assess the integrity of a material and, if possible, to avoid rupture. At high temperature, creep deformation is always associated with the synergistic effect of both microstructural variations and strain accumulation which leads to the formation of microvoids, growth and coalescence of voids, microcrack formation and crack growth leading to failure. The microstructural variations, such as phase transformation and precipitation of different second phase particles, are controlled by different diffusion mechanisms. The dislocation dynamics and substructure formation control the strain accumulation.

In situ optical metallography for creep damage

In most thermal power plant high temperature components, creep damage progresses in five stages: nucleation of isolated cavities, growth of cavities, oriented cavities, microcracks, and macrocracks. These progressive stages of creep damage are related to the consumed life fraction of the component.[185] *In situ* metallography or the surface replication technique would provide an indication of the different stages of damage progression.

From the metallographic information, if the number of creep pores per square millimetre N is calculated,

CALCULATED PORE CONCENTRATION, x 10^2
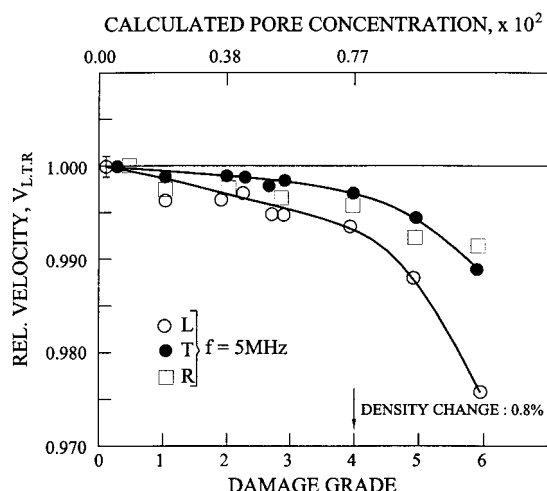
52 Influence of creep damage on ultrasonic velocity in serviced exposed (130 000 h/803 K) 14MoV63 steel[191]

53 Relative ultrasonic velocity as function of damaged area fraction in creep damaged austenitic steel[192]

it is possible to estimate the remaining life of the component for failure from the equation

$$N = (3.3 \times 10^6 \dot{\varepsilon} t) - 3300 \quad \ldots \ldots \ldots (21)$$

from which the strain rate $\dot{\varepsilon}$ can be calculated if the plant operation time t is known. If ε_f is the maximum permitted creep strain for total exhaustion of the material, it will be possible to calculate the time to reach ε_f.[186] This approach gives a conservative estimate of the remaining life. The main difficulty is in fixing the value of ε_f, which varies with steel grade, parent metal, HAZ, weld, etc.

Milanovic *et al.*[187] have used the metallographic parameter A, i.e. a quantity equal to the ratio of the number of damaged grain boundaries to the total number of boundaries in the direction of principle stress, to estimate the residual life of a pipeline bend operating at 803 K/100 MPa. The parameter A is related to remaining life by

$$t = t_o \{ 1/[1 - (1 - A)^9] - 1 \} \quad \ldots \ldots (22)$$

where t is remaining life and t_o is operation time. This approach has been found to give some good correlations in low alloy steels. However, it has been generally observed that it is essential to take a large number of microstructures from different locations and at different depths for obtaining more reliable statistical information on creep damage.

An etching technique using a picric acid with a wetting agent or using 20% HNO_3 with alcohol solution was found to have great potential for the NDE estimation of grain boundary embrittlement caused by carbides and σ precipitation in AISI type 316 and 321 stainless steels which has been related to creep damage and Charpy impact energy.[188]

Ultrasonic attenuation and velocity measurements

Ultrasonic attenuation and velocity are strongly influenced by the microstructural changes associated with creep. An excellent overview of the ultrasonic methods used for the detection of creep damage is given by Stamm.[189] In a review presented by Stigh,[190]
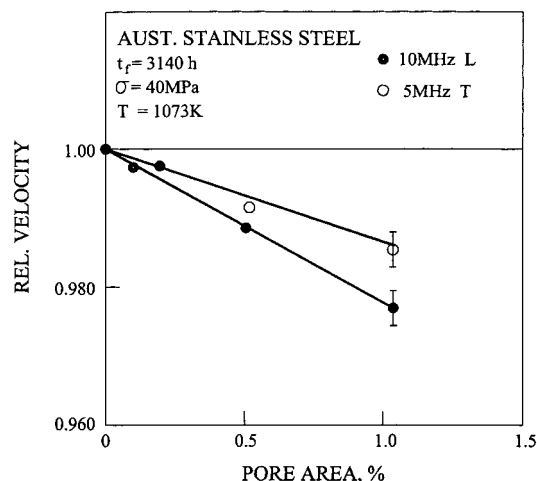
it has been shown that ultrasonic velocity measurements can be used to assess the creep damage occurring by grain boundary cavities and thereby to predict the remaining life.

Ultrasonic velocity measurements seem to have great potential for assessing the creep damage as compared to attenuation measurements. Ultrasonic measurements have been made on 14MoV63 steel tube bend which had failed after 130 000 h/808 K service exposure and contained different grades of damage, namely, isolated micropores, chains of micropores and microcracks.[191] The relative changes in ultrasonic velocities of both longitudinal and shear waves of the same wavelength show a decrease with increase in damage grade. Figure 52 shows the average value of ultrasonic velocity of the longitudinal wave V_L, the shear wave V_T, and the Rayleigh wave V_R versus damage grade, normalised to the corresponding velocities measured in the undamaged state. It can be seen that the velocity decreases nearly linearly up to damage grade 4. For higher damage grades, the velocity drop becomes more pronounced and amounts to 2–3%. Additionally, it is found that the effect is about twice large for longitudinal waves as compared to shear waves and surface (Rayleigh) waves.
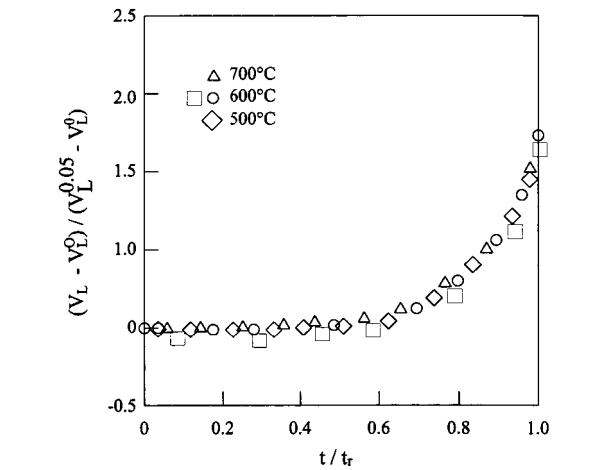
In another study on creep damaged austenitic steel,[192] the change in relative velocities as a function of damaged area fraction (per cent pore area) showed decrease in velocity with increase in damage (Fig. 53). Results from these studies show that pore concentration down to ~0.2% (volume content) can be detected with a measuring accuracy of ±0.001 for relative ultrasonic time-of-flight measurements. The pore concentration is obtained from the velocity change relative to the undamaged material with the same microstructure. Such reference material is available at low loaded parts of the component itself.

Since small variations in grain size will produce larger variations of attenuation coefficient α than creep pores, ultrasonic attenuation measurements are not considered to be appropriate for detection of micropores in creep damaged polycrystalline steels under service conditions which involve grain growth.
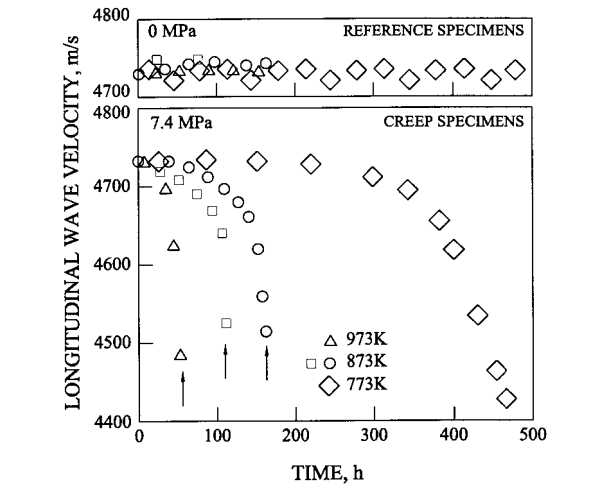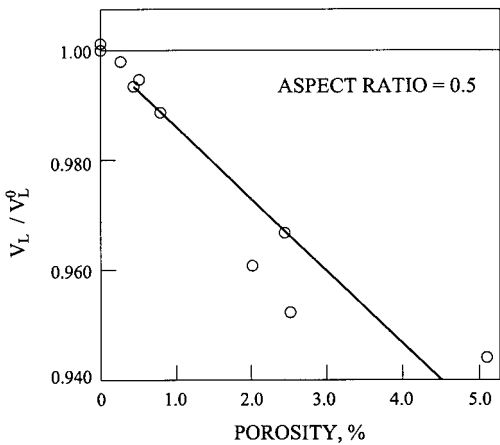
54 Variation in ultrasonic longitudinal wave velocity with creep time at 7·4 MPa for creep damaged Cu (arrows indicate failure)[193]

Hirao *et al.*[193] studied the velocity change caused by accumulated creep damage in polycrystalline pure copper after high temperature tensile loading. The propagation velocities of bulk waves, longitudinal and shear waves polarised parallel and perpendicular to the stress direction, showed a strong sensitivity to intergranular creep controlled by grain boundary cavitation and subsequent microcracking. The velocities decreased slowly with creep time up to approximately 60% of lifetime corresponding to gradual nucleation and growth of grain boundary cavities covering primary and steady stages. At the end of the steady stage, however, the velocities decreased at an ever increasing rate until failure. The total velocity change amounted to several per cent of the original velocities. Figure 54 shows the variations of longitudinal wave velocity V_L with creep time at 7·4 MPa at three different temperatures. Similar variations were observed for shear wave velocity. Figure 55 shows the


V_L^0 and $V_L^{0.05}$ are values for undamaged specimen and at 0·05 creep strain respectively and t_r is time to rupture

55 Normalised variation in ultrasonic longitudinal wave velocity V_L as function of fractional lifetime for creep damaged Cu:[193] because data all lie on single curve, temperature merely controls rate of same damage process


56 Relationship between ultrasonic longitudinal velocity and porosity for creep damaged Cu at 873 K and 7·4 MPa[193] (aspect ratio of pores = 0·5)

normalised variation in longitudinal wave velocity V_L as a function of fractional creep lifetime at different temperatures. All the data points lying on a single curve indicates that the temperature merely controls the rate of the same process of creep damage accumulation. Figure 56 shows the dependence of normalised V_L on porosity for creep damaged specimens at 873 K and 7·4 MPa for different periods. The ratio of the longitudinal wave velocity to its initial value V_L/V_L^0 decreases approximately linearly with increasing porosity.

Von Estorff and Stamm[194] have shown that, in Mn–Cr steels, the cracking of grain boundary facets, a creep damage related to density and size of microcracking, can be identified from ultrasonic velocity measurements. The generation of flaws in the form of cavities or microcracks on the grain boundaries influences the local compliance of a polycrystalline material and this, in general, decreases the ultrasound velocity. Figure 57 shows the ultrasound velocity as a function of the position within the gauge length of a non-ruptured Mn–Cr steel (AMCR 0033) specimen exposed to creep for 146 h at 150 MPa and 923 K. The comparison of the frequency spectrum of the first and second back wall echoes in virgin and creep specimens showed that the intensity of the echo is significantly reduced in the creep specimen and the
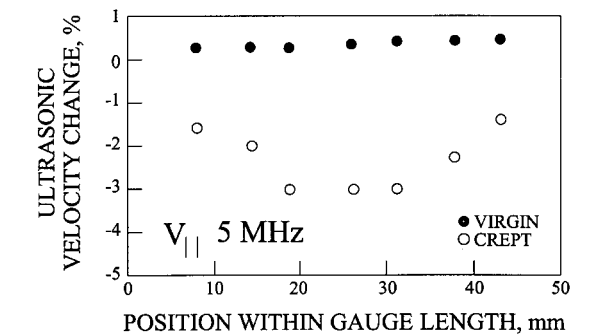
57 Ultrasonic velocity measurement as function of position within gauge length of non-ruptured Mn–Cr steel specimen exposed to creep for 146 h at $\tau_0 = 150$ MPa and $T = 923$ K[194]
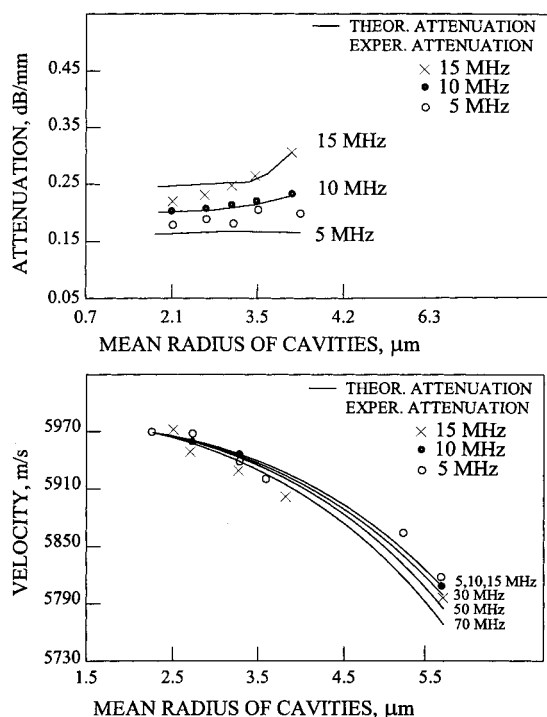
58 **Variation in theoretical and experimental ultrasound attenuation and velocity values as function of mean radius of cavities in 0·5Cr–0·5Mo–0·25V steel[195]**

maximum of the reflected intensity is shifted to a lower frequency.

Perez *et al.*[195] have studied the creep damage accumulation in 0·5Cr–0·5Mo–0·25V steel using ultrasound attenuation and velocity measurements. They compared experimental values with theoretical values. Figure 58 shows the variation in the experimental and theoretical values of velocity and attenuation as a function of mean radius of cavities. This study establishes the models to correlate the metallurgical and ultrasonic parameters.

Brathe[196] showed that the decrease in velocity with progress in creep damage could be used to measure the level of damage in commercially pure copper. In the case of creep rupture tests, the velocity was found to decrease with increase in creep rupture time. The velocity decrease was up to 15% at rupture. Similarly, Stigh *et al.*[190] have found about 8% decrease in velocity in creep tested AISI type 316 stainless steel samples. The theoretical results showed much smaller dependence of density on velocity than the experimental results. This was attributed to the fact that the cavities assumed in the theory are spherical in nature, whereas the creep cavities formed in practice are generally found to be oblate spheroids which may have low influence on density. In order to eliminate the interference of microstructural changes on the ultrasonic velocity and to consider only the influence of creep cavities and/or microcracking, the velocity of the creep damaged specimens was normalised to that of the equivalent thermally aged specimens.

The theoretical description of the propagation of an acoustic wave in a material containing voids is

generally based on the scattering and multiscattering processes[197–199] and experimental results consistent with theoretical prediction have been obtained.[200,201] As pointed out, when the cavities are the result of a creep process in polycrystalline materials, clear deviations between theory and measurements have been detected.[202] Gomez *et al.*,[203] from a systematic study, reported the possibility for complete characterisation of creep damage in steel by using acoustic measurements and also improved the theoretical models by considering different sources of losses.[204] A semi-empirical procedure has been suggested for assessment of creep damage. Gomez *et al.*[203] have also demonstrated the usefulness of attenuation measurements in addition to velocity measurements, normally used by various other investigators, for improving the knowledge of creep damage. In common with the velocity measurements, the attenuation measurements, particularly the frequency dependence on attenuation, are also found to be sensitive to creep damage. The dislocation and structural changes taking place during creep damage were found to influence the attenuation. In order to take into account such effects, the attenuation coefficient was expressed as

$$\alpha = a_1 f^2 + a_2 f^4$$

where the first term on the right-hand side is related to dislocation damping, molecular relaxation and magnetic domain wall effects and the second term is due to scattering losses.[192] It is necessary to take multiscattering into consideration for explaining the variation in ultrasonic velocity with creep damage. The equations given below describe the influence of porosity on velocity V with (equation (23)) and without (equation (24)) considering multiscattering

$$(V_0/V)^2 = 1 - (A_1 + B_1 k^2 a^2) + (D_{13} + D_{14} k^2 a^2) \qquad \dots \dots \dots (23)$$

$$V_0/V = (A_1 + B_1 k^2 a^2) d/2 \qquad \dots \dots \dots (24)$$

where V_0 is the velocity of the specimen without creep damage ($\Delta V = V_0 - V$); A_1, B_1 are constants depending on the particular material; k is the wave number for the ultrasonic wave ($= 2/\lambda_1$, λ_1 being the wavelength); a is pore diameter; D_{13}, D_{14} are functions of ratio of wave number for transverse and longitudinal waves; and d is grain size. The porosity P is given by

$$P = \tfrac{4}{3} a^3 n_o$$

where n_o is cavity concentration. This study indicated that for porosity greater than $2·5 \times 10^{-3}$ the multiscattering expression gives a better approximation to the metallographic results. This study also showed that both ultrasonic velocity and attenuation measurements could effectively be used for assessment of creep damage, and relate the behaviour with theoretical modelling after taking into consideration multiple scattering and the influence of other microstructural and substructural changes.

Jayakumar *et al.*[205] have used ultrasonic velocity measurements to assess the creep damage in service exposed 0·5Cr–0·5Mo–0·25V and 1Cr–0·5Mo ferritic steels. The density of the material is related to the cavity formation in the material, which, in turn, is
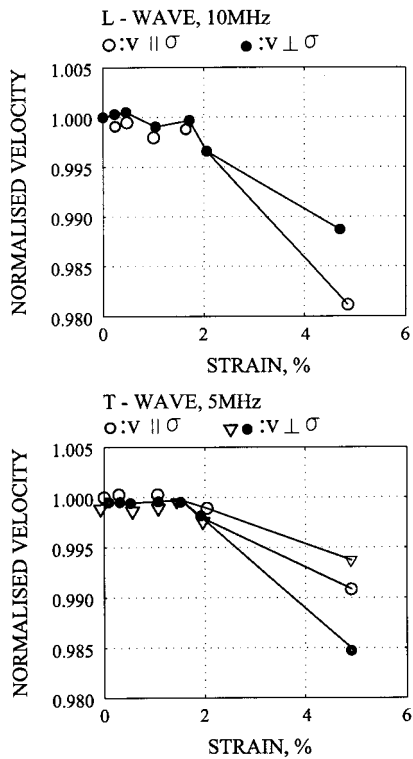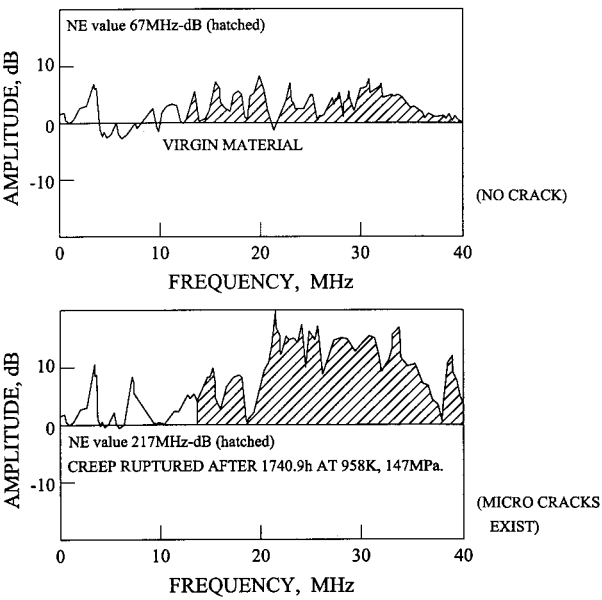
59 **Variation with creep strain of normalised velocity of ultrasonic waves propagating parallel and perpendicular to direction of stress in service exposed 0·5Cr–0·5Mo–0·25V steel[205]**

NE = noise intensity

60 **Principle and typical results of noise value analysis from tests carried out on virgin and creep ruptured specimens of AISI 321 stainless steel:[206] technique is suitable for steels that produce microcracks/microvoids**

related to the extent of creep damage. It has been observed that the velocity decreases with increase in cavity formation.[205] Any decrease in velocity then should indicate creep damage. A good correlation between the velocity and the density could be obtained on both laboratory samples and samples prepared from service exposed components. It is also possible to detect the presence of any oriented cavities/microcracks by using the velocity measured in different directions by both longitudinal and shear waves of the same wavelength. It has been found that the velocity change is less for longitudinal waves propagating perpendicular to the load direction compared to that parallel to the load direction (Fig. 59). This indicates that the cavity chains/microcracks are aligned perpendicular to the load direction.

Ultrasound noise analysis

Assessment of creep damage by utilising ultrasound techniques through noise analysis is quite promising. It is capable of showing the occurrence of microcracks, voids, cavities, and other such flaws. In the noise analysis method, the amount of noise contained in a given frequency range is determined as a damage indicator by conducting frequency analysis on the back scattered noise (Gross echoes).[206] Figure 60 shows typical results of the noise analysis method. Figure 61 shows a linear relationship between microcrack area and noise values determined for creep ruptured specimens of AISI type 321 stainless steel. However, this method is neither effective for detecting the creep deformation, nor is it sensitive enough for steels which do not produce voids or cracks.

Magnetic techniques

Coercive force and residual induction

Creep damage is characterised by the formation of pores or voids, which are associated with magnetic free poles. Magnetic hysteresis loop methods have shown some interesting trends while studying this type of damage.[81,126,207] It has already been mentioned that when a domain intersects a pore or a second phase particle, there is a reduction in magnetostatic energy which in turn would affect the coercive force H_c. The H_c has been found to increase linearly while the saturation magnetisation M_s decreases with percentage porosity.[81] Both the size and the volume fraction of the pores were found to influence the coercivity[80,83,85] in iron, and the following equation was found to be valid for pore diameters $< 0·1$ μm
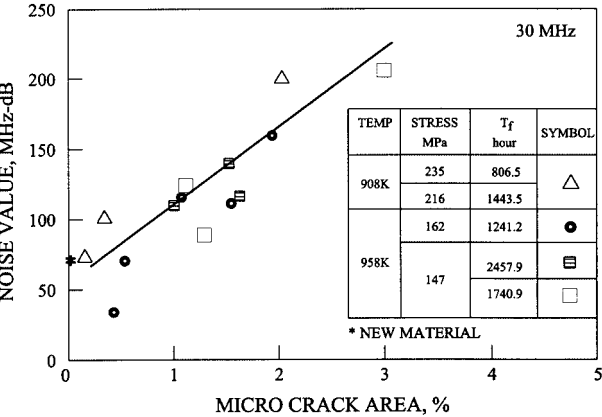
61 **Relationship between microcrack area ratios and noise values determined for creep ruptured specimens of AISI 321 stainless steel[206]**
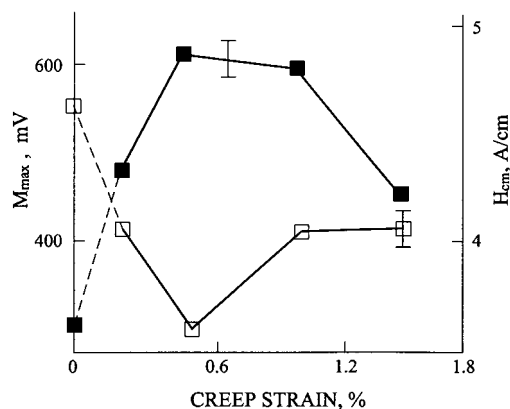
62 Variation in M_{max} (black squares) and H_{cm} (open squares) with percentage creep strain for 13CrMoV44 steel service exposed to 90 MPa at 803 K[211]

63 Radius distribution function of voids for 5 and 10% creep deformed Alloy 800H[212]

$$H_c = [5 \times 10^7 (a/2) + 10^{19} (a/2)^3] P^{2/3} \qquad . \quad . \quad . \quad (25)$$

where a is pore diameter and P is the volume fraction of pores. The energy of the demagnetising field for pores was found to be two orders of magnitude higher than the energy of the domain wall. Closure domains form when the pore diameter is greater than 0·1 μm and therefore H_c was found to decrease for $a > 0·1$ μm.
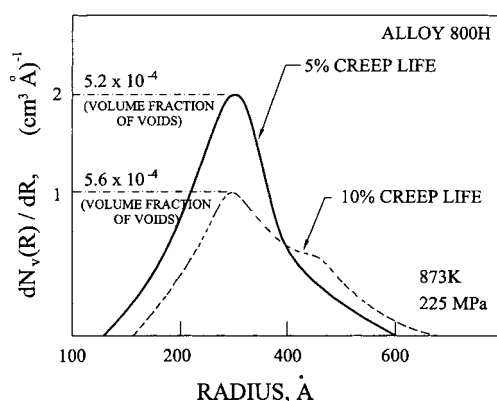
Several studies[208–210] carried out on service exposed Cr–Mo steels showed that a lower remanence and higher coercive force are indicative of creep damage. The product of coercivity and remanence also seems to be a good indicator of the level of creep damage. Considering the large scatter, they have also tried neural network analysis with the magnetic parameters and observed a significant improvement in the assessment of creep damage.

Magnetic Barkhausen emission technique for creep damage

Parameters of MBE such as M_{max} (the maximum value of the MBE signal generated during a hysteresis cycle) and H_{cm} (the magnetic field at which the maximum MBE occurs) are used for assessing creep damage. Figure 62 shows the variation in MBE parameters for 13CrMoV44 steel service exposed at 803 K and 90 MPa.[211] These studies indicate that MBE parameters are strongly influenced by creep damage. The initial decrease in H_{cm} and increase in M_{max} indicate the stress enhanced aging of the microstructure resulting in coarsening of laths/grains and second phase precipitates which has a dominant effect on magnetisation processes compared to that of increase in dislocation density. The increase in H_{cm} and decrease in M_{max} at higher creep strain indicate the dominant effect of cavities, which strongly pin the domain wall movement during magnetisation. However, further studies based on a multiparameter approach are required to clearly identify the effect at lower and higher creep strain values, because the H_{cm} and M_{max} show more or less similar values.

Small angle neutron scattering (SANS)

The stress enhanced growth of second phase precipitates and cavities provides strong scattering centres of neutrons. Hence, SANS can be considered a good NDE tool for creep damage assessment. The SANS technique has been used to study void growth during creep in Alloy 800H.[212] Figure 63 shows the radius distribution function of voids for 5 and 10% creep deformed Alloy 800H samples. The results indicate a clear shift in the mean size of the voids as the creep strain increases. The volume fraction of voids increases by 7% when the creep strain increases from 5 to 10%. Page *et al.*[213] have studied void nucleation rate, growth rate, void size distribution, etc. in samples subjected to creep–fatigue interaction, using SANS measurements.

Kim *et al.*[121] have compared the effect of fatigue and creep deformation in the tempered condition on SANS data. The marked difference between the undeformed and deformed samples has been attributed to the faster growth of carbides resulting in a reduction in the number density of carbides in deformed samples. The coarse carbides in deformed samples scatter at very low angles and hence the scattering intensity at higher scattering vectors decreases in deformed samples. Similarly, the high temperature fatigue also produces significant changes in the scattering profile. It has been observed that the changes in the scattering profile are mainly caused by the variation in the second phase precipitation behaviour and not by the changes in the dislocation substructure.

Critical assessment

It is apparent that *in situ* metallography gives accurate information about microstructural changes (such as grain coarsening, void formation, micro- and macrocrack formation, etc.) associated with creep damage. However, it cannot give information about phenomena such as precipitation coarsening and dislocation substructure evolution in the early stages of creep. Also, the prolonged times necessary for measurements restrict the accuracy on statistical information.

Extensive studies have been carried out using ultrasonic methods for assessing creep damage in a wide range of materials. The ultrasonic velocity changes more significantly compared to attenuation. The ultrasonic velocity measurement gives a sharp indi-

cation with reduction in velocity after the formation of microcracks. But in the early stages, the changes in velocity do not clearly reflect the damage progression. However, the presence of interconnected porosity decreases the velocity. In the later stages, it is even possible to quantitatively estimate the porosity from the changes in ultrasonic velocity.

In the case of ferritic steels, the micromagnetic technique seems to be the better method for identifying the progressive creep damage right from the early stage. However, the microstructural evolution phenomena, such as grain coarsening and dislocation substructure variations, influence the magnetic parameters in a synergistic manner. The grain growth would reduce the coercive force, whereas the increase in dislocation density would increase the coercive force and decrease the residual induction. It is difficult to identify such complex variations from the magnetic hysteresis loop parameters. However, such complex variations can be understood from the MBE profile, by analysing the slope of the rising profile, peak height and peak position. So far, studies have not been carried out in the direction of isolating the influence of grain growth and dislocation substructure, which is a potential area for future research. The combined use of hysteresis loop and MBE would give better insight in characterising the creep damage.

The SANS technique is extremely sensitive to changes in second phase precipitation and void formation during creep. It is possible to quantify the size and distribution of precipitates and voids using SANS, but it does not indicate the grain coarsening and dislocation substructure evolution. The main problem with SANS is in-service application on actual components.

Assessment of fatigue damage using NDE techniques

It has been well established that fatigue properties are influenced by the microstructure and surface residual stresses. Some NDE techniques are used to assess the endurance or fatigue limit. In components subjected to fatigue loading, the accumulation of strain by cyclic plastic deformation occurs prior to the formation of microcracks, which later coalesce to form a macrocrack. The cyclic plasticity is associated with the different stages of dislocation substructure formation. The rearrangement of dislocations in various stages involves the formation of dislocation walls and persistent slip bands, which then convert into cells and subgrains with accumulating number of cycles. Many studies have been carried out to identify the different stages of fatigue damage accumulation and thereby predict the remaining life of a component. This section gives the status of various NDE techniques, which can be used to assess the fatigue properties and the progressive damage.

Estimation of fatigue limit

X-ray diffraction (XRD) technique
The fatigue damage process is usually associated with the accumulation of strain in persistent slip bands and development of intrusions and extrusions on the
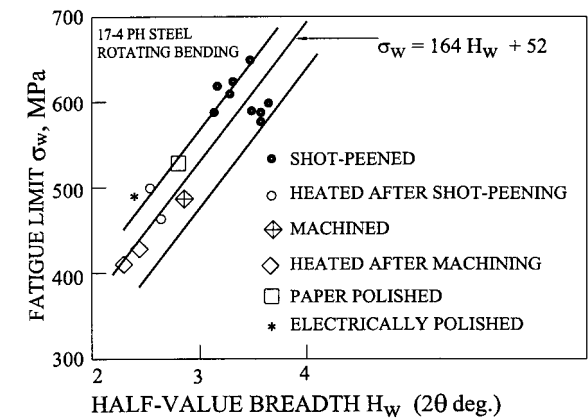
64 Fatigue limit versus half-value breadth from rotating bending tests on 17-4PH steel[214]

specimen surface promoting roughness of the surface. This in turn changes the residual stress pattern on the surface of the material. Hence, the determination of residual stress can give some indirect information on the accumulated fatigue damage. Since XRD is very sensitive to changes in crystalline structure, diffraction profile analysis, such as simple measurement of profile broadening or half-value breadth, can yield information on fatigue damage. In a study by Toru Goto[214] on material strength evaluation and damage detection by the XRD technique, it was shown that the half-value breadth could be related to the fatigue limit. Figure 64 shows a plot of fatigue limit against half-value breadth obtained from fatigue test specimens having different initial surface conditions obtained by machining, shot peening, paper polishing and electropolishing of 17-4PH steel. It was shown that it would be possible to correlate the half-value breadth H_w with the fatigue limit σ_w (MPa) using the following linear equation

$$\sigma_w = 164 H_w + 52 \quad . \quad . \quad . \quad . \quad . \quad . \quad . \quad (26)$$

Identification of different stages of fatigue damage accumulation

Ultrasonic methods
A study of Alloy 800H[215] to monitor high temperature low cycle fatigue damage shows very interesting changes in ultrasonic parameters. Fatigue loading leads to modification in the dislocation substructure, initiation of microcracks in the near surface regions and their growth culminating in fatigue failure. The interaction between ultrasound and dislocations has been described by the vibrating string model. It is observed that the changes in the dislocation substructure produced by fatigue loading are too small to lead to measurable changes in ultrasonic velocity. The ultrasonic absorption, however, decreases linearly with increases in fatigue life fraction, which is attributed to the development of dislocation substructure such as cells and subgrains.[215] Figure 65 shows the changes in ultrasonic absorption and velocity as a function of fraction of life.

A laser ultrasound absorption study[216] was carried out on Alloy 800H samples subjected to tension–compression low cycle fatigue tests at different stress
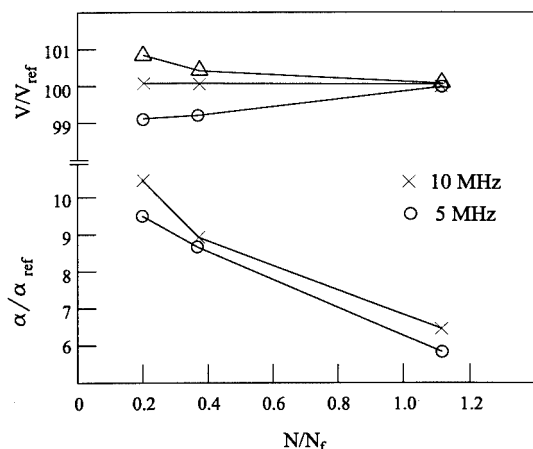
65 Variation in relative ultrasonic absorption and velocity as function of fatigue life fraction in Alloy 800H:[215] dislocation cell formation decreases absorption, whereas there is no appreciable change in velocity

ranges and strain rates (Fig. 66). It can be seen that the absorption decreased with increasing number of cycles to fracture N_f (Fig. 66). It has been found that the absorption parameter exhibits less scatter and is more sensitive than the velocity parameter. It has also been reported[216] that laser based ultrasound absorption measurements by the reverberation technique can be conducted up to very high temperatures (1400 K) using small specimens.

Magnetic techniques
Hysteresis loop methods
Changes in magnetic hysteresis loop properties with stress cycling in steels have been used to predict the fatigue life.[217,218] It has been observed in EN1 steel (0·1 wt-%C) that during high cycle fatigue the change in coercive force ΔH_c goes through a maximum, whereas the change in residual induction ΔB_r goes through a minimum as the number of cycles increases. This is attributed to the changeover from cyclic hardening to softening. However, both ΔH_c and ΔB_r are influenced by the stress amplitude.

Devine *et al.*[88] have studied the effect of cyclic stress on the magnetic hysteresis parameters in AISI
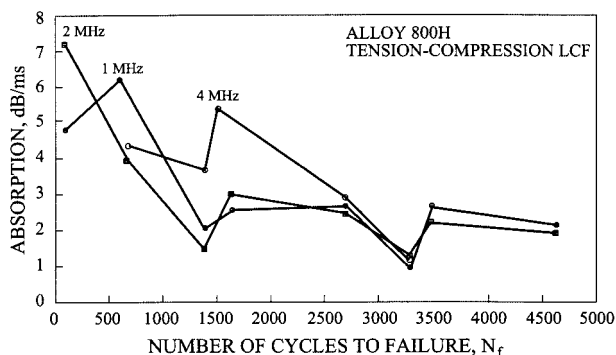
LCF = low cycle fatigue

66 Ultrasonic absorption as function of fatigue cycles at different frequencies for specimens of Alloy 800H[216]
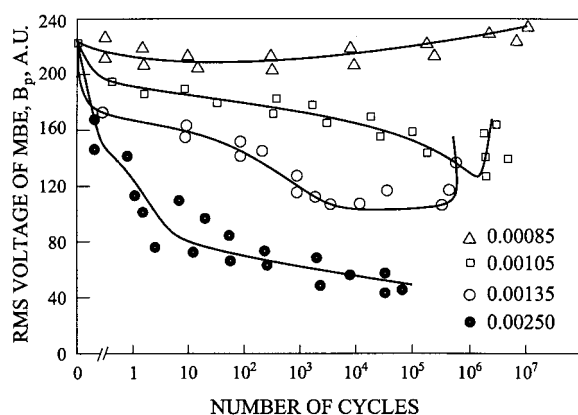
67 Change in rms value of MBE (parallel to stress direction) as function of number of fatigue cycles for different strain amplitudes: tests carried out on normalised low C steel[222]

4340 steel during a constant total strain amplitude (0·005) test. The coercivity was found to decrease rapidly in the initial stages due to fatigue softening, which is attributed to the reduction in dislocation density due to annihilation. It was also found that the remanence of the material increases sharply during the first few stress cycles due to softening of martensite, but subsequently the increase was less pronounced. It was found that the magnetic properties were dependent on both the strain amplitude and the number of stress cycles experienced.

Govindaraju and co-workers[219,220] have studied the effect of fatigue damage on coercive force and remanence in a bridge steel and A533B low alloy ferritic steel at various life fractions during a constant strain amplitude ($\pm 0·003$) low cycle fatigue test. In the bridge steel, they observed that both the coercive force and remanence increase initially corresponding to a load drop and then remain constant in relation to load. The drastic drop in the load corresponding to the crack propagation stage is indicated by the rapid drop in both the coercive force and remanence. However, in the A533B steel, during final load drop, the coercive force has been found to increase and the remanence has been found to decrease.

Bi and Jiles[221] have used the changes in magnetic properties and mechanical modulus to detect fatigue crack propagation in A533B steel and Cr–Mo steels. They observed that, during the crack propagation stage, the remanence decreases linearly similar to modulus whereas the coercive force increases with number of cycles. It has been found that there exists a linear relationship between remanence and modulus as well as between modulus and fatigue damage.

Magnetic Barkhausen emission method
Karjalainen and co-workers[150,151,222] have conducted extensive cyclic bending tests on normalised low carbon steel at stresses below and above the fatigue limit to determine the effect of fatigue loading on MBE. They measured the MBE level parallel B_p and perpendicular B_t to the stress direction at various stages of fatigue life. Figure 67 shows the variation in B_p in unloaded fatigue samples as a function of number of cycles. The studies indicate the possibility
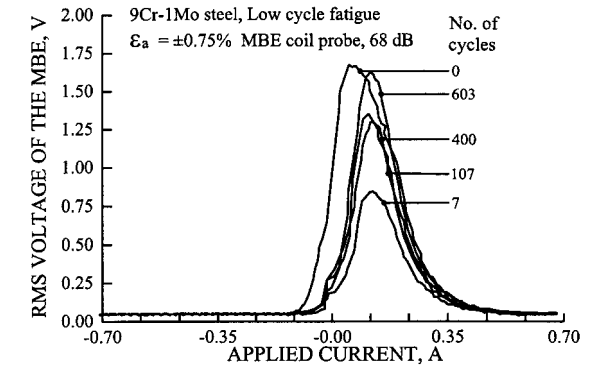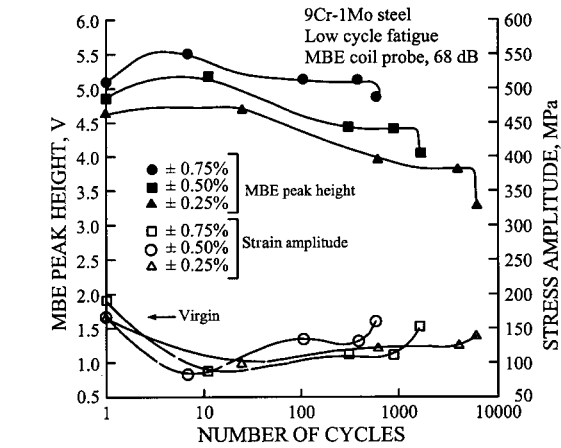
68 **Typical variation in rms voltage profile of MBE as function of current applied to yoke for different stages of LCF life: tests carried out on 9Cr–1Mo steel[225]**


69 **Variation in stress amplitude and MBE peak height at different stages of LCF life of 9Cr–1Mo steel specimens tested under three different strain amplitudes[225]**

to evaluate the actual state of fatigue. At strain amplitudes just below the fatigue limit (strain amplitude 0·00105 and 3×10^6 cycles), B_p remains more or less constant till $\sim 10^7$ cycles. At strain (stress) amplitudes above the fatigue limit, the changes in B_p increase rapidly. First, the B_p decreases with number of cycles indicating fatigue hardening and then increases due to softening. The extent of changes in B_p at various life fractions is strongly influenced by the strain amplitude. It has been shown that by measuring the variation in B_p and B_t during the first 5×10^4 cycles, it should be possible to distinguish whether the load is above or below the fatigue limit, thereby allowing prediction of the fatigue life without knowing the actual load level. The authors have also observed[222] that the fatigue softening and hardening processes introduce specific changes in the shape and area of the rms voltage of the MBE versus stress loops. They have shown good correlation between the variations in B_p and the compressive residual stress as a function of number of cycles. Later, Tiitto[223] reviewed the use of MBE in evaluating fatigue damage. He showed that stress relaxation due to fatigue and overloading could be easily detected by MBE measurements.

Govindaraju *et al.*[224] used MBE for identifying the three different stages of low cycle fatigue damage in medium strength steel (A533B). They observed an initial increase in MBE with decrease in load, which was attributed to fatigue softening caused by breaking of dislocation tangles. Then, corresponding to the saturation stage, they observed a decrease in MBE due to formation of slip lines on the surface. The crack propagation stage was marked by a rise in MBE level. This was attributed to additional closure domain formation at the free surfaces of the crack, which results in increased domain wall density. Significant changes in MBE amplitude were observed in the first 30% and in the last 20% of the fatigue life.

Recently, the MBE technique has been used to assess progressive low cycle fatigue damage in 9Cr–1Mo ferritic steel.[225] Total strain controlled fatigue tests were conducted at ambient temperature employing plastic strain amplitudes of ± 0.25, ± 0.50 and $\pm 0.75\%$. For this study, MBE measurements have been performed on low cycle fatigue tested

specimens interrupted at various life fractions. The various stages of deformation and fracture under low cycle fatigue loading, such as cyclic hardening, cyclic softening, saturation and surface crack initiation and propagation, have been examined and identified using the peak height value of the rms voltage of the MBE. Figure 68 shows the typical variation in the rms voltage profile of the MBE as a function of current applied to the yoke for different stages of low cycle fatigue life. Figure 69 shows the variation in stress amplitude and MBE peak height at different stages of low cycle fatigue life under three different strain amplitudes. The cyclic hardening, which occurred in the early stage of low cycle fatigue cycling in 9Cr–1Mo steel, decreases the MBE peak height value. The reduction in MBE peak height value increased with increase in the amount of hardening, which in turn depends on strain amplitude. The progressive cyclic softening stage displayed a reversal in MBE response, i.e. the MBE peak height value increased with softening. Further, the saturation stage, where the stress value remained constant for a large number of cycles due to formation of stable dislocation substructure, results in a constant value of MBE. Finally, the onset of rapid stress drop and cusp formation in the stress–strain hysteresis loop, which indicates surface crack initiation and propagation, exhibited a rapid increase in the MBE peak values. This is attributed to the movement of additional reverse domains produced at the crack surfaces. The rapid increase in MBE due to crack initiation and propagation has been confirmed by the measurement of MBE on the crack and away from the crack using a surface MBE probe. The correlation of MBE with dislocation substructure evolution in different stages of low cycle fatigue life has been confirmed from TEM investigations.[54] These studies indicate that MBE can be used to monitor accumulation of fatigue damage on components exposed to cyclic loading and predict the remaining service life.
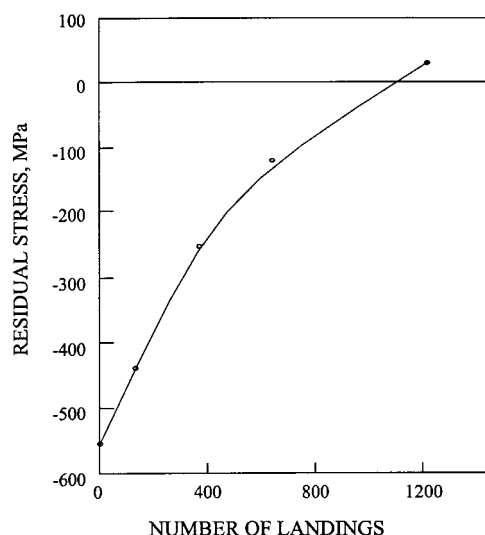
Positron annihilation (PA) technique
As already mentioned, positron lifetime is strongly influenced by changes in dislocation density and
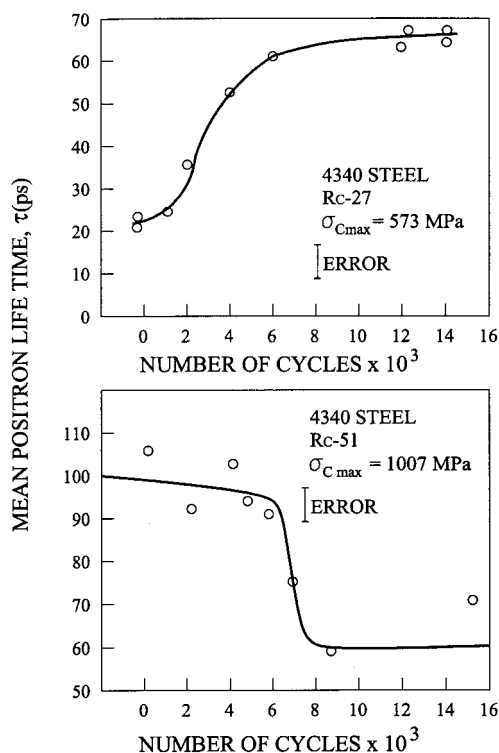
70 Mean positron lifetime versus number of fatigue cycles for 4340 steel having initial Rockwell hardness values of 27 and 51 HRC:[226] in soft (annealed) samples, cyclic hardening increases positron lifetime, in hard (quenched) samples, softening decreases positron lifetime

71 Variation in surface residual stress in high strength steel landing gear with number of landings[230]

dislocation substructure. This has been exploited to assess fatigue damage using the PA technique. Figure 70 shows variations in positron lifetime versus the number of fatigue cycles for soft (annealed) and hard (quenched) samples of 4340 steel; the maximum applied stress in fatigue loading is equal to two-thirds of the yield stress.[226] For the soft samples, positron lifetime increases rapidly as a result of fatigue hardening, from an initial value of about 20 ps to a value of about 65 ps at fracture. For the hard samples, the positron lifetime decreased by almost 40% at about 10 000 cycles. This is attributed to the work softening phenomenon associated with migration of interstitial impurities to positron trapping sites thereby removing the vacancy sites. The usefulness of this technique for design and for damage assessment is indicated by a long region of small but significant slope seen in the behaviour of the positron lifetime as a function of fatigue cycles. In another study by Nishiwalei *et al.*[227] on AISI 304 stainless steel subjected to cold rolling and fatigue, it has been shown that the measurement of positron lifetime and Doppler broadening can predict the production of dislocations and vacancy clusters in the initial stages of fatigue damage.

Positron annihilation line shape analysis has been used to study fatigue damage in AISI type 316 stainless steel and SA508 low alloy steel.[228,229] It was observed that the S parameter is very sensitive in the early stage of fatigue life (10% of life) due to the increase in dislocation density, but showed little sensitivity in the later stages of fatigue life where crack initiation and growth predominate.
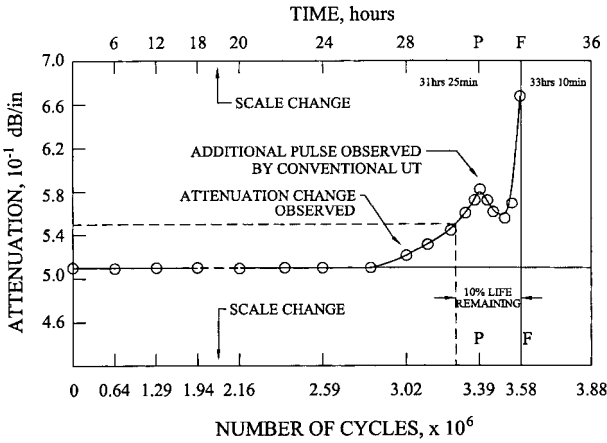
X-ray diffraction (XRD) measurements

Accumulation of fatigue damage in components is manifested as an alteration in surface stresses. During fabrication of many critical components, such as steam turbine blades and aircraft landing gears, to enhance fatigue life, high compressive stresses are introduced, particularly in the near surface regions. In service, these components undergo fatigue loading, thus leading to redistribution of surface residual stresses prior to initiation of cracks. It is therefore advantageous to measure non-destructively the surface residual stresses to assess the extent of redistribution of the surface stresses, which is a measure of the accumulated fatigue damage. This would enable a decision to be made on continued use/rejuvenation/replacement of such components.

The potential of the XRD technique for evaluation of fatigue damage in the case of steam turbine blades and aircraft landing gear has been successfully demonstrated by Rai *et al.*[230] The measurements made on new aircraft landing gear showed compressive stress of the order of 500–600 MPa. The used landing gear showed a gradual changeover from the original compressive stress of 500–600 MPa to a tensile stress of 100 MPa, with increase in the number of landings (Fig. 71). The presence of tensile stresses on the top surface of the used landing gear indicated progressive redistribution of residual stresses due to accumulation of fatigue damage. All these measurements have been made at different regions prone to fatigue damage (based on the design analysis). From the basic understanding of the fatigue process, the trend in redistribution of surface residual stresses and the stresses in the depth direction (up to 300 μm) could be effectively explained. These studies have also been extended to qualify the rejuvenation process employed for extending the life of the landing gear. The rejuvenated landing gear showed compressive stresses of the order of 350–400 MPa. These stress levels are adequate, as rejuvenated landing gear would be expected to be used for only two-thirds of the landings employed in the case of new landing gear, prior to its rejuvenation.

**72 Typical plot of ultrasonic attenuation as function of number of fatigue cycles for Al[231]**

73 Changes in half-value breadth ratio H_w/H_{wo} during high temperature (773 K) low cycle fatigue (constant strain cycling), and crack initiation line in Cr–Mo–V forgings[214]

Monitoring fatigue crack initiation and growth using NDT techniques

Ultrasound attenuation
In a study by Joshi and Green,[231] ultrasound attenuation measurements were used for continuous monitoring of fatigue damage during cyclic testing of polycrystalline aluminium and steel specimens. It was observed that the ultrasound attenuation initially remained constant, increased slowly, and then increased rapidly just prior to fracture. Figure 72 shows a typical plot of the variation in attenuation with number of cycles for aluminium. The increase in attenuation has been attributed to strain accumulation and the associated formation of microcracks. It is observed that the change in attenuation value can indicate the impending failure several hours before the conventional ultrasound technique could detect an additional echo caused by the presence of a macrocrack (as indicated in Fig. 72).

X-ray diffraction studies
An XRD study has been carried out by Toru Goto[214] for fatigue life estimation of steam turbine rotors of Cr–Mo–V forged steel. For a turbine, there are many types of start-up, such as cold start, warm start and hot start. The change in thermal stress during one cycle is not uniform for a given groove root. It was observed that the half-value breadth of the XRD peak changes significantly during high temperature low cycle fatigue. Figure 73 shows the results of constant strain cycling, plotting the changes in half-value breadth ratio H_w/H_{wo} and the crack initiation line against the number of cycles. Crack initiation is defined as the occurrence of a surface crack of about 1 mm in length. It can be observed from the figure that, except at the initial stage, the relation between the half-value breadth ratio and the number of cycles can be represented by a straight line for a given strain cycling on a log plot. A constant slope has also been observed for all the straight lines representing the various strain cycling processes. It was also possible to represent the relationship between the half-value breadth and the number of cycles at crack initiation by a straight line, which is shown as the crack initiation line in Fig. 73.
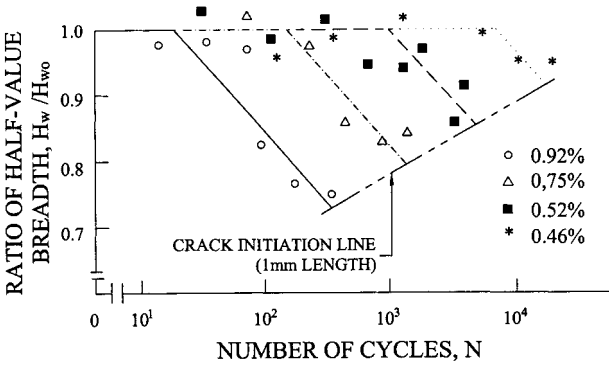
From this study, a simple method (illustrated by Fig. 74) has been proposed for fatigue life estimation. After measuring the half-value breadth ratio and the number of start-ups, the crack initiation point can be obtained by drawing a constant slope straight line as mentioned above from the H_w/H_{wo} point to the already established crack initiation line. From the number of cycles corresponding to the crack initiation point, one can estimate the damage N/N_o or the residual life $N_o - N$. This method has been validated on various specimens. Figure 75 shows the estimated fatigue life fraction against the actual life fraction for various types of strain cycling on Cr–Mo–V forgings. This study shows that the XRD technique can be used for estimating the remaining fatigue life within a factor of two.

Acoustic harmonic measurements
An acoustic harmonic generation study during fatigue by Buck *et al.*[232] on 2024 aluminium alloy revealed a complex dependence of stress on harmonic generation after 5000 cycles (Fig. 76). This has been attributed to the presence of surface cracks of average length 15–20 μm with a density of about 100 cm^{-2}. It was observed that initial crack closure leads to a peak in the vicinity of zero applied stress after 5000 cycles. Advanced stages of fatigue damage can be identified by acoustic harmonic measurement. However, initial stages cannot be assessed as the substructural changes do not influence the harmonic generation.
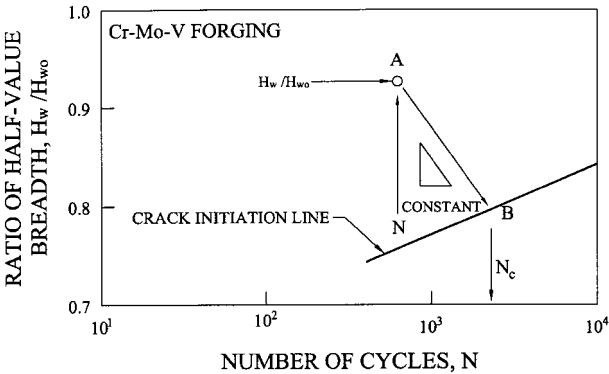
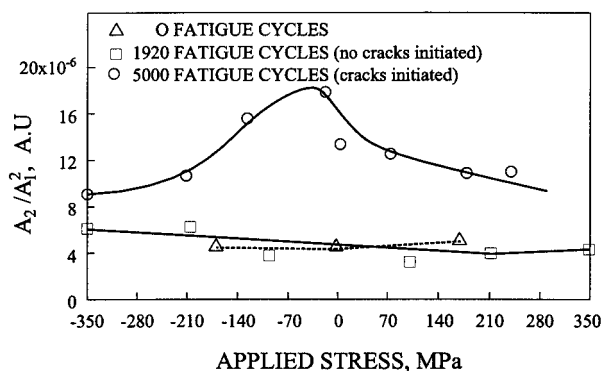**74 Illustration of method of fatigue life estimation in Cr–Mo–V forgings[214]**
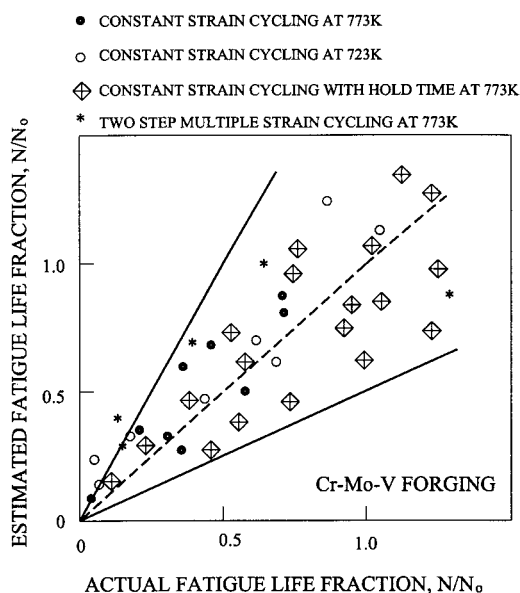
75 **Estimated fatigue life fraction versus actual fatigue life fraction for various types of strain cycling in Cr–Mo–V forgings[214]**

77 **Peak value of normalised second harmonic generation in 7075 Al alloy as function of fatigue life[233]**

Another study[233] on 7075-T651 aluminium alloy clearly shows the potential of this technique for fatigue monitoring. Figure 77 shows the peak value of the harmonic generated as a function of fatigue cycles. Crack initiation is clearly indicated by the rapid increase in the peak value at about 30% fatigue life. At 60% of expended life, the harmonic had increased by about a factor of four.
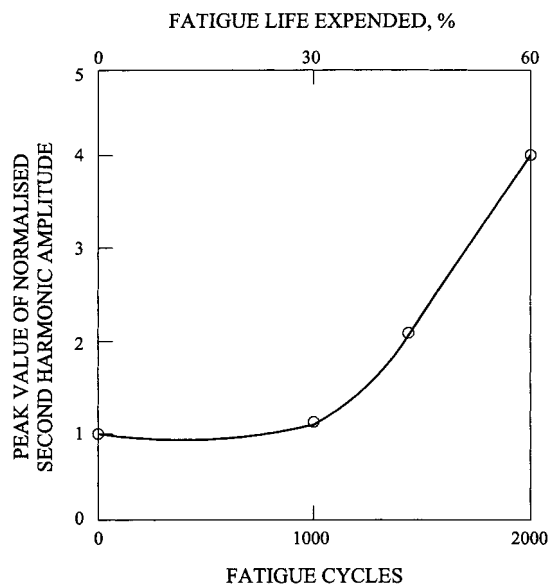
Laser scattering technique

When a fatigued specimen surface is illuminated by a laser beam, the reflected and scattered light intensity distribution, in the form of a speckle pattern, carries information about the surface roughness and hence the fatigue damage. Generally, optical correlation measurement and spectrum width parameters are used for the detection of fatigue crack growth. Haworth *et al.*[234,235] have assessed fatigue damage in 2024 Al alloy using the optical correlation technique. They have correlated the microcrack density with the optical correlation intensity as a function of number of fatigue cycles in high strength 2024 Al alloy
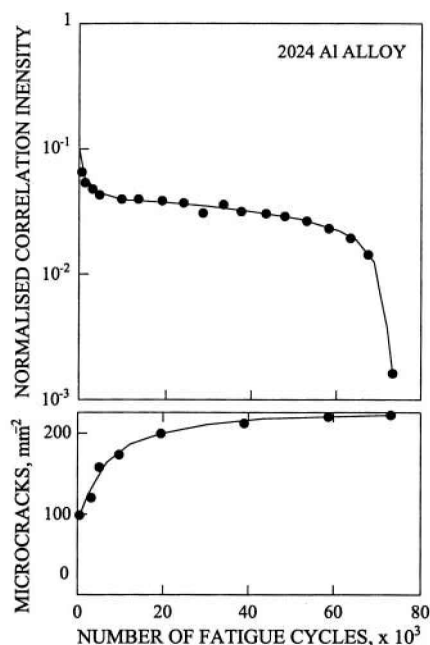
(Fig. 78). They have also related the correlation intensity with crack length (Fig. 79). They have observed a correlation intensity loss of eight orders of magnitude for a crack growth of 700 μm. This study demonstrates the extreme sensitivity of the optical correlation technique for detecting fatigue crack initiation and growth, without any prior knowledge of the precise location where the crack would initiate. Even though optical correlation measurement has high sensitivity, its practical applications are limited. This is because optical correlation measurement is sensitive to rigid body movement and involves a time consuming wet photographic process.

A_2/A_1^2 is ratio of second harmonic amplitude to square of first harmonic amplitude

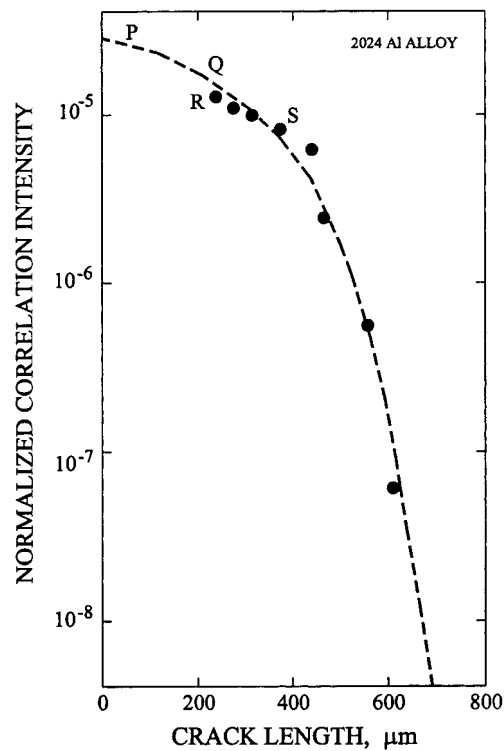76 **Harmonic generation in Al alloy 2024 as function of applied stress[232]**

78 **Variation in optical correlation intensity and microcrack density as function of number of fatigue cycles for 2024 Al alloy[235]**

79 Relationship between optical correlation intensity and fatigue crack length in 2024 Al alloy[235]

Dai *et al.*[236] have shown that the spectrum width technique is advantageous because it is sensitive to surface changes prior to crack initiation. In spectrum width analysis, the speckle pattern is digitised and this digitised intensity distribution is smoothed using numerical processing and is plotted as average grey level as a function of spatial frequency (line/mm). The width at half the maximum grey level is measured as spectrum width. In this study, the spectrum width extracted from the speckle pattern was used to understand different stages of fatigue damage development in 6061-T6 aluminium alloy. Figure 80 shows the variation in spectrum width with number of fatigue cycles for specimens having different values of notch radius. It was observed that the spectrum width increases with the number of cycles. The increasing rate strongly depends on the dimension of the notch
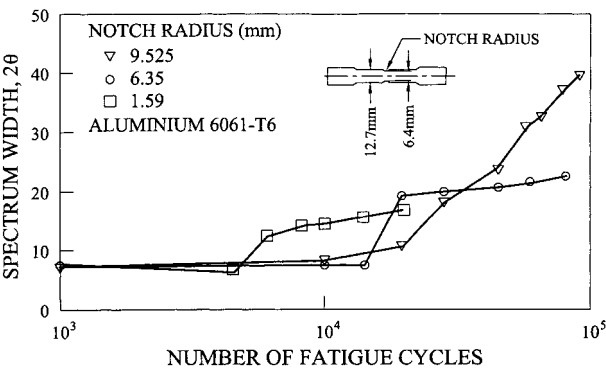
80 Spectrum width 2θ (deg.) versus fatigue life for 6061 Al specimens with different values of notch radius[236]
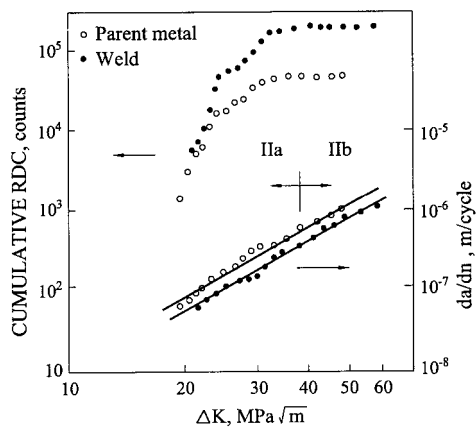
81 Variation in cumulative RDC (ringdown counts) *N* and crack growth rate d*a*/d*n* as function of stress intensity factor range ΔK for parent and weld specimens of AISI type 316 stainless steel[248]

radius, which results in different magnitudes of stress concentration. A drastic change in spectrum width occurs at about 25% of fatigue life, which is attributed to the formation of persistent slip bands. It is also observed that the smaller the notch radius, the earlier the occurrence of the drastic change in spectrum width. This is attributed to the fact that a smaller notch radius results in a greater stress concentration and, hence, early occurrence of slip bands and crack initiation. This drastic change in spectrum width thus emerges as a valid criterion for evaluating the progression in fatigue damage. This non-contact NDT method can also be used for the evaluation of high temperature fatigue damage under non-oxidising conditions.

Acoustic emission (AE) technique

The feasibility of using the AE technique for crack growth measurement has been studied by Hartbower and co-workers.[237,238] Another study by Dunegan *et al.*[239] showed a power law relationship between total number of AE ringdown counts *N* resulting from plastic deformation near the crack tip and the stress intensity factor *K* as

$$N = AK^m$$

Experimental results show that the value of the exponent *m* ranges from 4 to 8 for different materials. This study established that it should be possible to continuously monitor slow crack growth by AE, if the parameters *A* and *m* could be established for a given material of particular thickness. Following these investigations, several attempts have been made to use the AE technique for studying high cycle fatigue crack growth on different materials. These studies have resulted in establishing relationships between AE parameters (such as cumulative AE ringdown counts, count rate (counts/cycle)) and fatigue parameters (such as stress intensity factor range ΔK and crack growth rate d*a*/d*n*).[240–246] Hutton and Kurtz[247] have conducted a mock-up study, using an insert of A533B steel with machined and fatigue pre-sharpened flaws, welded onto a cylindrical pressure vessel of 11·75 cm thickness and
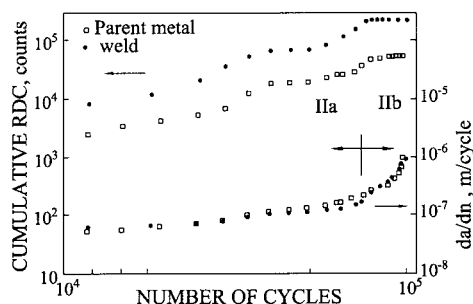
82 Variation in cumulative RDC (ringdown counts) *N* and crack growth rate d*a*/d*n* as function of number of cycles *n* for parent and weld specimens of AISI type 316 stainless steel[248]

145 cm internal diameter. The insert contained three part circular surface flaws; two on the inside surface and one on the outside surface. The longitudinal axis of the flaw was perpendicular to the circumferential stress in the vessel. The test vessel was internally pressurised with water. The water pressurisation system provided constant amplitude, cyclic stressing of the component. A power law relationship between AE event count rate d*N*/d*t* and crack growth rate d*a*/d*t* was obtained. This study showed a good correlation between crack growth rate determined from AE data and that determined from crack opening displacement and fracture surface measurements.

Acoustic emission behaviour during fatigue crack growth in parent and weld specimens of AISI type 316 stainless steel has been studied by Moorthy *et al.*[248,249] It was found that the AE technique can be applied to distinguish the transition from substage IIa to IIb during stage II fatigue crack growth by observing a sharp decrease in AE activity in both parent and weld specimens (Fig. 81). The transition point in AE activity matches with that of crack growth rate (Fig. 82). The transition in crack growth rate and AE activity occurs at 10^{-7} m/cycle, which is in general agreement with the reported values of transition point (Table 4). This information on AE signal thus greatly helps in recognising the transition, providing an opportunity for the early detection of fatigue damage.

It has been established that the cyclic plasticity within the cyclic plastic zone (CPZ) is the major

Table 4 Transition coordinates $(\Delta K)_0$ and $(\mathrm{d}a/\mathrm{d}n)_0$ and slope of $\log(N)$ versus $\log(\Delta K)$ plot during stage IIa for various solution annealed (SA), aged, and weld specimens

Spec.	*t*, mm	Heat treatment	$(\Delta K)_0$, MPa	$(\mathrm{d}a/\mathrm{d}n)_0$ $\times 10^{-7}$, m/cycle	Slope in stage IIa
T6	25	SA	31·02	1·04	5·32
F6	25	SA	31·82	1·01	5·46
T3	25	Aged (2h)	33·2	2·06	4·94
F3	25	Aged (2h)	31·73	1·22	4·92
4	25	Aged (8h)	32·26	2·27	2·69
5	25	Aged (8h)	30·39	1·40	2·29
SA3	12·5	SA	31·39	2·87	5·65
W34	12·5	Weld	30·43	2·75	7·83

t is specimen thickness.
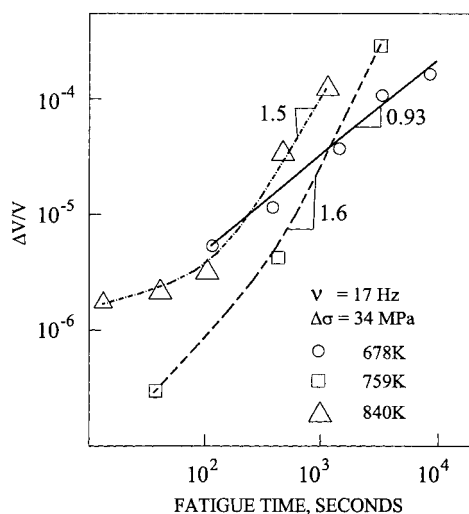
83 Total void volume (from SANS analysis) versus time for fatigued Cu in fully reversed loading with stress amplitude of 34 MPa[250]

source of AE compared to monotonic plastic zone expansion and ductile crack extension.[249] Since during stage IIa the AE signal is mainly generated by the cyclic plasticity within the cyclic plastic zone, the total AE ringdown counts generated at a given ΔK should depend on the size of the cyclic plastic zone, the average plastic strain within the cyclic plastic zone, and the number of cycles before each crack extension. Since all these parameters are functions of ΔK, an empirical relation has been established between cumulative AE ringdown counts and ΔK, which show a power relationship as

$$N = A\Delta K^{\mathrm{m}}$$

where *m* is 5. The experimental results match well with this prediction, as can be seen from Table 5. These studies indicate the possibility of using the AE technique for quantitative estimation of fatigue crack growth rate.

Small angle neutron scattering

Even though neutron scattering is not significantly affected by dislocations, the formation of voids during high temperature fatigue strongly affects the scattering cross-section. Hence, SANS has been used to determine void formation in high temperature fatigue.[250,251] The integrated intensity over the entire range of scattering vector *q* values can be calculated to obtain values of total void volume per unit sample volume $\Delta V/V$. Figure 83 shows the total void volume

Table 5 Slope and correlation coefficient (CC) of $\log$ (cumulative RDC) versus $\log(\Delta K)$ plot during stage IIa for differently annealed samples

Spec.	*t*, mm	Slope in stage IIa	CC
T6	25	4·99	0·83
F6	25	5·22	0·81
SA2	12·5	4·54	0·97
SA3	12·5	5·39	0·90

t is specimen thickness.
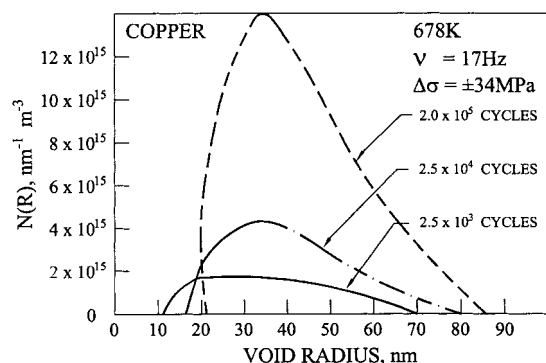
84 Void size distribution determined from SANS analysis for fatigued Cu[250]

fraction measured from SANS as a function of time for fatigued copper in fully reversed loading with a stress amplitude of 34 MPa at temperatures varying from 678 to 843 K. Figure 84 shows the void size distribution (dN/dR versus R) at different fatigue cycles for the same samples obtained from inversion of SANS data. The total number of voids can be calculated from the area of the size distribution curve. These results indicate the high sensitivity of this technique for assessing high temperature fatigue damage. It has been found that a void volume fraction of $\leqslant 10^{-6}$ can be determined using SANS, which is two orders of magnitude below that detectable by density measurements.

Critical assessment

Since fatigue strength is affected by surface properties, NDE techniques sensitive to surface would be more effective methods. X-ray diffraction and laser scattering methods have been found to be excellent techniques to estimate the fatigue limit. Being sensitive to near surface changes, the MBE technique would also be a good method for assessing the fatigue strength, though more work is needed to establish practical applications.

In ultrasonic methods, the velocities do not change significantly during progressive accumulation of fatigue damage. Ultrasonic attenuation measurements clearly indicate the progressive fatigue damage accumulation prior to macrocrack initiation. However, the initial stages of fatigue damage are not assessed adequately. Ultrasonic techniques do not indicate cyclic hardening, softening, etc. Acoustic harmonic generation is found to be very sensitive to the formation of microcracks and their growth.

For ferritic steels, the MBE technique seems to be sufficiently sensitive to the progressive accumulation of fatigue damage compared to the magnetic hysteresis loop method. Changes in the MBE profile clearly indicate every stage of progressive fatigue life right from dislocation generation to crack initiation and propagation. Being sensitive to near surface damage, this is considered a useful method for assessing fatigue life. Since the MBE signal is strongly influenced by the microstructure and the surface residual stresses of ferromagnetic material, the MBE technique is a potential non-destructive method for evaluating the fatigue limit in ferromagnetic steels. However, studies need to be carried out in evaluating the fatigue limit for different microstructures and surface treatments.

Positron annihilation measurements also clearly identify cyclic hardening and cyclic softening, but the technique does not indicate the formation of micro/macrocracks. Since SANS is sensitive to the formation of voids and the growth of precipitates, but not to the dislocation substructure, this technique is found to be useful only in high temperature low cycle fatigue. It is even possible to obtain the variation in void size and distribution with fatigue life quantitatively from the SANS profile.

Since the introduction of tensile stress is the prime cause for crack formation and growth, the measurement of surface stresses would give a clear indication of the region prone to crack initiation. So far, XRD is the only method to estimate the stress accurately. Recently, a magnetic technique based on a multiparameter approach has been shown to have great potential for such applications in ferromagnetic materials as an alternative to XRD.

The XRD method is also found to be sensitive for detection of surface crack initiation and growth. It is quite interesting to know that the measurement of the FWHM of the XRD profile would indicate the remaining life of the component. However, the main difficulty associated with this technique is the time involved and the requirement of knowledge of the regions prone to crack initiation. Also, the XRD system is not really portable for field applications.

The AE technique is found to be a suitable technique for obtaining on-line information on fatigue crack growth provided the background noise level is sufficiently low. This technique indicates the transition from stage IIa to IIb even in ductile materials such as stainless steel, thus giving advance warning well before the catastrophic failure. In single phase materials, it is even possible to quantify the crack growth rate from AE. Being a successful technique for locating dynamic cracks in large size components, the crack growth can easily be monitored to establish its severity.

The optical correlation technique is found to be another potential tool, which has extreme sensitivity for fatigue crack initiation and growth. It can be used even without having any prior information on the region prone to crack initiation. However, the measurement is strongly affected by rigid body movement of the structure or component. The 'spectrum width measurement' method has been found useful in overcoming the limitations associated with rigid body movement in evaluating the fatigue damage.

Summary

The characterisation of microstructures, mechanical properties, deformation and damage initiation and growth by non-destructive evaluation (NDE) techniques is assuming a vital role in various industries because of the growing awareness of the benefits that can be derived by using NDE techniques for assessing the performance of various components. Non-destructive evaluation is particularly assuming greater significance in the assessment of material degradation, where investment in new plant is not cost-effective

and the safe operation lifetime of existing plant needs to be extended. In recent years, various advanced NDE techniques have been successfully employed for the characterisation of defects and microstructural features such as grain size, texture, nucleation and growth of second phases, and the assessment of tensile, creep and fatigue properties, deformation and damage. Non-destructive evaluation techniques are also becoming indispensable in the monitoring and control of fabrication processes for ensuring the desired microstructure of materials and components.

Most components and structures subjected to complex service environments, such as exposure to elevated temperature and/or loading, undergo degradation in mechanical properties, such as strength and fracture toughness, due to microstructural changes, corrosion, creep and fatigue damage. Microstructural features are decisive as these determine the physical, mechanical and corrosion performance of materials. Microstructural features and mechanical properties can be assessed using optical and electron-optical and mechanical testing systems, but these are essentially destructive in nature. For characterisation of the microstructures of components, it is essential to develop techniques that give the required information without destroying the material, thus enabling structural integrity assessment, particularly under the demanding operating conditions of fatigue, creep, high temperatures, radiation and corrosive environments. With the advent of fracture mechanics concepts, the microstructure, defects and stresses must be quantitatively characterised to have reliable and fail-safe materials and components. Changes in the microstructure which reduce life or performance should be predicted sufficiently in advance to apply suitable remedial measures, thus ensuring safe, reliable and economic operation of the components. This is possible when one realises that the interaction of the non-destructive probing medium with the material depends on substructural/microstructural features such as point defects, dislocations, voids, micro- and macrocracks, secondary phases, texture and residual stresses.

In the recent past, many NDE techniques have been developed for the characterisation of microstructures, deformation mechanisms, and fracture behaviour and the assessment of creep and fatigue damage. Ultrasonic parameters (such as attenuation and velocity) and micromagnetic parameters (coercive force and magnetic Barkhausen emission) are being used to determine the variations in grain size and size distribution of second phases due to thermal aging. Non-destructive evaluation techniques such as *in situ* metallography, acoustic emission, ultrasonic attenuation and velocity measurements, acoustic harmonic measurement, magnetic Barkhausen emission, acoustic Barkhausen emission, laser interferometry, positron annihilation, X-ray diffraction and small angle neutron scattering are used for studying creep and fatigue damage. The acoustic emission technique has been extensively used to study the deformation mechanisms, and to determine the low cycle and high cycle fatigue damage and fatigue crack propagation rate, from which in turn the severity of flaws can be estimated. Different stages of fatigue crack growth

can also be identified by the acoustic emission technique. Changes in ultrasonic absorption and velocity have been correlated with changes in dislocation substructure, dislocation density, microcrack formation, etc. Electromagnetic non-destructive testing (NDT) techniques can estimate the fatigue crack depth, void density, microstructural variations, creep strain, etc. Recently developed pulsed laser induced ultrasound techniques have potential as non-contact NDE methods to determine creep and fatigue damage. Techniques such as acoustic microscopy, positron annihilation, and neutron scattering are capable of quantifying the damage produced by thermal aging, creep and fatigue processes. In addition, miniature specimens taken out from the aged components using scooping devices offer the clear possibility to evaluate degradation in tensile and fracture properties, and creep and fatigue damage in components. In the recent past, a stress–strain microprobe system has been developed based on the automated ball indentation technique to determine the tensile and fracture properties of materials in a nearly non-destructive manner.

During NDE-based materials characterisation, the interaction of the probing medium with various microstructural features may lead to complex signals, thus making interpretations very difficult and requiring 'separation' of the signal to obtain feature-specific information. Under such conditions, the use of multiple NDE techniques and NDE parameters in a complementary manner helps in isolating the influence of one or a combination of specific microstructural features. The benefits of non-destructive characterisation and the challenges in the interpretation of results have led to intensive effort worldwide. Modelling, development of new sensors, advanced signal analysis and materials science based approaches are the new directions.

This review clearly brings out that several specialised NDT techniques have been developed for characterisation of microstructure, mechanical properties and the detection of progressive creep and fatigue damage. The specialised NDT techniques have been used with great success by the groups engaged in their development. It is necessary to develop fruitful interactions among various groups to encourage widespread use of the developed NDT methods for the intended applications and to bring out further improvements to make them universally acceptable.

Acknowledgements

References

1. G. DOBMANN, M. KRONENING, W. THEINER, H. WILLEMS and U. FIEDLER: *Nucl. Eng. Des.*, 1992, **157**, 137–158.

2. 'Metals Handbook', Vol. 17, 'Nondestructive testing technique'; 1989, Materials Park, OH, ASM International.
3. BALDEV RAJ, T. JAYAKUMAR and B. P. C. RAO: *J. Aero. Soc. India*, 1994, **46**, 101–115.
4. BALDEV RAJ. T. JAYAKUMAR and M. THAVASIMUTHU: 'Practical non-destructive testing', 1st edn; 1998, New Delhi, Narosa Publishing.
5. R. BECKER, G. DOBMANN, M. KROEBNING, H. REITER and E. SCHNEIDER: *Int. J. Pressure Vessels Piping*, 1997, **73**, 11–17.
6. P. MCINTIRE and R. K. MILLER: 'Non-Destructive Testing Handbook', Vol. 5, 'Acoustic emission testing', 2nd edn, 276; 1987, West Conshohocken, PA, ASTM.
7. R. S. TEBBLE and D. J. CRAIK: 'Magnetic materials', 369–411; 1969, New York, Wiley Interscience.
8. D. C. JILES: 'Introduction to magnetism and magnetic materials', 135; 1994, London, Chapman & Hall.
9. S. TIITTO: *Acta Polytech. Scand., Appl. Phys. Series*, 1977, **119**, 1–80.
10. G. A. MATZKANIN, R. E. BEISSNER and C. M. TELLER: Report No. NTIAC–79–2, Southwest Research Institute, San Antonio, TX, 1979.
11. V. MOORTHY, S. VAIDYANATHAN, T. JAYAKUMAR and BALDEV RAJ: *Philos. Mag. A*, 1998, **77**, 1499–1514.
12. K. ONO: *NDTE Int.*, 1996, **29**, (5), 346–347.
13. G. DOBMANN, W. A. THEINER and R. BECKER: in 'Non-destructive characterization of materials', (ed. P. Holler *et al.*), 516–523; 1988, Berlin, Springer-Verlag.
14. A. VARY: in 'Research techniques in nondestructive testing', Vol. IV, (ed. R. S. Sharpe), chap. 5; 1980, London/New York, Academic Press.
15. E. P. PAPADAKIS: *Int. Met. Rev.*, 1984, **1**, 1.
16. J. P. PANAKKAL, H. WILLEMS and W. ARNOLD: *J. Nucl. Sci.*, 1990, **25**, 1397–1402.
17. O. BUCK, W. L. MORRIS and J. M. RICHARDSON: *Appl. Phys. Lett.*, 1978, **33**, 371.
18. O. BUCK and G. A. ALERS: Proc. ASM Materials Science Seminar, 137; 1979, Materials Park, OH, ASM International.
19. C. S. BARRETT and T. B. MASSALSKI: 'Structure of metals', 3rd edn; 1966, New York, McGraw-Hill.
20. I. C. NOYAN and J. B. COHEN: 'Residual stress measurement by diffraction and interpretation'; 1987, New York, Springer-Verlag.
21. J. R. WEERTMAN: in 'Nondestructive evaluation: microstructural characterization and reliability strategies', (ed. O. Buck and S. M. Wolf), 147–168; 1980, Warrendale, PA, TMS.
22. M. FATEMI, C. S. PANDE and B. B. RATH: in 'Novel NDE methods for materials', (ed. B. B. Rath), 155–192; 1983, Warrendale, PA, TMS.
23. W. BRANDT and A. DUPASQUIER: 'Positron solid state physics'; 1983, Amsterdam, North-Holland.
24. P. HAUTOJARVI: 'Positrons in solids'; 1979, Berlin, Springer-Verlag.
25. E. MAROM: in 'Holographic non-destructive testing', (ed. R. K. Erf), 149–180; 973, New York, Academic Press.
26. W. F. RANSON, M. A. SUTTON and W. H. PETERS: in 'Handbook on experimental mechanics', (ed. A. S. Kobayashi), chap. 8, 388–429; 1987, Englewood Cliffs, NJ, Prentice-Hall.
27. C. BABU RAO: 'Studies on laser scattering to characterise surfaces', PhD thesis, University of Madras, 1999.
28. P. V. KUZNETSOV, V. E. PANIN and J. SCHREIBER: *Theor. Appl. Fract. Mech.*, Mar.–Apr. 2001, **35**, (2), 171–177.
29. G. E. LUCAS: *Metall. Trans. A*, 1990, **21A**, 1105–1119.
30. R. VISWANATHAN: *EPRI J.*, Jan.–Feb. 1995, 40–43.
31. W. R. CORWIN, S. T. ROSINSKI and E. VAN WALLE: in 'Small specimen testing techniques', STP 1329; 1998, West Conshohocken, PA, ASTM.
32. F. M. HAGGAG and K. L. MURTY: in 'Non-destructive evaluation and materials properties III', (eds. P. K. Liaw *et al.*), 101–106; 1997, Warrendale, PA, TMS.
33. P. HOELLER: in 'Nondestructive characterisation of materials II', (ed. J. F. Bussiere, *et al.*), 211–225; 1987, New York, Plenum Press.
34. I. ALTPETER, J. BENDER, J. HOFFMANN and M. KOPP: *Pract. Metallogr.*, 1998, **35**, 126–135.
35. M. N. MIKHEEV and E. S. GORKUNOV: *Sov. J. Nondestr. Test.*, 1981, **17**, 579–592.
36. J. B. GOODENOUGH: *Phys. Rev.*, 1954, **95**, (4), 917–932.
37. T. D. YENSEN and N. A. ZIEGLER: *Trans. ASM*, 1935, **23**, 556–557.

38. W. E. RIEDER: *Trans. ASM*, 1934, **22**, (11), 1120–1141.
39. A. MAGER: *Ann. Phys.*, 1952, **11**, 15.
40. J. DEGAUQUE, B. ASTIE, J. L. PORTESEIL and R. VERGNE: *J. Magn. Magn. Mater.*, 1982, **26**, (1–3), 261–263.
41. C. GATELIER-ROTHEA, P. FLEISCHMANN, J. CHICOIS and R. FOUGERES: *Nondestr. Test. Eval.*, 1992, **8–9**, 591–602.
42. J. KAMEDA and R. RANJAN: *Acta Metall.*, 1987, **35**, 1515–1527.
43. J. KAMEDA: *Scr. Metall.*, 1988, **22**, 1487–1492.
44. R. RANJAN, D. C. JILES, O. BUCK and R. B. THOMPSON: *J. Appl. Phys.*, 1987, **61**, (8), 3199–3201.
45. R. HILL, R. S. GENG, A. COWKING and J. W. MACKERSIE: *NDTE Int.*, 1991, **24**, (4), 179–186.
46. R. RANJAN, D. C. JILES and P. K. RASTOGI: *IEEE Trans. Magn.*, 1987, **23**, 1869–1876.
47. S. TIITTO, M. OTALA and S. SAYMJAKANGAS: *Nondestr. Test.*, 1976, **9**, 117–120.
48. O. SUNDSTROEM and K. TORRONEN: *Mater. Eval.*, 1979, **37**, 51–56.
49. D. J. BUTTLE, J. P. JAKUBOVICS, G. A. D. BRIGGS and C. B. SCRUBY: *Philos. Mag. A*, 1987, **55**, (6), 717–734.
50. R. RANJAN, D. C. JILES, O. BUCK and R. B. THOMPSON: *J. Appl. Phys.*, 1987, **61**, (8), 3199–3201.
51. J. KAMEDA and R. RANJAN: *Acta Metall.*, 1987, **35**, 1527–1531.
52. V. MOORTHY, S. VAIDYANATHAN, T. JAYAKUMAR and BALDEV RAJ: *J. Magn. Magn. Mater.*, 1997, **171**, 179–189.
53. V. MOORTHY, BALDEV RAJ, S. VAIDYANATHAN, T. JAYAKUMAR and B. P. KASHYAP: in 'Review of progress in quantitative non-destructive evaluation', (ed. D. O. Thompson and D. E. Chimenti), Vol. 19, 1525–1532; 2000, New York, American Institue of Physics.
54. V. MOORTHY: 'Characterization of microstructural evolution in ferromagnetic steels using micro-magnetic parameters', PhD thesis, Indian Institute of Technology, Bombay, India, 1999.
55. R. E. GREEN: in 'Nondestructive evaluation: microstructural characterization and reliability strategies', (ed. O. Buck and S. M Wolf), 115–132; 1980, Warrendale, PA, TMS.
56. T. JAYAKUMAR: 'Microstructural characterization of metallic materials using ultrasonic and magnetic methods', PhD thesis, University of Saarland, Saarbrücken, Germany, 1996.
57. E. P. PAPADAKIS: *Metall. Trans.*, 1970, **1**, 1053–1057.
58. P. PALANICHAMY, A. JOSEPH, T. JAYAKUMAR and B. RAJ: *NDTE Int.*, 1995, **28**, 179.
59. P. PALANICHAMY, A. JOSEPH and T. JAYAKUMAR: *Insight*, 1994, **36**, 874.
60. A. VARY: in 'Fracture mechanics', STP 677, (ed. C. W. Smith), 563–578; 1979, West Conshohocken, PA, ASTM.
61. S. HIRSEKORN: *J. Acoust. Soc. Am.*, 1982, **72**, 1021.
62. S. HIRSEKORN: *J. Acoust. Soc. Am.*, 1983, **73**, 1160.
63. ANISH KUMAR, T. JAYAKUMAR, P. PALANICHAMY and BALDEV RAJ: *Scr. Metall.*, 1999, **40**, (3), 333–340.
64. ANISH KUMAR, T. JAYAKUMAR and BALDEV RAJ: *Philos. Mag. A*, 2000, **80**, 2469–2487.
65. T. JAYAKUMAR and ANISH KUMAR: *J. Acoust. Soc. India*, 1999, **27**, (1–4), 75–84.
66. S. HIRSEKORN: *J. Acoust. Soc. Am.*, 1982, **72**, 1021–1031.
67. S. HIRSEKORN: *J. Acoust. Soc. Am.*, 1983, **73**, 1160–1163.
68. T. JAYAKUMAR, C. K. MUKHOPADHYAYA, K. KASIVISWANATHAN and BALDEV RAJ: *Trans. Ind. Inst. Met.*, 1998, **51**, 485–507.
69. A. MORO, C. FARINA and F. ROSSI: *NDT Int.*, 1980, **13**, (4), 169–175.
70. P PALANICHAMY, M. VASUDEVAN, T. JAYAKUMAR, S. VENUGOPAL and B. RAJ: *NDTE Int.*, 2000, **33**, 253–259.
71. H. WILLEMS: in 'Review of progress in quantitative nondestructive evaluation', (ed. D. O. Thompson and D. E. Chimenti), Vol. 6A, 473; 1987, New York, Plenum.
72. E. S. GORKUNOV: *Sov. J. Nondestr. Test.*, 1991, **27**, (4), 231–259.
73. M. N. MIKHEEV and E. S. GORKUNOV: *Sov. J. Nondestr. Test.*, 1985, **21**, (3), 155–172.
74. T. JAYAKUMAR, T. D. KOBLE, W. A. THEINER and BALDEV RAJ: *Nondestr. Test. Eval.*, 1993, **10**, 205–214.
75. S. TIITTO: 'Principles of the magnetoelastic Barkhausen noise method', American Stress Technologies Inc., Pittsburgh, PA, USA, 1991.
76. D. J. BUTTLE, C. B. SCRUBY, G. A. D. BRIGGS and J. P. JAKUBOVICS: *Proc. R. Soc. (London) Series A*, 1987, **A414**, 469–497.
77. K. P. STAUDHAMMER, L. E. MURR and S. S. HECKER: *Acta Metall.*, 1983, **31**, 267.
78. D. L. DIJKSTRA and C. WERT: *Phys. Rev.*, 1950, **79**, (6), 979–985.
79. B. D. CULLITY: 'Introduction to magnetic materials', 292; 1972, Reading, MA, Addison Wesley.

80. B. I. VORONENKO: *Sov. J. Nondestr. Test.*, 1986, **22**, 535.
81. M. N. MIKHEEV and E. S. GORKUNOV: *Sov. J. Nondestr. Test.*, 1985, **21**, (12), 807–822.
82. E. S. GORKUNOV: *Sov. J. Nondestr. Test.*, 1991, **27**, (4), 231–259.
83. M. KERSTEN: *Z. Phys.*, **1948**, 124, 714–742.
84. C. KITTEL: *Rev. Mod. Phys.*, 1949, **21**, 541.
85. L. NEEL: *Physica*. 1949, **15**, 225.
86. E. KNELLER: 'Ferromagnetismus', 533–538; 1962, Berlin, Springer-Verlag.
87. H. D. DIETZE: *J. Phys. Soc. Jpn Suppl. B1*, 1962, **81**, 663–665.
88. M. K. DEVINE, D. C. JILES and S. HARIHARAN: *J. Magn. Magn. Mater.*, 1992, **104–107**, 377–378.
89. S. P. NARAYANAN, V. RAO, S. DAS and O. N. MOHANTY: *J. Magn. Magn. Mater.*, 1990, **88**, 71–78.
90. S. P. NARAYANAN, V. RAO and O. N. MOHANTY: *J. Magn. Magn. Mater.*, 1991, **96**, 137–144.
91. J. DRABECKI and B. WYSLOCKI: *Phys. Status Solidi A*, 1975, **30**, (1), 345–355.
92. L. CLAPHAM. C. JAGADISH and D. L. ATHERTON: *Acta Metall.*, 1991, **39**, 1555–1562.
93. D. J. BUTTLE, J. P. JAKUBOVICS and G. A. D. BRIGGS: *Philos. Mag. A*, 1987, **55**, (6), 735–756.
94. A. H. WAFIK, N. A. RAZIK and M. H. ZAYAN: *Phys. Status Solidi A*, 1989, **116**, 383–388.
95. A. H. WAFIK and N. A. RAZIK: *Phys. Status Solidi A*, 1991, **126**, 451–458.
96. D. K. BHATTACHARYA, T. JAYAKUMAR, V. MOORTHY, S. VAIDYANATHAN and BALDEV RAJ: *NDTE Int.*, 1993, **26**, (3), 141–148.
97. I. ALTPETER, R. KERN, M. LANG and H. ROSNER: 'Detection of copper precipitates by means of micromagnetic parameters', Report 980232–TW, Fraunhofer Institute for Non-destructive Testing, Saarbrücken, Germany, April 1998.
98. V. MOORTHY, S. VAIDYANATHAN, T. JAYAKUMAR, BALDEV RAJ and B. P. KASHYAP: *Metall. Mater. Trans. A*, 2000, **31A**, 1053–1081.
99. I. ALTPETER: Proc. 3rd Int. Symp. on 'Nondestructive characterization of materials', (ed. P. Hoeller *et al.*), 606–613; 1989, Berlin, Springer-Verlag.
100. M. G. HETHERINGTON, J. P. JAKUBOVICS, J. A. SZPUNAR and B. K. TANNER: *Philos. Mag. B*, 1987, **56**, (5), 561–577.
101. A. D. BEALE, J. P. JAKUBOVICS, M. G. HETHERINGTON, C. B. SCRUBY, B. A. LEWIS and K. J. DAVIES: *J. Magn. Magn. Mater.*, 1992, **104–107**, 365–367.
102. S. VAIDYANATHAN, V. MOORTHY, T. JAYAKUMAR and BALDEV RAJ: *Mater. Sci. Technol.*, 2000, **16**, (2), 202–208.
103. M. ROSEN: in 'Analytical ultrasonics in materials research and testing', NASA Conf. Publication 2383, NASA Lewis Research Center, Cleveland, OH, Nov. 1984, p. 83.
104. M. ROSEN, L. IVES, S. RIDDER, F. BIANCANIELLO and R. MEHRABIAN: *Mater. Sci. Eng. A*, 1985, **74**, 1.
105. M. ROSEN: Proc. Conf. on 'Advanced NDE technology', (ed. J. F. Bussiere), 54; 1982, Montreal, Canada, National Research Council of Canada.
106. T. JAYAKUMAR, BALDEV RAJ, H. WILLEMS and W. ARNOLD: in 'Review of progress in quantitative nondestructive evaluation', (ed. D. O. Thompson and D. E. Chimenti), Vol. 10B, 1693–1699; 1991, New York, Plenum.
107. B. P. RAO, T. JAYAKUMAR, D. K. BHATTACHARYA and BALDEV RAJ: *J. Pure Appl. Ultrasonics*, 1993, **15**, 53–59.
108. T. JAYAKUMAR, P. PLANICHAMY and BALDEV RAJ: *J Nucl. Mater.*, 1998, **255**, 243–249.
109. C. K. MUKHOPADHYAY, T. JAYAKUMAR, K. V. KASIVISWANATHAN and BALDEV RAJ: in 'Advances in physical metallurgy', (ed. S. Banerjee and R. V. Ramanujan), 542; 1995, New York, Gordon and Breach.
110. C. K. MUKHOPADHYAY, T. JAYAKUMAR, K. V. KASIVISWANATHAN and BALDEV RAJ: *J. Mater. Sci.*, 1995, **30**, 4556.
111. R. W. SIEGEL: in 'Encyclopedia of Materials Science and Engineering', (ed. M. B. Berer), Vol. 5, 3856–3857; 1986, New York, Pergamon.
112. S. ABIS, P. BARTOLOMEI, M. BIASINI, M. VALLI and A. DUPASQUIER: *Phys. Status Solidi A*, 1992, **129**, (1), 143–148.
113. W. B. GAUSTER and W. R. WAMPLER: *Philos. Mag. A*, 1980, **41**, 143.
114. J. K. TIEN, S. J. TAO, J. P. WALLACE and S. PURUSHOTHAMAN: in 'Electron and positron spectroscopies in materials science and engineering', 73–119; 1979, New York, Academic Press.
115. S. C. SHARMA, R. M. JOHNSON and L. M. DIANA: in 'Novel NDE methods of materials', (ed. B. B. Rath), 45–61; 1983, Warrendale, PA, TMS.
116. PADMA GOPALAN, R. RAJARAMAN, B. VISWANATHAN, K. P. GOPINATHAN and S. VENKATESAN: *J. Nucl. Mater.*, 1998, **256**, 229–234.
117. G. KOSTORZ: in 'Treatise on Materials Science and Technology', Vol. 15, 'Neutron scattering'; 1979, New York, Academic Press.
118. H. WALTERM and A. PIZZI: in 'Research techniques in non-destructive testing', Vol. IV, (ed. R. S. Sharpe), 314–391; 1980, London/New York, Academic Press.
119. P. PIZZI: AGARD Meeting on 'NDI relationships to aircraft design and materials', Structures and Materials Panel, Advisory Group for Aerospace Research and Development, Norway, Sept. 1977, 5-1–5-7.
120. P. CORTESE, P. PIZZI, H. WALTHER, G. BERNARDINI and A. OLIVI: *Mater. Sci. Eng.*, 1978, **36**, 81–88.
121. S. KIM, J. R. WEERTEMAN, S. SPOONER, C. J. GLINKA, V. SIKKA and W. B. JONES: in 'Nondestructive evaluation: application to materials processing', (ed. O. Buck and S. M. Wolf), 169–176; 1983, Warrendale, PA, TMS.
122. P. PIZZI, H. WALTHER and P. CORTESE: Proc. 8th World Conf. on 'Nondestructive testing', Cannes, France, 1976, French Society for Non-destructive Testing (COFREND), p. 3L7.
123. A. VARY: *Mater. Eval.*, 1978, **36**, 55–64.
124. J. KRAUTKRAMER and H. KRAUTKRAMER: 'Ultrasonic testing of materials'; 1977, New York, Springer-Verlag.
125. ANISH KUMAR, K. LAHA, T. JAYAKUMAR, K. BHANU SANKARA RAO and BALDEV RAJ: *J. Pure Appl. Ultrasonics*, 1999, **21**, (2), 1–10.
126. M. N. MIKHEEV and E. S. GORKUNOV: *Sov. J. Nondestr. Test.*, 1985, **21**, (3), 155–172.
127. M. N. MIKHEEV: *Sov. J. Nondestr. Test.*, 1983, **19**, 1–8.
128. M. N. MIKHEEV and E. S. GORKUNOV and F. N. DUNAEV: *Defektoskopiya*, 1977, **13**, (6), 7–18.
129. M. N. MIKHEEV, E. S. GORKUNOV, V. M. SOMOVA and A. B. KUTKIN: *Sov. J. Nondestr. Test.*, 1982, **18**, (9), 725–734.
130. D. C. JILES and J. D. VERHOEVEN: in 'Review of progress in quantitative nondestructive evaluation', (ed. D. O. Thompson and D. E. Chimenti), Vol. 6B, 1681–1690; 1987, New York, Plenum.
131. M. N. MIKHEEV, V. M. MOROZOVA, A. P. MOROZOVA, B. M. NEIZVESTNOV, G. V. SURIN and G. N. ZAKHAROVA: *Sov. J. Nondestr. Test.*, 1978, **14**, (1), 9–17.
132. E. S. GORKUNOV, V. M. SOMOVA and T. P. TSARKOVA: *Sov. J. Nondestr. Test.*, 1991, **27**, (10), 729–733.
133. G. V. BIDA and V. M. KAMARDIN: *Sov. J. Nondestr. Test.*, 1991, **27**, (7), 458–468.
134. V. MOORTHY, S. VAIDYANATHAN, K. LAHA, T. JAYAKUMAR, K. B. S. RAO and BALDEV RAJ: *Mater. Sci. Eng. A*, 1997, **A231**, 98–104.
135. G. V. LOMAEV, V. S. MALYSHEV and A. P. DEGTEREV: *Sov. J. Nondestr. Test.*, 1984, **20**, 189–203.
136. I. G. PALMER: *Mater. Sci. Eng.*, 1973, **11**, 227–236.
137. H. L. DUNEGAN, D. O. HARRIS and C. A. TATRO: *Eng. Fract. Mech.*, 1968, **1**, 105–110.
138. H. TAKAHASHI, M. A. KHAN, M. KIKUCHI and M. SUZUKI: *Exp. Mech.*, 1981, **3**, 89–99.
139. G. E. LUCAS, J. W. SHECHERD, G. R. ODETTE and S. PANCHANADEESARAH: *J Nucl. Mater.*, 1984, **122–123**, 429–434.
140. K. V. KASIVISWANATHAN, S. K. HOTTA, C. K. MUKHOPADHYAY and B. RAJ: in 'Small specimen test techniques', STP 1329, (ed. W. R. Corwin *et al.*), 523–538; 1998, West Conshohocken, PA, ASTM.
141. M. P. MANHAN, A. E., BROWNING, A. S. ARGON and O. K. HARLING: in 'The use of small scale specimens for testing irradiated materials', STP 888, (ed. W. R. Corwin and G. E. Lucas), 17–49; 1986, West Conshohocken, PA, ASTM.
142. J. R. FOULDS, P. J. WOYTOWITZ, T. K. PARNELL and C. W. JENNETT: *J. Test. Eval.*, 1995, **23**, 3–10.
143. N. G. MURALIDHARAN, T. JAYAKUMAR, RAKESH KAUL, A. RAMABATHIRAN, K. V. KASIVISWANATHAN, D. K. BHATTACHARYA and BALDEV RAJ: Proc. 7th Asia–Pacific Conf. on 'Non-destructive Testing', Sanghai, China, Sept. 1993, Chinese Society for Non-destructive Testing, 768–785.
144. K. L. MURTY, M. D. MATHEW, Y. WANG, V. N. SHAH and F. M. HAGGAG: *Int. J. Pressure Vessel Piping*, 1998, **75**, 831–840.
145. W. K. LEE, D. R. METZGER, A. DONNER and O. E. LEPIK: in 'Small specimen test techniques', STP 1329, (ed. W. R. Corwin *et al.*), 539–553; 1998, West Conshohocken, PA, ASTM.
146. J. H. BULLOCH: *Int. J. Press. Vessels Piping*, 1998, **75**, 791–804.
147. T. MATSUSHITA, M. L. SAUCEDO, Y. H. JOO, and T. SHOJI: *Key Eng. Mater.*, 1990, **51–52**, 259–264.

148. Y. H. JOO, T. HASHIDA and T. TAKAHASHI: *J. Test. Eval.*, 1992, **6**, 20–31.
149. J. H. BULLOCH: *Int. J. Press. Vessels Piping*, 1995, **63**, 63–74.
150. L. P. KARJALAINEN and M. MOILANEN: *NDT Int.*, 1979, **22**, (2), 51–57.
151. L. P. KARJALAINEN, M. MOILANEN and R. RAUTIOAHO: *Mater. Eval.*, 1979, **37**, (9), 45–51.
152. V. MOORTHY, S. VAIDYANATHAN, T. JAYAKUMAR, BALDEV RAJ and B. P. KASHYAP: *Acta Mater.*, 1999, **47**, (6), 1868–1879.
153. S. VAIDYANATHAN, V. MOORTHY, P. KALYANASUNDARAM, T. JAYAKUMAR and BALDEV RAJ: *Metall. Mater. Trans. A*, 1999, **30A**, 2067–2072.
154. C. R. HEIPLE and S. H. CARPENTER: *J. Acoust. Emiss.*, 1987, **6**, (3), 177–205.
155. C. R. HEIPLE and S. H. CARPENTER: *J. Acoust. Emiss.*, 1987, **6**, (4), 215–237.
156. BALDEV RAJ: 'Acoustic emission during tensile deformation and fracture in austenitic stainless steel', PhD thesis, Indian Institute of Science, Bangalore, India, 1989.
157. H. N. G. WADLEY and C. B. SCRUBY: *J. Mater. Sci.*, 1991, **26**, 5777–5792.
158. C. B. SCRUBY and H. N. G. WADLEY: *J. Mater. Sci.*, 1993, **28**, 2501–2516.
159. H. N. G. WADLEY and C. B. SCRUBY: *J. Mater. Sci.*, 1993, **28**, 2517–2530.
160. A. VINOGRADOV: *Acta Mater.*, 1998, **39**, (6), 797–805.
161. T. BIDLINGMAIER, A. WANNER, G. DEHM and H. CLEMENS: *Z. Metallkd.*, 1999, **90**, (8), 581–587.
162. BALDEV RAJ and T. JAYAKUMAR: in 'Acoustic emission: current practice and future directions', STP 1077, 218–241; 1991, West Conshohoken, PA, ASTM.
163. G. AIROLDI: *Met. Sci.*, 1980, **14**, 569–578.
164. K. N. TANDON and K. TANGIN: *Mater. Sci. Eng.*, 1975, **20**, 47–54.
165. Q. Y. LONG and YIN HUAZI: *Metall. Trans. A*, 1990, **21A**, 373–379.
166. C. H. CACERES: *Acta Metall.*, 1987, **35**, 2851.
167. P. FLEISCHMANN: *Nondestr. Test.*, 1975, 241–244.
168. BALDEV RAJ, T. JAYAKUMAR, P. KALYANASUNDARAM, P. BARAT, B. B. JHA, D. K. BHATTACHARYA and P. RODRIGUEZ: *J. Acoust. Emiss.*, 1989, **8**, S149.
169. R. PASCUAL: *Scr. Metall.*, 1974, **8**, 1461.
170. C. R. HEIPLE: *Met. Sci.*, 1981, **15**, 587.
171. C. B. SCRUBY: *Met. Sci.*, 1981, **15**, 599.
172. C. B. SCRUBY, H. N. G. WADLEY and K. L. RUSHBRIDGE: *Mater. Sci. Eng.*, 1983, **59**, 169–183.
173. R. D. YOUNG, D. A. ARMENTROUT and S. H. CARPENTER: Proc. 8th Int. Symp. on 'Acoustic Emission', 'Progress in Acoustic Emission III', Tokyo, Japan, Oct. 1986, The Japanese Society for Nondestructive Inspection.
174. C. H. CACERES: *Scr. Metall.*, 1983, **17**, 1115.
175. W. F. HARTMAN: *Exp. Mech.*, 1974, **14**, 19–23.
176. T. TAKAGAKI and A. K. MUKHERJEE: in 'Strength of materials and alloys', Vol. 1, 589–593; 1979, Oxford, Pergamon Press.
177. T. JAYAKUMAR, BALDEV RAJ, P. RODRIGUEZ and O. PRABHAKAR: *Trans. Ind. Inst. Met.*, 1987, **40**, (2), 147–150.
178. T. JAYAKUMAR, BALDEV RAJ, D. K. BHATTACHARYA, P. RODRIGUEZ and O. PRABHAKAR: *Scr. Metall.*, 1991, **25**, 2733–2738.
179. B. RAJ. B. B. JHA and P. RODRIGUEZ: *Acta. Metall.*, 1989, **37**, (8), 2211–2215.
180. V. MOORTHY, T. JAYAKUMAR and BALDEV RAJ: *J. Pressure Vessels Piping*, 1995, **64**, 161–168.
181. C. K. MUKHOPADHYAY, T. JAYAKUMAR, K. V. KASIVISWANATHAN. and BALDEV RAJ: *J. Mater Sci.*, 1995, **30**, 4556–4560.
182. C. K. MUKHOPADHYAY, K. V. KASIVISWANATHAN, T. JAYAKUMAR and BALDEV RAJ: *J. Mater. Sci.*, 1993, **28**, 145–154.
183. D. R. SMITH and S. H. CARPENTER: *J. Acoust. Emiss.*, 1988, **7**, (1), 9–19.
184. H. TAKAHASHI, M. A. KHAN, M. KIKUCHI and M. SUZUKI: *Exp. Mech.*, 1981, **3**, 89–99.
185. F. LIU: in 'ASM Handbook', Vol. 19, 'High temperature life assessment', 520; 1997, Materials Park, OH, ASM International.
186. R. VISWANATHAN: 'Damage mechanisms and life asssessment of high temperature components'; 1989, Materials Park, OH, ASM International.
187. D. MILANOVIC, V. SIJACKI-ZERAVCIC, A. MARKOVIC and M. RADOVIC: *Mater. Sci. (Russia)*, 1994, **30**, (5), 588–597.
188. F. NOGATA and H. TAKAHASHI: *J. Pressure Vessel Technol. (Trans. ASME)*, 1995, **117**, (1), 14–18.
189. H. STAMM: *Eur. J. Nondestr. Test.*, 1992, **1**, (4), 169–178.
190. U. STIGH: *Eng. Fract. Mech.*, 1987, **28**, 1.
191. H. WILLEMS, W. BENDICK and H. WEBER: 2nd Int. Symp. on 'Non-destructive characterization of materials', (ed. J. F. Bussiere *et al.*); 1986, New York, Plenum.
192. H. WILLEMS and G. DOBMANN: *Nucl. Eng. Des.*, 1991, **128**, 139–149.
193. M. HIRAO, T. MORISHITA and H. FUKUOKA: *Metall. Trans. A*, 1990, **21A**, 1725–1732.
194. U. VON ESTORFF and H. STAMM: Proc. 5th Int. Conf on 'Creep of materials', 287–296; 1992, Materials Park, OH, ASM International.
195. C. PEREZ, R. MARTINEZ-ONA and J. BANES: Proc. 6th European Conf. on 'Non-destructive testing', Nice, France, 1994, French Society for Non-destructive Testing (COFREND), 543–547.
196. L. BRATHE: *Scand. J. Metall.*, 1978, **7**, 199.
197. C. F. YING and R. TRUELL: *J. Appl. Phys.*, 1956, **27**, 1066.
198. P. C. WATERMAN and R. TRUELL: *J. Math. Phys.*, 1961, **2**, 512.
199. C. M. SAYERS: *J. Phys. D, Appl. Phys.*, 1981, **14**, 413–430.
200. C. M. SAYERS: *J. Phys. D, Appl. Phys.*, 1981, **14**, 179.
201. M. SAYERS and R. L. SMITH: *Ultrasonics*, 1998, **20**, 201.
202. T. E. GOMEZ, J. A. GALLOEGO, E. RIERA, R. MARTINEZ and V. LOPEZ: 'Ultrasonics International '91 Conference Proceedings', Le Touquet, France, July 1991, 503–506; 1991, Butterworth-Heinemann.
203. T. GOMEZ, E. RIERA and J. A. GALLOEGO: *J. Ultrasonics*, 1993, **3**, 1155.
204. E. A. PAPADAKIS: *J. Appl. Phys.*, 1964, **35**, 1474.
205. T. JAYAKUMAR, BALDEV RAJ and P. RODRIGUEZ: Proc. Int. Conf. on 'Computational Engineering Science', 'Computational mechanics '95: theory and applications', (ed. J. Boogaard and G. M. van Dijk), Vol. 1, 1377–1382, 1995; Amsterdam, Elsevier.
206. H. YONEYAMA, M. NAKASHIRO, S. SHIBATA, and A. OHTOMA: Proc. 12th World Conf. on 'Non-destructive testing', Amsterdam, 1989, 1743–1748.
207. E. S. GORKUNOV, A. P. NICHIPURK, V. M. SOMOVA and V. I. LEVIT: *Sov. J. Nondestr. Test.*, 1993, **29**, (7), 535–539.
208. M. R. GOVINDARAJU, D. A. KAMINSKI, M. K. DEVINE, S. B. BINER and D. C. JILES: *NDTE Int.*, 1997, **30**, (1), 11–17.
209. M. NEGLEY, M. R. GOVINDARAJU and D. C. JILES: in 'Review of progress in quantitative nondestructive evaluation', (ed. D. O. Thompson and D. E. Chimenti), Vol. 13B, 1817–1824; 1993, New York, Plenum.
210. A. MITRA, Z. J. CHEN and D. C. JILES: in 'Review of progress in quantitative nondestructive evaluation', (ed. D. O. Thompson and D. E. Chimenti), Vol. 14B, 1733–1740; 1994, New York, Plenum.
211. H. WILLEMS, T. JAYAKUMAR, T. KOBLE and W. THEINER: 'Second Annual Report on Project D4', Cost 501/II WP 5C, 1989–90, European Committee on Special Testing, IzfP, Saarbrücken, Germany, June 1990.
212. G. G. NILSSON and M. ROTH, *Mater. Sci. Eng.*, 1981, **50**, 101–108.
213. R. PAGE, J. R. WEERTMAN and M. ROTH: *Acta Metall. Mater.*, 1982, **30**, 1357–1366.
214. TORU GOTO: 'Advances in X-ray analysis', (ed. C. S. Barrett *et al.*), Vol. 35, 489–501; 1992, New York, Plenum.
215. J. BRESSERS, W. HESSLER, U. W. HILDEBRANDT and H. WILLEMS: Proc. Conf on 'High temperature materials for power engineering', Part I, (ed. E. Bachelet *et al.*), 629–642; 1990, Dordrecht, Kluwer Academic.
216. P. KALYANASUNDARAM, J. RESZAT and M. PAUL: Internal Report 940142–E, Fraunhofer Institute for Nondestructive Testing, Saarbrücken, Germany, 1994.
217. M. B. SHAH and M. S. C. BOSE: *Phys. Status Solidi*, 1984, **86**, 275–281.
218. M. S. C. BOSE: *NDT Int.*, 1986, **19**, 83–87.
219. M. R. GOVINDARAJU, A. STROM, D. C. JILES and S. B. BINER: in 'Review of progress in quantitative nondestructive evaluation', (ed. D. O. Thompson and D. E. Chimenti), Vol. 12B, 1839–1846; 1993, New York, Plenum.
220. M. R. GOVINDARAJU, Z. J. CHEN, A. STROM, S. B. BINER and D. C. JILES: in 'Nondestructive evaluation and materials properties II', (ed. P. K. Liaw *et al.*), 133–144; 1994, Warrendale, PA, TMS.
221. Y. BI and D. C. JILES: in 'Review of progress in quantitative nondestructive evaluation', (ed. D. O. Thompson and D. E. Chimenti), Vol. 17B, 1509–1515; 1998, New York, Plenum.
222. L. P. KARJALAINEN and M. MOILANEN: *IEEE Trans. Magn.*, 1980, **MAG–16**, (3), 514–517.

223. K. TIITTO: *Nondestr. Test. Eval.,* 1989, **5**, 27–37.
224. M. R. GOVINDARAJU, A. STROM, D. C. JILES, S. B. BINER and Z. J. CHEN: *J. Appl. Phys.,* 1993, **73**, (10), 6165–6167.
225. V. MOORTHY, B. K. CHOUDHARY, S. VAIDYANATHAN, T. JAYAKUMAR, K. BHANU SANKARA RAO and BALDEV RAJ: *Int. J. Fatigue,* 1999, **21**, 263–269.
226. K. G. LYNN and J. G. BYRNE: *Metall. Trans. A,* 1976, **7A**, 604–606.
227. K. NISHIWALEI, N. OWADA, K. HINODE, S. TANIJAWA, K. SHIBATA, T. FUJITA and M. DOYAMA: Proc. 5th Int. Conf. on 'Positron annihilation', Lake Yamanaka, Japan, 1979, 177–180.
228. N. MAEDA, N. NAKAMURA, M. UCHIDA, Y. OHTA and K. YOSHIDA: *Nucl. Eng. Des.,* 1996, **167**, (2), 169–174.
229. M. UCHIDA, Y. OHTA, N. NAKAMURA and K. YOSHIDA: Proc. 13th Int. Conf. on 'NDE in nuclear and pressure vessel industries', (ed. K. Iida *et al.*), Kyoto, Japan, May 1995, 349–353.
230. S. K. RAI, T. JAYAKUMAR, BALDEV RAJ and P. RODRIGUEZ: Proc. Int. Symp. on 'Inelastic deformation, damage and life analysis '97', (ed. S. N. Atluri and G. Yagawa), 64–69; 1997, Forsyth, GA, Tech Science Press.
231. N. R. JOSHI and R. E. GREEN: *Eng. Fract. Mech.,* 1972, **4**, 577–583.
232. O. BUCK, W. L. MORRIS and J. M. RICHARDSON: *Appl. Phys. Lett.,* 1978, **33**, 371.
233. O. BUCK and G. A. ALERS: Proc. ASM Materials Science Seminar, 137; 1979, Materials Park, OH, ASM International.
234. W. L. HAWORTH: *Fatigue Eng. Mater. Struct.,* 1979, **1**, 351–361.
235. W. L. HAWORTH, V. K. SINGH and R. K. MUELLER: *Metall. Trans. A,* 1980, **11A**, 219–229.
236. Y. Z. DAI, A. KATO and F. P. CHIANG: *Int. J. Fatigue,* 1991, **13**, (3), 227–232.
237. W. W. GERBERICH and C. E. HARTBOWER: *Int. J. Fract. Mech.,* 1967, **3**, (3), 185–192.
238. C. E. HARTBOWER, W. W. GERBERICH and H. LIEBOWITZ: *Eng. Fract. Mech.,* 1968, **1**, (2), 291–307.
239. H. L. DUNEGAN, D. O. HARRIS and C. A. TATRO: *Eng. Fract. Mech.,* 1968, **1**, 105–121.
240. Y. MORI, Y. SAHAKIBARA, T. NAGATA, T. OHIRA and T. KISHI: Proc. 5th Acoustic Emission Symp., Tokyo, 1980, Japanese Society for Nondestructive Inspection, 465–474.
241. H. L. DUNEGAN, D. O. HARRIS and A. S. TETELMAN: *Mater. Eval.,* 1970, **28**, (10), 221–227.
242. T. OHIRA, T. KISHI and R. HOREUCHI: Proc. 5th Acoustic Emission Symp., Tokyo, 1980, Japanese Society for Nondestructive Inspection, 137–145.
243. T. M. MORTON, R. M. HARRINGTON and I. G. BJELECTICH: *Eng. Fract. Mech.,* 1973, **5**, 691–693.
244. T. C. LINDLEY, I. G. PALMER and C. E. RICHARDS: *Mater. Sci. Eng.,* 1978, **32**, 1–15.
245. F. HAMEL, J. P. BAILON and M. N. BASSIM: *Eng. Fract. Mech.,* 1981, **14**, 853–860.
246. V. MOORTHY, T. JAYAKUMAR, D. K. BHATTACHARYA and BALDEV RAJ: Proc. Int. Symp. on 'Fatigue and fracture of steel and concrete structures', ISFF91, Structural Engineering Research Centre, Madras, 1991, Vol. 1, 219–233.
247. P. H. HUTTON and R. J. KURTZ: Proc. 8th Water Reactor Safety Research Information Meeting, Gaithersburg, MD, Oct. 1980, NRC, USA, National Bureau of Standards.
248. V. MOORTHY, T. JAYAKUMAR and BALDEV RAJ: *Mater. Sci. Technol.,* 1996, **12**, (1), 56–58.
249. V. MOORTHY, T. JAYAKUMAR and BALDEV RAJ: *Bull. Mater. Sci.,* 1994, **17**, (6), 699–715.
250. R. PAGE, J. R. WEERTMAN and M. ROTH: *Scr. Metall.,* 1980, **14**, 773–777.
251. R. PAGE, J. R. WEERTMAN and M. ROTH: *Acta Metall. Mater.,* 1982, **30**, 1357–1366.